Fall 2021

# Characterizations of Dissolved Organic Carbon at Hydrothermal Systems of the MidCayman Rise

Aaron Mau

# Characterizations of Dissolved Organic Carbon at Hydrothermal Systems of the Mid-Cayman Rise

by

Aaron Mau

Bachelor of Science
University of Washington, 2018

---

Submitted in Partial Fulfillment of the Requirements

For the Degree of Master of Science in

Marine Science

College of Arts and Sciences

University of South Carolina

2021

Accepted by:

Susan Lang (Director of Thesis)

Michael Bizimis (Reader)

Lori Ziolkowski (Reader)

Jeffrey Seewald (Reader)

Tracey L. Weldon, Interim Vice Provost and Dean of the Graduate School

## ACKNOWLEDGEMENTS

I would not have had my graduate experience if not for my advisor, Dr. Susan Lang. Her immense scientific knowledge on all things hydrothermal, paired with her wisdom in a scientific context always inspired me to produce the best work that I could. Her patience and genuine concern were what made me keep trying when I hit a wall, consider alternatives, and pursue my passions. I've grown tremendously through a bumpy ride and for that, I'm very thankful to have had her during my graduate experience. I'd also like to give a special thanks to the rest of my committee: Dr. Michael Bizimis, Dr. Lori Ziolkowski, and Dr. Jeffrey Seewald.

Thanks must also be extended to the past and present members of the Lang Lab. Bryan Benitez-Nelson, Malayika Vincent, Cameron Henderson, Jessica Frankle, J.J. Fryer, Jessica Rodgers, Maddie Petersen, and Claire Matta have played key roles running analyses, showing me a technique, brainstorming, or smiling and nodding during a practice presentation.

There are also numerous collaborators which I would like to thank. First and foremost, the captain and crew of R/V *Atlantis* cruise 42-22 as well as the ROV *JASON II* team. Thanks to Dr. Andre Simpson and his team at the University of Toronto, Dr. Li Xu and others at the NOSAMS facility in Woods Hole, and Dr. Tom McCollom at the University of Colorado.

Finally, I would like to give a special thanks to those that encouraged me during this journey. Kevin Hurler, Osama Alian, Annie Klyce, Allison Brown, Jacob Samuelsen,

Ben Songrass-Rosales, Derek Gosser, and my family have been absolute lifesavers by keeping me going when things got tough.

Funding for this research was provided by the National Science Foundation (OCE-1801036), NASA Planetary Science and Technology from Analog Research program (80NSSC17K0252), and a NOSAMS graduate student fellowship.

# ABSTRACT

Marine dissolved organic carbon (DOC) is a carbon reservoir comparable in size to all atmospheric $CO_2$ and is composed primarily of refractory material which can be thousands of years old. Circulation through hydrothermal systems has been demonstrated to profoundly alter this material, but the mechanisms that lead to addition, removal, and alteration of DOC are poorly understood. Consequently, the contribution of hydrothermal systems to organic carbon cycling in the deep ocean – and the biological and geochemical processes exhibited at different venting environments – remain highly uncertain.

In January 2020, samples were collected from two hydrothermal vent fields at the Mid-Cayman Rise that have substantial differences in host rock type, depth, and vent fluid temperature. The Von Damm field is situated atop an oceanic core complex and is influenced by ultramafic rocks, whereas the mafic, neovolcanic Piccard field exhibits high temperature black-smoker fluids. Our goal was to determine the different fates of DOC in fluids from these fields and across a wide temperature range of 4 – 393 °C. DOC was characterized by multiple means including isotopically ($^{13}C$, $^{14}C$), by Nuclear Magnetic Resonance (NMR), by Gas Chromatography Mass Spectrometry (GC-MS), and by determining the concentrations of specific compounds of interest such as the organic acid, formate. Our data indicate that at Von Damm, concentrations of DOC isolated by solid phase extraction (SPE-DOC) are inversely proportional to temperature, decreasing from background seawater values while becoming more depleted in $^{13}C$. Organic acid

analysis indicates that formate is the dominant aqueous organic species in Von Damm vent fluids, with concentrations exceeding 800 μM. Dissolved inorganic carbon (DIC) meanwhile, becomes more enriched in $^{13}C$ as formate concentrations increase. These data can be used to determine the isotopic fractionation factor between DIC and formate at Von Damm. At Piccard, most SPE-DOC samples have $\delta^{13}C$ values similar to background seawater and concentrations do not correlate with temperature. NMR analysis of these samples indicates that the hottest Piccard fluids (393 °C) contain a high concentration of a few compounds, unlike background seawater which is composed of thousands of compounds.

The synthesis of these multiple complimentary geochemical data with comparisons to other vent fields help us identify changes in DOC at different hydrothermal systems and the mechanisms at play in the deep carbon cycle. Particularly, that refractory or non-bioavailable DOC is lost during hydrothermal circulation at Von Damm, and labile DOC is being produced from DIC at Von Damm.

# TABLE OF CONTENTS

# LIST OF TABLES

# LIST OF FIGURES

# LIST OF ABBREVIATIONS

Bdl ..... Below Detection Level

Chem ..... Chemistry (HOG sample)

CTD ..... Conductivity, Temperature, Depth (Niskin sample)

DIC ..... Dissolved Inorganic Carbon

DOC ..... Dissolved Organic Carbon

E.M. ..... Endmember

Fm ..... Fraction Modern

GC-MS ..... Gas Chromatography Mass Spectrometry

HOG ..... Hydrothermal Organic Geochemistry (Sampler)

IGT ..... Isobaric Gas Tight

IRMS ..... Isotope Ratio Mass Spectrometry

LV ..... Large Volume (HOG sample)

MCR ..... Mid-Cayman Rise

Mg ..... Magnesium

NMR ..... Nuclear Magnetic Resonance

- COSY ..... $^{1}H$-$^{1}H$ Correlation Spectroscopy
- DOSY ..... $^{1}H$ Diffusion Ordered Spectroscopy
- HMBC ..... $^{1}H$-$^{13}C$ Heteronuclear Multiple-Bond Correlation
- HSQC ..... $^{13}C$-$^{1}H$ Heteronuclear Single Quantum Coherence
- TOSCY ..... $^{1}H$-$^{1}H$ Total-Correction Spectroscopy

NOSAMS.....National Ocean Sciences Accelerator Mass Spectrometry

VDVF.....Von Damm Vent Field

OA.....Organic Acid

PVF ..... Piccard Vent Field

ROV .....Remotely Operated Vehicle

R/V.....Research Vessel

SPE.....Solid Phase Extraction

SPE-DOC..... Solid Phase Extracted Dissolved Organic Carbon

UofSC .....University of South Carolina

VPDB..... Vienna PeeDee Belemnite

# LIST OF SYMBOLS

$X_H$ ..... $\delta^{13}C$ of hydrothermal E.M.

$X_T$ ..... $\delta^{13}C$ of sample

$X_{SW}$ ..... $\delta^{13}C$ of seawater

$A_H$ ..... Carbon concentration of hydrothermal E.M.

$A_T$ ..... Carbon concentration of sample

$A_{SW}$ ..... Carbon concentration of seawater

$F_H$ ..... Fraction of hydrothermal fluid, calculated from Mg

$F_{SW}$ ..... Fraction of entrained seawater, calculated from Mg

$\alpha$ ..... Fractionation factor (R notation)

$\varepsilon$ ..... Fractionation factor ($\delta$ notation)

$C_0$ ..... Initial concentration of DIC

$C_t$ ..... Concentration of DIC at time t

$C_p$ ..... Concentration of DIC lost to make formate

$R_0$ ..... $^{13}C/^{12}C$ ratio of initial DIC

$R_t$ ..... $^{13}C/^{12}C$ ratio of DIC at time t

$R_p$ ..... $^{13}C/^{12}C$ ratio of DIC lost to make formate

f ..... Fraction of remaining DIC at time t

# CHAPTER 1: INTRODUCTION

Hydrothermal environments have been found in every ocean basin and at every active margin, totaling at least 665 active systems as of 2021, yet only 28% of these had been sampled at the seafloor (Beaulieu and Szafranski, 2020). With major impacts on ocean chemical balances (Beaulieu et al., 2013; Tagliabue et al., 2010), the ability to sustain complex biological assemblages independent of sunlight (Reveillaud et al., 2016), and the ability to cause phytoplankton blooms in the surface ocean (Ardyna et al., 2019), hydrothermal environments are an extensive biome with a wide-reaching sphere of influence. However, these are also among the most remote environments on Earth which present numerous scientific and engineering challenges to visit, sample, and understand.

One important area of study at hydrothermal environments is understanding the role they play in the marine carbon cycle. Deep ocean dissolved organic carbon (DOC) is composed of compounds which range from labile (or bioavailable) and to refractory (or not accessible for biological consumption). Hydrothermal environments can expose carbon in circulating fluids to extreme temperatures, pH, or other physiochemical conditions to alter, sequester, or synthesize new labile or refractory DOC. However, much of hydrothermal literature discusses targeted organic compounds such as simple alkanes, organic acids, and aromatics, which leaves a large fraction of hydrothermal DOC unknown (Lin et al., 2019). Many non-targeted or bulk methods used to identify this fraction require large sample volumes. Nuclear Magnetic Resonance Spectrometry

(NMR) for example, requires approximately 5 mg of carbon which can require concentrating over 10 L of sample when deep seawater DOC concentrations seldom exceed 40 μM (Benner et al., 1992; Druffel et al., 1992; Simpson et al., 2011). Similarly, the acquisition of radiocarbon isotope $^{14}C$ data requires 0.5 – 1 L of sample that is subsequently unavailable for other analyses (McNichol and Aluwihare, 2007; Kawagucci et al., 2020).

To remedy challenges in collecting large volumes, samples were collected at two vent fields of the Mid-Cayman Rise using the Hydrothermal Organic Geochemistry sampler (HOG) in January of 2020. Samples came from two geochemically-contrasted fields in close proximity to one another – the ultramafic Von Damm Vent Field (VDVF) and the neovolcanic Piccard Vent Field (PVF; Table 1.1). By performing multiple, complimentary analyses on large volumes of fluid, we can exploit the physical and geochemical differences of each vent field to identify hydrothermal mechanisms that control the fate of carbon.

This work seeks to use these data to address two hypotheses: 1) refractory DOC is lost at both the Von Damm and Piccard vent fields and 2) more labile DOC is produced at Von Damm than at Piccard.

**Table 1.1: Physical and chemical characteristics from the Von Damm and Piccard vent fields.** Values are reported as means of characteristic endmembers from cruise data in McDermott et al. 2015 and McDermott et al. 2018.

| Field (Vent) | Host Rock | Depth (m) | Maximum Temp. (°C) | pH | Cl (mM) | $H_2$ (mM) | $CH_4$ (mM) |
|---|---|---|---|---|---|---|---|
| Deep Seawater | - | - | ~5 | ~8 | 545 | 0 | 0 |
| Von Damm (East Summit) | Mixed Ultramafic-Mafic | ~2,350 | 226 | 5.65 | 649 | 16.2 | 2.62 |
| Piccard (Beebe 1) | Mafic | ~4,957 | 397 | 3.1 | 313 | 18.5 | - |

# CHAPTER 2: BACKGROUND

## *2.1 Hydrothermal Environments*

Hydrothermal circulation, and the spectacular vents associated with them, is not a new field of study. 2017 marked the 40-year anniversary of the confirmation of vents in the Galápagos, yet the high temperature anomalies detected in 1976 were not by pure coincidence (Karl et al., 1980). Studies of groundwater flow date back before the 17$^{th}$ century (Meinzer 1934), with experiments on porous terrestrial and oceanic rock since being performed through benchtop methods and extensive models. Despite all of this, there remain significant unknowns in major marine cycles across many spatial scales. The cycling of carbon – the building block of life – is difficult to model or quantify in all its varieties, species, and compounds in the world's oceans. Perhaps the most mysterious, is dissolved organic carbon (DOC) which is made up of millions of different compounds.

In hydrothermal systems, seawater percolates through permeable rock or faults to react deep under venting locations, experiencing increased heat and pressure (Figure 2.1). Background seawater is recharged into the seafloor, whereupon it begins being altered by biotic and abiotic processes that differ substantially from those in the water column. Chemoautotrophic organisms utilize geochemical energy to metabolize and grow, with dissolved inorganic carbon (DIC) as a carbon source, at temperatures up to 122 °C (Takai et al., 2004; McDermott et al., 2020). Heterotrophic organisms consume organic

compounds and have been found extensively in the subseafloor (Huber et al., 2007; Meyer et al., 2016; Walter et al., 2018; Li et al., 2020).

As fluids percolate deeper into the lithosphere, they are warmed by conductive heating from the mantle, dramatically changing aqueous chemical properties through high-temperature reactions and adding gases (Seewald, 2003). These fluids buoyantly rise and exit the seafloor, often via focused flow in hydrothermal chimneys. They subsequently mix with deep seawater. The pure hydrothermal fluid (prior to mixing with seawater) is referred to as an endmember (E.M.), and can be identified by its low magnesium (Mg) content. Mg reacts with igneous rock at high temperatures and conservatively precipitates out of solution during circulation as smectite or anhydrive clays (Seyfried and Mottl, 1982; Seyfried et al., 1988; McDermott et al., 2018). Mg concentrations of seawater are around 52.5 mmol/kg and decrease to <1 mmol/kg in pure hydrothermal solution (Klein and Langmuir, 1987).

Buoyant hydrothermal fluids return to the surface, where they begin to cool and form chimney complexes or sulfide mounds when they mix with deep seawater. Some of these mounds or chimneys are particularly porous, allowing for deep seawater to become entrained and mix with endmember fluids to exhibit diffuse venting (Ludwig et al., 2006; Webber et al., 2015; McDermott et al., 2020). Resultant endmember or diffuse plumes eventually homogenize with background seawater, contributing hydrothermally altered compounds to seawater DOC.

When distinguishing hydrothermal environments from one another, the host rock – or the types of minerals encountered by circulating fluids – is a common classifying parameter as it is a major control on vent chemistry (Charlou et al., 2010). The host rock

of vent fields is defined by the geomorphology and geologic setting which makes water-rock reactions possible. For example, faulting along slow-spreading ridges can make ultramafic rocks such as peridotites accessible to water; these rocks have water-rock reactions distinct from those of basalts and gabbros (Früh-Green et al., 2003; Kelley et al., 2005; Hodgkinson et al., 2015**)**. Host rock classifications range from mafic to ultramafic at marine spreading centers with differing amounts of basalt, gabbro, and peridotites. Basaltic or mafic hydrothermal systems commonly host reactions that produce $H^+$ and acidify fluids, whereas reactions in ultramafic systems can act to basify them given some other physiochemical constraints (Seyfried and Mottl, 1982; McCollom and Seewald, 2003a).

*2.2 Study Sites of the Mid-Cayman Rise*

The Von Damm and Piccard vent fields are located on the northern half of the ultraslow-spreading Mid-Cayman Rise, with Piccard located closest to the Oriente Fault Zone (Figure 2.2). The fields are relatively recent discoveries, originally detected by plume signatures in 2010 and visually confirmed later that year (German et al., 2010; Connelly et al., 2012). Locations are not extensively sedimented, with vent locations covered by sulfides and chimney talus. Cores taken from the North of the venting fields at a depth of 1 km suggest contribution of some terrigenous matter (Peters et al., 2000). At both locations, *Rimicaris hybisae* shrimp are the dominant macrofaunal signature present near locations of fluid flow. *Methanothermococcus* and *Sulfurovum* are the dominant archaeal and bacterial communities present at each vent field, capable of utilizing $H_2$ and $H_2S$ of venting fluids (Reveillaud et al., 2016).

Ultramafic environments exhibit geochemistry distinct from perceptions of venting environments, often lacking distinctive “black smoker” plumes at lower temperature regimes. The host rock of these systems is often an assemblage of peridotites or gabbros, which contain the mineral olivine (Palandri and Reed, 2004). Olivine is responsible for the reaction serpentinization, where an olivine-containing rock is transformed into serpentinites by equation 2.1 below (McCollom and Bach, 2009):

$$Mg_{1.8}Fe_{0.2}SiO_4 + 1.37H_2O \rightarrow 0.5Mg_3Si_2O_5(OH)_4 + 0.3Mg(OH)_2 + 0.067Fe_3O_4 + 0.067H_2$$

Olivine Serpentine (Eq. 2.1)

Serpentinization is an exergonic process which produces $H_2$ and sequesters large amounts of $H_2O$ to expand and fracture rocks in ultramafic environments (Perner et al., 2013). The cracking of rock along the fluid pathway creates more surface area for further serpentinization and potentially convoluting flow pathways (MacDonald and Fyfe, 1985; Palandri and Reed, 2004). Ultramafic sites such as the Lost City are situated on oceanic core complexes which have extensive faulting to permit such water-rock reactions (Kelley et al., 2005; Lang et al., 2021). The $H_2$ produced from serpentinization creates reducing conditions in vent fluids, capable of converting $CO_2$ to $CH_4$ or small hydrocarbons (Equation 2.2, 2.3; McCollom and Seewald, 2007; Proskurowski et al., 2008; McCollom and Bach, 2009).

$$2(FeO)_{rock} + H_2O \rightarrow (Fe_2O_3)_{rock} + H_2 \quad (2.2)$$

$$CO_2 + H_2 \rightarrow CH_4 + C_2H_6 + C_3H_8 + C_nH_{n+2} \ldots + H_2O \quad (2.3)$$

Given alkaline conditions and high concentrations of $H_2$, the single-carbon organic acid formate can be thermodynamically favored over inorganic carbon at some

venting environments (Equation 2.4; McCollom and Seewald, 2003a; Lang et al., 2010; McDermott et al., 2015).

$$CO_2 + H_2 \leftrightarrow HCOO^- + H^+ \quad (2.4)$$

Formate

The Von Damm vent field (VDVF) is an ultramafic vent system perched atop an oceanic core complex, Mount Dent, at a depth of around 2,350 m approximately 13 km west of the axial valley (Connelly et al., 2012). Though the VDVF is estimated to be 1 to 2 Ma old, observed venting activity is akin to the latest stage of hydrothermal activity over tens of thousands of years (Hodgkinson et al., 2015). Clear venting fluids (Figure 2.2) emanate from the field in two distinct talc mounds to the Northwest and Southeast, with some temperatures exceeding 150 °C. These locations are geochemically distinct and are described in this work as the Northern and Southern Mounds. There are many locations of proposed diffuse flow across the entire field due to faulting and serpentinization associated with oceanic core complexes (Kelley et al., 2005; Hodgkinson et al., 2015; Lang et al., 2021). Fluid pH (~5.9) is higher than observed at the nearby Piccard field, though still acidic relative to seawater (~8.1). Methane and hydrogen (2.8 mM and 19 mM respectively) are elevated following the association of ultramafic systems (McDermott et al., 2015). The delicate chimneys at VDVF are composed of talc residing on conical mounds of chimney talus, which are largest at the southern end of the field but are increasingly inactive in a southerly direction (Hodgkinson et al., 2015).

Mafic or basalt-hosted vent fields are perhaps the best documented in literature, with distinctive black plumes and hot, acidic venting fluids. At unsedimented spreading centers, fluid penetrates fresh ridge basalts and gabbros to percolate deep into the crust.

Water, heated by conductively heated basalts, reacts with basalt surfaces through a series of alteration or dissolution reactions. The alteration or dissolution of basalt lowers the pH of fluids to be characteristically acidic when metal sulfides form, while also enriching the fluid with elements such as Fe, Ca, K, Mn, and Zn (Seewald and Seyfried, 1990). Similarly, water-rock reactions of ferrous iron and precipitated metal sulfides in mafic circulation pathways allow for generation of hydrogen gas and hydrogen sulfide (Perner et al., 2013; Scheuermann et al., 2020). Altered endmember fluids are physiochemically distinct from deep background seawater, and buoyantly rise to mix with deep seawater at the venting orifice. Within these endmembers, concentrations of hydrogen ($H_2$) and hydrogen sulfide ($H_2S$) are elevated from background seawater, therefore allowing for chimneys of metal sulfides (pyrite) to form while also being extremely desirable for microbial metabolisms (Webber et al., 2015; Reveillaud et al., 2016; Lang et al., 2021).

To the north of Von Damm, the mafic Piccard vent field is situated almost directly on the axial valley at a depth of 4,900 – 5,000 m, making it the deepest known high-temperature vent field (Connelly et al., 2012; McDermott et al., 2018). Venting fluids are abundant in dissolved trace metals and sulfides, causing metal-sulfide chimneys to form at venting orifices and giving plumes a distinctive 'black smoker' appearance (Figure 2.2). Venting is most pronounced at the center and southern sides of the field, with smaller venting areas to the north and east. Located centrally at Piccard is a complex of vents referred to as Beebe 1 – 5 and are the hottest vents of the entire vent field. Observed hydrogen values are higher than those at ultramafic environments, though methane concentrations are relatively low (~0.1 mM; McDermott et al., 2018). Observed hydrogen concentrations (19.9 mM) exceed those of hydrogen sulfides (12 mM), which is

abnormal for mafic systems and may be due to temperature and pressure conditions (Foustoukos et al., 2009; McDermott et al., 2018; Scheuermann et al., 2020). The crust at the spreading center is only 2 – 3 km thick, with extremely hot venting fluids of up to 400 °C (Webber et al., 2015). Fluids from these vents have chlorinity lower than background seawater, as well as trace metal ratios that confirm they reach temperatures and pressures sufficiently elevated to cause phase separation (Table 1.1; Von Damm et al., 2003; Connelly et al., 2012; Webber et al., 2015; McDermott et al., 2018). Supercritical water occurs at locations of high heat (407 °C) and pressure (298 bar) and can behave as a solvent, reactant, catalyst, proton donor, complexing agent or hydration agent for numerous organic reactions (Von Damm et al., 1985; Bischoff, 1991; Savage, 1999; Konn et al., 2011). These supercritical conditions cause phase separation, where a measurable Cl-depleted vapor phase is distinguished from a Cl-enriched brine (Simoneit, 1993; Butterfield et al., 1994).

### *2.3 Dissolved Organic and Inorganic Carbon*

DOC is operationally defined as the fraction of organic compounds that pass through a submicron filter and has many high and low-molecular weight constituents (Chen et al., 2016; Zigah et al., 2017; Shen and Benner, 2018). The 662 Pg of marine dissolved organic carbon in the world's oceans can be defined as biochemically reactive "labile" or non-reactive "refractory" fractions (Jiao et al., 2010; Hansell et al., 2012). Labile DOC is utilizable by microorganisms and is altered over timeframes of years to hundreds of years. The refractory component of DOC is not available to major biogeochemical cycles and has been identified as 4,000 years or older below 1000 m

depth (Druffel et al., 1992; Hansell et al., 2012; Lang et al., 2019; Lin et al., 2019). For both fractions of DOC, however, data regarding their distributions and abundances are underdeveloped in the purview of hydrothermal vents (Lin et al., 2015).

One group of compounds that contributes to labile DOC are organic acids (OAs). OAs function as intermediates of biochemical reactions such as methanogenesis and sulfidogenesis with many synthesis pathways (Martin et al., 2008; Lang et al., 2018; Lang et al., 2019). Simple organic acids, such as formate and acetate, may be synthesized or decomposed abiotically as functions of pH, hydrogen activity, or temperature (Figure 2.3). As such, OAs can be insightful in determining the role of thermal decomposition on organic matter or supporting microbes as a metabolic substrate in many marine environments (McCollom and Seewald, 2003a; McCollom and Seewald, 2003b).

In contrast to DOC, dissolved inorganic carbon (DIC) consists of only a few compounds and speciation is primarily determined by pH (Figure 2.3). Carbonate ($CO_3^{2-}$), bicarbonate ($HCO_3^-$), carbonic acid ($H_2CO_3$), and carbon dioxide ($CO_2$) make up a carbon pool that can be biotically and abiotically transformed into organic compounds via a variety of reactions. Inorganic carbon is the carbon source used for the biological synthesis of organic carbon and is enormously abundant (37,400 Pg of carbon; Jiao et al., 2010), such as $CO_2$ in photosynthesis. In hydrothermal environments, chemosynthesis is the dominant biological control on converting DIC to DOC, where abundant amounts of $H_2$ and $H_2S$ are available as electron donors to reduce DIC into organic molecules (Lin et al., 2012; Lang et al., 2019). $CO_2$ is often seen at elevated levels in the acidic fluids of black smokers, which are often mafic systems, whereas $HCO_3^-$ and $CO_3^{2-}$ are more

common at ultramafic sites where pH is more basic (Seyfried and Mottl, 1982; Lang et al., 2010).

*2.4 Hydrothermal Addition and Removal of DOC*

The chemical and physical conditions of hydrothermal systems are major controls on alteration of DOC. Abiotic synthesis reactions can form organic compounds from inorganic carbon in the absence of life. For example, reducing conditions of hydrothermal environments are favorable for Fischer-Tropsch Type (FTT) synthesis – a reaction to form long-chain alkanes (McCollom et al., 1999a; McCollom and Seewald, 2003a; Lang et al., 2010). At the Mid-Cayman Rise, formate has been proposed to be generated in the subsurface when $H_2$-rich fluids mix with entrained deep seawater with abundant DIC, allowing for abiotic synthesis of the organic acid (Equation 2.4; Shock and Schulte, 1998; McCollom and Seewald, 2003a; Seewald et al., 2006; Shock and Canovas, 2010; McDermott et al., 2015).

Organic compounds can also be added by the microbial communities that proliferate in hydrothermal systems. Microbial populations of hydrothermal environments operate at conditions where sunlight is absent, oxygen is depleted relative to surface water, and electron donors are abundant. As such, chemosynthetic organisms use DIC or labile fractions of DOC to metabolize and synthesize new biomass (Jiao et al., 2010; Lang et al., 2019).

A different suite of reactions can cause the removal of DOC. The elevated temperatures of hydrothermal fluids are favorable to overcome kinetic reaction barriers. For example, elevated temperatures allow for pyrolysis or cracking reactions which act to

break compounds down into smaller compounds or more stable compounds such as simple alkanes or aromatic molecules (Kvenvolden and Simoneit, 1990; McCollom et al., 1999b; Seewald, 2003).

Sorption, or the "sticking" of organic compounds to rocks, is a subsurface process that may act to remove DOC during hydrothermal circulation. In this context, sorption is more likely at lower temperatures and acidic conditions, though the sorptive potential of different igneous minerals is highly unknown (Lang et al., 2006). Clays, however, are better understood and have been identified as biproducts of hydrothermal alteration in a variety of environments (Seyfried and Mottl., 1982; Lévy et al., 2020; Tudor et al., 2021). Clays, such as smectite and kaolinite, have been observed to sorb DOC of different sizes depending on availability of iron oxides and surface areas (Saidy et al., 2013).

The biotic process of consuming DOC, heterotrophy, is a potential sink of DOC that may be observed in DOC concentrations of hydrothermal fluids (McCarthy et al., 2010; Lang et al., 2006; Hawkes et al., 2015; Walter et al., 2018). However, biological communities also act to transform characteristics of DOC, with biologically derived DOC being discharged into deep seawater (McCarthy et al., 2010; Walter et al., 2018; Lin et al., 2019). Different microbial populations have been identified at distinct temperature regimes of hydrothermal environments, which may impact how extensive biological contributions are to altered fluids at different vents (Anderson et al., 2013; Reveillaud et al., 2016; Anderson et al., 2017).

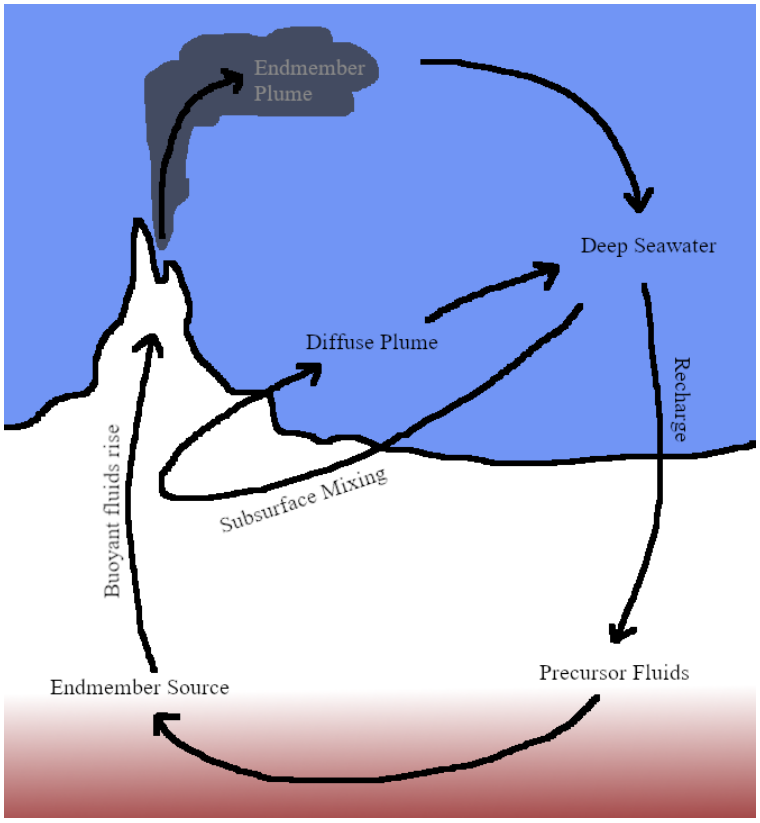


**Figure 2.1: A simplified sketch of hydrothermal circulation pathways.**

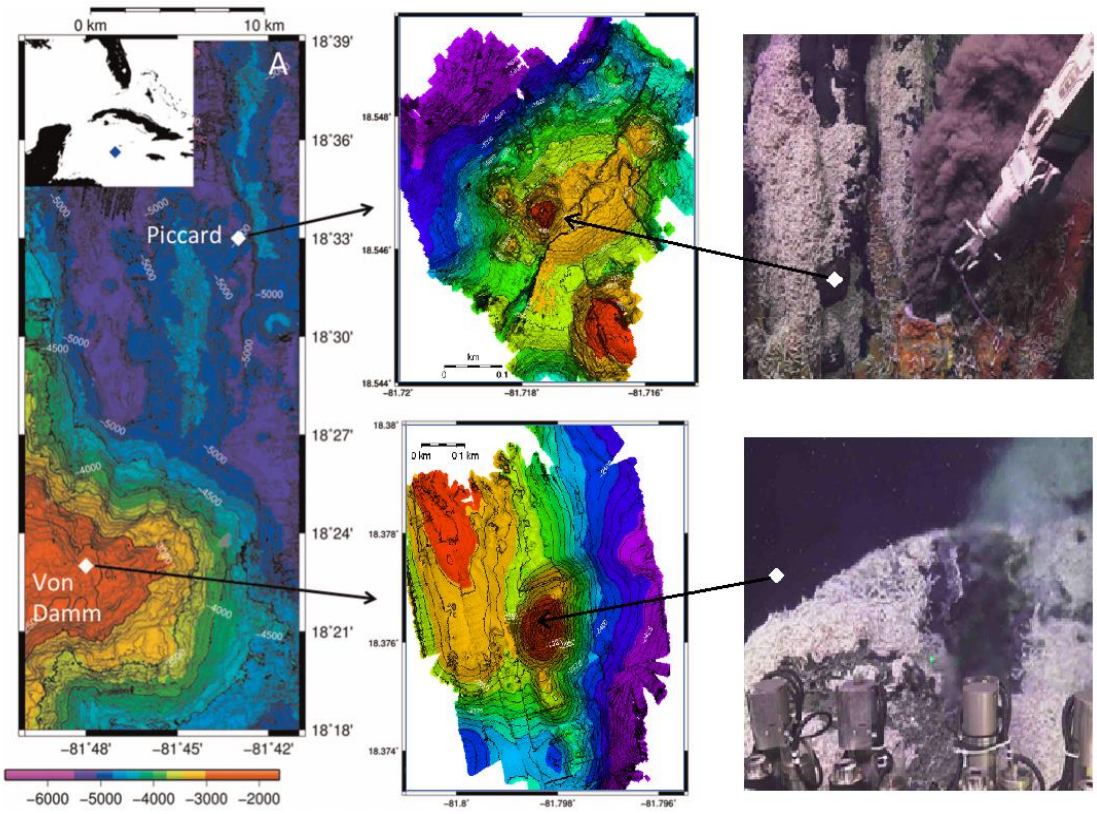


**Figure 2.2: Bathymetry and visual representations of the Piccard (top panels) and Von Damm (bottom panels) at the Mid-Cayman Rise**. Modified from Bennett et al. 2015.

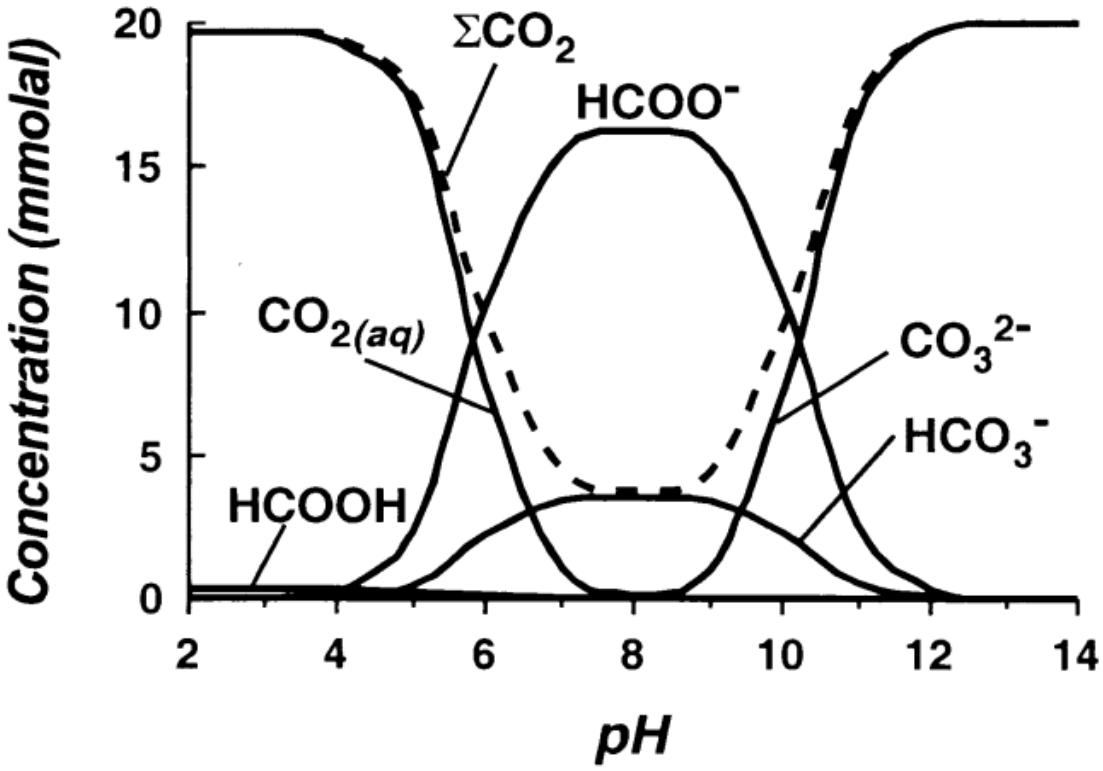


**Figure 2.3: Modeled dissolved inorganic carbon species, formate, and formic acid as a function of pH at $aH_2$ of 40 mmolal, 175°C.** Dotted line is representative of total dissolved inorganic carbon. Modified from McCollom and Seewald. 2003a.

# CHAPTER 3: METHODS

*3.1 Sample collection*

Samples were collected at the Mid-Cayman Rise during January 2020 on the R/V *Atlantis* with the remotely operated vehicle (ROV) *JASON II* (Table 3.1). Background seawater samples were acquired by Niskin/CTD Rosette casts and hydrothermal fluid samples were collected with the Hydrothermal Organic Geochemistry (HOG) sampler constructed at the University of South Carolina (Lang and Benitez-Nelson, 2021; Figure 3.1). The HOG, mounted on the undercarriage of *JASON*, shunts sample fluid through a main conduit; samples are collected into acid washed Kynar® bags by positive displacement (10% HCl soak overnight, followed by thorough rinsing, overnight Milli-Q soak, and further rinsing; Figure 3.1). Samples can be collected into seven 2 L chambers and six 9 L chambers. Sample bags, unlike Isobaric Gas Tights, are not pressurized and thus allow for degassing of volatiles within samples. The HOG features an *in situ* NKE Instrumentation Temperature Probe (P/N S2T6000-Ti-DH; P/N 60-07-326-002) connected to the ROV Jason that can be monitored in real time.

Once on deck, samples were immediately subsampled for shipboard determination of sulfide concentrations and pH. Sample bags were further subsampled for nutrients, trace metals, total hydrolysable amino acids/organic acids, unfiltered DOC, and major ions. Nutrients were acidified with two drops of trace-metal grade HCl prior to storage. Subsampled aliquots (excluding trace metals and major ions) were frozen at -16

°C until analysis. All fluids collected via the HOG followed the same general protocols with the exception of J-1242 at the Beebe vents of the Piccard field, where the HOG intake line was swapped out for a longer, high-temperature titanium line and temperature was determined using a temperature probe from the ROV.

Sulfides were determined by a calorimetric method that utilizes a dye of iron (III) chloride and N,N-dimethyl-p-phenylenediamine dihydrochloride (Cline, 1969). Sample aliquots (5 mL) were spiked with 500 μL of dye. Approximately 15 minutes were allowed to pass for the reagent to bind to sulfides, after which 100 μL was transferred to 5 mL of 0.6 N HCl, shaken, and read at 670 nm on a Hach Model DR/2400 spectrophotometer. Concentrations were then calculated from their corresponding standard curve from earlier that day. Standard curves were made from helium-purged MilliQ $H_2O$ (2 ppb carbon) and sodium sulfide. Standards were compared to a sulfide electrode method used by IGT groups from the Woods Hole Oceanographic Institution and the University of Bergen.

For all dives except J-1235, the pH for HOG samples was measured by a glass Ag/AgCl combination reference electrode (25 °C, 1 atm) by science party members from Bridgewater State University.

Collected geochemical conditions from each site (temperature, pH) were used to constrain Bjerrum equilibrium plots of DIC ($CO_2$, $H_2CO_3$, $HCO_3^-$, $CO_3^{2-}$), formate ($HCOO^-$), and formic acid (HCOOH) speciation after the conventions of McCollom and Seewald, 2003.

*3.2 Solid Phase Extraction*

Aliquots for Solid Phase Extraction (SPE) were filtered with a 0.2 μm Acropak filter (P/N 12039 ID 7932) to remove particulate organic carbon and sulfides. The filtered sample was then acidified to a pH of around 2 to maximize recovery of organic compounds (Dittmar et al., 2008). Up to 1 L of acidified sample was passed over individual Bond Elut PPL cartridges (1 gm, 6 mL, Agilent P/N 12255002), with 3 – 5 replicate cartridges taken for large volume (LV) samples at each site (Table 3.1). Prior to drying and storage, cartridges were flushed with acidified MilliQ water to remove salts. Sample cartridges were dried and stored at -16 °C until being eluted with 8 mL of OmniSolv high-purity methanol. Eluted samples were evaporated to 2 mL volume and 50 μL aliquots were transferred to prepared Labco Exetainer® vial for the analysis of $\delta^{13}C_{SPE\text{-}DOC}$ values and SPE-DOC concentrations. The remainder was frozen at -15 to -18 °C until combined and dried for NMR analyses. Blanks were prepared by passing high-purity MilliQ $H_2O$ through a new 0.2 μm Acropak filter and over SPE cartridges for elution and aliquoting.

*3.3 Isotope Ratio Mass Spectrometry*

Aliquots of the eluted SPE samples were prepared for isotope ratio mass spectrometry (IRMS) following a modified procedure from Lang et al. (2012). Aliquots were dried under $N_2$ gas to remove the MeOH before adding 1 mL of saturated sodium persulfate oxidizing solution ($Na_2(SO_4)_2$). The sealed vials were then purged with high purity helium for 5 minutes at 100 mL $min^{-1}$ before heating at 100°C for 1 hour to convert DOC to $CO_2$. The resultant isotopic signature was analyzed using a GasBench II

preparation device connected to a ConFlo IV interface and a Delta V Plus isotope ratio mass spectrometer (Thermo Fisher Scientific). A methanol blank was prepared and was subtracted from sample IRMS peak areas.

Carbon isotopes are represented by $\delta^{13}C$ in per mil notation (‰) relative to VPDB (Vienna Pee Dee Belemnite, $R_{Standard} = 0.0112372$) standard where R represents the ratio between $^{13}C$ and $^{12}C$ and the VPDB:

$$\delta^{13}C = 1000 * \left(\frac{R_{Sample}}{R_{Standard}} - 1\right) (‰) \qquad (3.1)$$

$\delta^{13}C$ values were determined using standards prepared over a concentration range that bracketed the samples and had been previously calibrated to IAEA standards (Sucrose, -12.4 ‰; Phthalic Acid, -33.6 ‰) and are also reported versus VPDB (Lang et al., 2012).

*3.4 Nuclear Magnetic Resonance*

SPE extracts from venting locations that had of similar temperatures, sulfide concentrations, SPE $\delta^{13}C$, and SPE-DOC concentrations were combined to obtain sufficient carbon for Nuclear Magnetic Resonance (NMR) spectroscopy at the University of Toronto, Scarborough. Extract combinations were fully dried under $N_2$ prior to shipment. A SPE blank was prepared by passing MilliQ $H_2O$ over an 0.2 μm Akropak filter and a PPL SPE column and eluted similarly to field samples described in Section 3.2. NMR analyses were performed with a Bruker Ultrashield 500MHz Avance III Solution-State NMR using a methanol-d4 solvent. Samples were subjected to 1D $^{1}H$ NMR, $^{1}H$-$^{1}H$ Total-Correction Spectroscopy (TOSCY), $^{13}C$-$^{1}H$ Heteronuclear Single

Quantum Coherence (HSQC), $^{1}H$-$^{13}C$ Heteronuclear Multiple-Bond Correlation (HMBC), $^{1}H$-$^{1}H$ Correlation Spectroscopy (COSY), and 2D $^{1}H$ Diffusion Ordered Spectroscopy (DOSY) (Simpson et al., 2017).

*3.5 Gas-Chromatography Mass Spectrometry*

The samples analyzed non-destructively for NMR were transferred to a reaction vial, dried under $N_2$ gas, and then dissolved in Fisher BSTFA+TMCS (10%, PN: PI38840) to derivatize samples for GC-MS. When fully dissolved, samples were frozen until ready for GC-MS analysis with separation on an Agilent J&W GC HP-5MS UI capillary column (PN: 19091S-433UIE) and an Agilent Technologies 5975 inert XL Mass Selective Detector with a Helium carrier gas. The GC oven was heated from an initial temperature of 70 °C to 150 °C at 15 °C per minute, and then to 300 °C at 5 °C per minute. A 5-point standard curve of a C7-C30 alkane series (PN: 49451-U, Sigma Aldrich) was used to quantify peak areas. All samples were processed at the University of South Carolina Mass Spectrometry Center.

An external standard of a potential compound found in the fluids, diethylene glycol monoethyl ether (trade name carbitol), was also analyzed. The standard was prepared from 100 μL of 99% diethylene glycol monoethyl ether (CAS 111-90-0) in 10 mL of OmniSolv methanol. A further 150 μL of this solution was diluted in another 10 mL of methanol to acquire a mass concentration of 149.85 ng carbitol per μL to be in range of the detector and standards. Peak areas for these carbitol standards were then compared to SPE elutions of 10, 25, and 50 mL extracted volumes to compare concentrations of carbitol at Beebe 4 of the Piccard vent field. The resulting spectrometry

was analyzed using the NIST14 chemical library to identify common compounds in the SPE extracts.

*3.6 Dissolved Inorganic Carbon*

DIC was subsampled from the HOG bags by transferring 0.5 mL of filtered sample (0.2 μm) to capped Labco Exetainer® vials previously prepared with 100 μL concentrated $H_3PO_4$ and flushed with helium. DIC samples were run at the University of South Carolina using the same GasBench II and ConFlo IV configuration as in the SPE-DOC method (section 3.2), with standards of potassium bicarbonate ($KHCO_3$, $\delta^{13}C$ = -38.1 ‰) and lithium carbonate ($Li_2CO3$, $\delta^{13}C$ = -1.1 ‰) to identify the $\delta^{13}C$ isotopic composition and DIC concentration.

*3.7 Organic Acids*

Organic acids were measured using a modified method from Albert and Martens (1997). A 1 mL aliquot was transferred to a freshly combusted 4 mL vial then spiked with 100 μL of 1:1 pyridine and 12 N Fisher TraceMetal$^{TM}$-grade HCl. Aliquots were vortexed and then bubbled under $N_2$ for 2 minutes. Once all aliquots had been bubbled under $N_2$, 100 μL of 0.1 M NPH solution (189.6 mg 2-nitrophenylhydrazine hydrocholoride in 10 mL 0.25 M HCl) and 100 μL of 0.3 M EDC solution (575.1 mg 1-(3-dimethylaminopropyl)-3-ethylcarbodiimide hydrochloride in 10 mL of MilliQ $H_2O$) were added to the samples before vortexing and allowing to react for 90 minutes. Thereafter, 100 μL of 40% KOH (4 g KOH in 10 mL MilliQ $H_2O$) was added. Samples were vortexed and placed on 70 °C heating blocks for 10 minutes. Concluding the

derivatization, samples sat overnight at room temperature in the dark and were filtered into 2 mL Thermo autosampler vials the next day using VWR 0.2 μm PES filters (PN: 28145-501). Samples were analyzed using a Thermo Ultimate 3000 UHPLC with a UV Vis detector and Thermo Scientific Acclaim Organic Acid silica column, along with a mobile phase of 2.5% n-butanol, 25 mM sodium acetate, 2 mM tetrabutylammonium hydroxide 30-hydrate, and 50 mM tetradecyltrimethylammonium bromide in MilliQ water acidified to pH = 4.5 using phosphoric acid. For each run, 5-point calibration curves were prepared by using a 1 mM mixed organic acid standard consisting of formate, acetate, propionate, butyrate, and lactate.

*3.8 Bulk DOC Analyses*

Whole fluid samples (1 L) were processed at the National Ocean Sciences Accelerator Mass Spectrometry (NOSAMS) center for bulk carbon analyses following a method similar to that outlined by Beaupre et al. 2007. DOC concentrations (DOC), the $^{13}C$ of DOC ($\delta^{13}C_{DOC}$) and the $^{14}C$ of DOC ($\Delta^{14}C_{DOC}$) were analyzed. Samples were acidified with irradiated phosphoric acid and purged with helium to remove DIC. DOC was subsequently oxidized by high-intensity UV irradiation for 4 hours. DOC concentrations were ascertained by resultant $CO_2$ measured by a manometer using a 1.03 g/mL density to convert to μM. $CO_2$ was also sampled for $\delta^{13}C$ by isotope ratio mass spectrometry, with the remainder converted to graphite for $\Delta^{14}C$ by accelerator mass spectrometry. Radiocarbon values are represented as fraction modern (Fm) to account for decay from bomb carbon (Reddy et al., 2002; Reimer et al., 2004).

Samples were also processed for bulk DOC concentrations at the University of South Carolina. Samples were thawed and transferred to autosampler vials, then acidified using 50 µL of 12N trace metal HCl. Aliquot DOC concentrations were analyzed on a Shimadzu total organic carbon TOC-V analyzer equipped with an autosampler. Deep seawater certified reference standards were injected to monitor the accuracy and consistency of the analysis.

*3.9 Major Ions and Endmembers*

Aliquots were analyzed for major ions (Mg, Ca) by inductively coupled plasma mass spectrometry (ICP-MS) at the Woods Hole Oceanographic Institution. Additional samples were also analyzed by ICP-MS at the University of South Carolina Mass Spectrometry Center.

During sampling, seawater is inevitably entrained at the point of sample collection. The geochemical composition of the hydrothermal fluid can be determined by mass balance if species mix conservatively. Since deep seawater contains high Mg value (52.5 mM) and hydrothermal fluids contain low Mg values (<1 mM), the contribution of seawater to any sample can be determined. Hydrothermal endmembers (E.M.) were calculated using a linear two-fluid mixing model using Mg values from CTD casts (AT42-22-CTD2-B11, AT42-22-CTD3-B1, and AT42-22-CTD5-B18) and HOG background samples (J-1244-Chem-7, J-1244-LV24) to represent deep seawater. A Mg concentration of 0 mmol/kg to represent a pure endmember (Von Damm et al., 1985), where the term *A* represents the concentration of the species, and *F* represents the fraction of seawater (*SW*) or hydrothermal E.M. (*H*) in the collected sample (*T*; Eq. 3.2).

$$A_H = \frac{A_T - A_{SW} F_{SW}}{F_H} \quad (3.2)$$

Endmember isotopes were calculated by assuming conservative mixing of two fluids of distinct isotopic composition, where *X* represents the $\delta^{13}C$ of the carbon species (Eq. 3.3). These endmember calculations help correct for seawater entrainment during sampling.

$$X_H = \frac{X_T A_T - X_{SW} A_{SW} F_{SW}}{A_H F_H} \quad (3.3)$$

*3.10 Nutrient Analyses*

Analyses of nutrient concentrations ($PO_4$, $NO_3$, $NO_2$, $NH_4$) were performed by the Marine Chemistry Laboratory at the University of Washington. Colorimetric analyses and calibration follow WOCE Hydrographic protocols and were conducted on a SEAL Analytical AA3 HR AutoAnalyzer.

**Table 3.1: Summary of samples collected by Niskin and the HOG at the MCR on AT42-22.**

| Field | Vent Name | Dive Number(s) | Maximum Temp. (°C) | HOG SPE Count* | HOG Chem Bag Count |
|---|---|---|---|---|---|
| Deep Seawater | - | CTD-002<br>CTD-003<br>CTD-005<br>J-1244 | 4 | 2 | 1 |
| Von Damm | Arrow Loop | J-1243 | 139 | - | 3 |
| | Bartizan | J-1244 | 137 | 1 | 2 |
| | Mustard Stand | J-1243 | 108 | 1 | 3 |
| | Old Man Tree | J-1238<br>J-1243 | 119 | 1 | 4 |
| | Ravelin 1 | J-1244 | 144 | | 2 |
| | Ravelin 2 | J-1238 | 113 | 1 | 3 |
| | Shrimp Hole | J-1244 | 22 | 1 | 2 |
| | White Castle | J-1235 | 179 | 1 | 3 |
| | X-18 | J-1235 | 62 | 2 | 4 |
| Piccard | Beebe 4 | J-1242 | 393 | 1 | |
| | Hot Chimlet | J-1239 | 98 | 1 | 3 |
| | Lots of Shrimp | J-1241 | 36 | 1 | 5 |
| | Shrimpocalypse | J-1240<br>J-1242 | 94 | 1 | 5 |
| | South of Hot Chimlet | J-1242 | 39 | - | 3 |
| | South of Lung Snack | J-1242 | 57 | - | 2 |

* Denotes large-volume (11 L) Keika bags which underwent SPE.

**Figure 3.1: The HOG sampler (left) with large-volume Keika sample bags (right) during AT42-22.**

# CHAPTER 4: RESULTS

*4.1 General Geochemistry and Nutrients*

The physiochemical characteristics of samples collected during AT42-22 differed between the Von Damm Vent Field (VDVF) and the Piccard Vent Field (PVF). Sample pH varied at the VDVF from 5.6 to 7.1 with the lowest pH recorded at White Castle (Table 4.1). PVF samples had pH values between 4.7 to 6.4, with Beebe 4 having the lowest value (Table 4.2).

Magnesium concentrations were acquired for three samples of background seawater: 51.4 mmol/kg (J-1244-Chem-7), 52.0 mmol/kg (CTD cast 2, bottle 11), and 53.2 mmol/kg (CTD cast 5, bottle 18). Magnesium values from hydrothermal fluids were lowest at Old Man Tree on the Southern VDVF mound (11.8 mmol/kg, T=122 °C, J-1238-Chem-6) and were highest at the Lots of Shrimp at PVF (52.9 mmol/kg, 35 °C, J-1241-Chem-3).

Measured $H_2S$ concentrations at the VDVF were lowest at Shrimp Hole (0.2 mM, 20.9 °C) and highest at Old Man Tree (2.3 ± 0.1 mM, 122 °C). For hot locations (T > 100 °C), $H_2S$ and $PO_4$ were higher at the Southern Mound than the Northern Mound of the VDVF. Sulfide concentrations at the PVF ranged from 0.0 to 4.5 mM; lowest at Lots of Shrimp (0.1 mM, 36 °C) and highest at Beebe 4 (3.7 ± 0.5 mM, 393 °C).

The highest measured values for nitrate ($NO_3^-$) at Von Damm and Piccard were at X-18 (10.3 μM; 37 °C) and South of Hot Chimlet (16.7 μM, 35 °C), respectively (Table

4.1, Table 4.2). Ammonium ($NH_4^+$) was highest at Beebe 4 (23.9 μM) and X-18 (23.0 μM). Our deep seawater sample contains detectable ammonium (4.95 μM, 4 °C) as well as nitrate concentrations (8.41 μM) lower than expected for deep seawater. Since this sample was collected using the HOG sampler that also collected high ammonium, low nitrate hydrothermal samples on the same dive, there is the possibility that these values reflect that the intake line was not sufficiently flushed prior to collecting the seawater sample. . Hydrothermal fluids have been demonstrated to reduce nitrate to ammonium due to abiotic and biotic processes (Bourbonnais et al., 2012). Previous studies report a deep seawater nitrate value of between 23.8 and 25.0 μM from 2,500 m depth in the Caribbean sea (Morrison and Nowlin, 1982). Ammonium concentrations are not expected to exceed 1 μM in the deep ocean (Watson et al., 2005). Reduced nitrate and elevated ammonium were also evident at some sites were at temperatures below 40 °C. This also included Lots of Shrimp at the PVF ($NO_3^-$ = 14.6 μM, $NH_4^+$ = 9.3 μM, 36 °C). The highest value for nitrite ($NO_2^-$) was also at Lots of Shrimp (0.2 μM). Of the 48 samples tested for nutrients, nitrite was only detectable (>0.001 μM) in 17 of them.

*4.2 Organic Acids*

For all organic acids (formate, acetate, lactate, butyrate, propionate), only formate was detected (> 5 μM). Formate was highest at Von Damm, especially the Southern Mound, where the highest values were observed at Ravelin 2 which were as high as 931 μM (Table 4.3). This was nearly 700 μM greater than the observed concentration of formate at Ravelin 1 (up to 246 μM formate). At cooler locations at the Southern Mound, such as X-18 and Shrimp Hole (T ~ 35 and 20 °C), formate was below detection. The

Northern Mound did not reach concentrations as high as the Southern Mound, instead ranging between 117 and 207 μM (Figure 4.1).

Formate was not detectable in Piccard fluids with the exception of one venting location. The only site where formate was detectable was South of Lung Snack with a concentration less than 30 μM.

*4.3 Solid Phase Extraction Dissolved Organic Carbon Concentration and Isotopes*

Solid Phase Extraction was performed on a total of 66 PPL cartridges for deep seawater and 11 distinct venting locations at Von Damm and Piccard (Table 4.4). Deep Caribbean seawater had a SPE-DOC concentration of 27.7 ± 3.5 μM, and $\delta^{13}C_{SPE}$ of -22.3 ± 0.6‰. Concentrations of SPE-DOC and isotopic values decreased at Von Damm from background seawater (Figure 4.2, Figure 4.3). SPE-DOC decreased conservatively with decreasing Mg ($r^2 = 0.95$), though $\delta^{13}C$ values were not as clear (Figure 4.2b). The hottest location, White Castle (T ~ 179 °C), had the lowest SPE-DOC (3.4 ± 1.3 μM) and the lowest $\delta^{13}C_{SPE}$ (-24.2 ± 0.9 ‰), whereas Shrimp Hole (T ~ 22 °C) had a SPE-DOC of 26.1 ± 3.3 μM and $\delta^{13}C_{SPE}$ of -22.3 ± 0.5, which were nearly identical to that of seawater (deviations of 0.8 μM and 0 ‰, respectively; Table 4.4).

Fluids from much of the PVF had SPE values of comparable concentration and $\delta^{13}C$ isotopic signature to that of seawater (Figure 4.3). Cooler locales (T < 393 °C) most resembled background seawater as indicated by SPE-DOC, $\delta^{13}C$, and Mg. Beebe 4 had high concentrations of SPE-DOC (32.1 μM) and low $\delta^{13}C_{SPE}$ values (-25.2 ± 0.7 ‰) compared to the rest of the data collected from the MCR. SPE-DOC was also highly variable at Beebe 4, with a standard deviation of 17.1 μM.

*4.4 Bulk DOC and Radiocarbon Analyses*

Bulk DOC analyses performed at the University of South Carolina for 3 deep seawater samples, 10 Von Damm samples, and 8 samples from Piccard (Table 4.5). DOCs in background seawater were assessed on two CTD samples as well as one HOG sample. Background concentrations varied from 43.8 to 46.5 μM. At the VDVF, DOC concentrations were higher on average at the Southern Mound (411.2 ± 351.2 μM), particularly the Ravelin 2 (up to 957.5 μM) and Old Man Tree sites (up to 645.7 μM), while DOC concentrations at the Northern Mound (205.2 ± 42.9 μM) did not exceeding 254.6 μM. Variability of the Southern Mound cannot be attributed entirely to temperature. Cooler sites, such as X18 (33 – 66 °C; up to 65.1 μM) and Shrimp Hole (19 °C; up to 53.6 μM), do have lower formate concentrations than the higher temperature locations. But there is also significant variability in the high temperature sites as Ravelin 1 and 2 differed by nearly 600 μM despite similar temperatures of 144 and 112 °C, respectively.

Piccard had DOC concentrations which were generally lower than at Von Damm. The highest DOC was at South of Lung Snack (101.0 μM), and the lowest was at Hot Chimlet (41.3 μM). There are no strong indications that DOC concentrations increase with temperature at Piccard, as Beebe 4 (393 °C, DOC = 81.4 μM) and South of Lung Snack (57 °C) had the highest DOC concentrations with all other samples between 41.3 and 64.1 μM. At both Piccard and Von Damm, there were no strong indications that DOC increased or decreased conservatively with magnesium (Figure 4.4).

The isotopic composition of bulk DOC was determined by NOSAMS for background seawater (40.9 μM) and 3 sites at Von Damm (Table 4.6). At each site, DOC

concentrations were higher than background seawater. At the Northern Mound, White Castle had a bulk DOC concentration of 156.1 μM. DOC concentrations were highest at the Southern Mound, where Old Man Tree had 599.0 μM Ravelin 2 had 784.0 μM. $\delta^{13}C_{DOC}$ values increased with increasing DOC concentration, from -25.7 ‰ in deep seawater to -5.0 ‰ at Ravelin 2. The background seawater sample had a DOC Fm value of 0.55, corresponding to a radiocarbon age of 4,750 y (Table 4.6). At the Northern Mound, White Castle DOC had a Fm of 0.25. The Southern Mound, with samples from Old Man Tree and Ravelin 2, had the lowest $^{14}C$, with Fm values of 0.19 at both sites which is 0.06 lower than at White Castle.

Concentrations of formate correlated strongly with bulk DOC concentrations, indicating that bulk DOC concentration reflects the presence of formate (Figure 4.5).

*4.5 Gas-Chromatography Mass Spectrometry*

All samples, including the background seawater sample, contained benzoic acid, and benzene/phenol derivatives (Table 4.7). Peaks tentatively identified as sugars and amino acids were detectable at Von Damm only, and they tended to be lower in abundance. Palmitic and stearic fatty acids were found in most samples, though Von Damm had elevated levels of palmitate. In contrast, the Hot Piccard sample (Beebe 4) was the only one to include dodecanol, a 12-carbon alcohol.

GC-MS spectra of samples were abundant in low-intensity compound peaks which had a low (< 90 %) match with the NIST14 library, especially in lower-temperature samples. Hotter locations in contrast, tended to have higher abundances at

early retention times. All sample spectra excluding Beebe 4 had an uncharacterized hump which began at about 25 - 36 minutes (Figure A.2).

GC-MS confirmed the presence of carbitol only in the Beebe 4 sample, where it was by far the most abundant compound in the sample (RT = 5.08, Table 4.7). Butyl carbitol was also identified in the Hot Piccard sample (RT = 6.69 min). Polyethylene glycols, which appeared as a series of peaks between 5.04 and 22.14 min, were present in all samples including deep seawater.

*4.6 Dissolved Inorganic Carbon*

The DIC E.M. concentrations and isotopic signatures differed significantly from background seawater (2.25 mM, 1.6 ‰) at both Von Damm and Piccard (Figure 4.6). At Von Damm, the $\delta^{13}C_{DIC}$ increases as concentrations decrease, with the most extreme deviation at Ravelin 2 (1.5 mM, 5.2 ‰) (Table 4.3). Though geospatially and physiochemically similar, Ravelin 1 (2.1 mM, 3.3 ‰) differed substantially from Ravelin 2. Sites at the Northern Mound or at lower temperatures (T < 66 °C) had DIC signatures more similar to seawater than warmer sites on the Southern Mound.

In contrast, sites at Piccard tended to increase in E.M. DIC concentration and decrease in $\delta^{13}C$ with increasing temperature. Beebe 4 had the highest observed concentration of DIC (8.3 mM) and lowest $\delta^{13}C_{DIC}$ (-2.9 ‰) of all other sites.

**Table 4.1: Non-carbon physiochemical properties for individual samples from the Von Damm Vent Field.**

| Location | Sample ID | Max T (°C) | pH | Mg (mmol/kg) | Ca (mmol/kg) | $H_2S$ (mM) | $PO_4^+$ (μM) | $NO_3^-$ (μM) | $NO_2^-$ (μM) | $NH_4^+$ (μM) |
|---|---|---|---|---|---|---|---|---|---|---|
| Background Seawater | J-1244-Chem-7 | 4.0 | 7.73 | 51.4 | 9.6 | 0.06 | 0.24 | 8.41 | 0.00 | 4.95 |
| Arrow Loop | J-1243-Chem-4 | 137.3 | 6.08 | 25.2 | 10.7 | 1.27 | 0.30 | 0.40 | 0.00 | 13.42 |
| | J-1243-Chem-5 | 139.6 | 5.93 | 26.8 | 12.2 | 1.56 | 0.32 | 0.00 | 0.00 | 15.72 |
| | J-1243-Chem-6 | 139.2 | 5.98 | 26.6 | 11.4 | 1.47 | 0.25 | 1.07 | 0.00 | 15.67 |
| Bartizan | J-1244-Chem-1 | 137.1 | 5.96 | 28.1 | 11.5 | 1.63 | 0.36 | 0.19 | 0.00 | 15.84 |
| | J-1244-Chem-2 | 139.0 | 6.09 | 30.7 | 11.6 | 1.49 | 0.35 | 1.06 | 0.00 | 16.27 |
| Mustard Stand | J-1243-Chem-1 | 104.8 | 6.02 | 25.0 | 10.7 | 1.44 | 0.43 | 0.39 | 0.00 | 13.07 |
| | J-1243-Chem-2 | 100.3 | 6.13 | 31.3 | 12.2 | 1.65 | 0.18 | 2.19 | 0.00 | 14.94 |
| | J-1243-Chem-3 | 103.8 | 6.11 | 27.0 | 10.4 | 1.36 | 0.35 | 0.34 | 0.00 | 13.54 |
| Old Man Tree | J-1238-Chem-4 | 121.6 | 5.74 | 13.3 | - | 2.27 | 1.26 | 0.00 | 0.00 | 4.56 |
| | J-1238-Chem-5 | 121.6 | 5.74 | 24.6 | 11.7 | 2.35 | 1.01 | 0.00 | 0.00 | 6.32 |
| | J-1238-Chem-6 | 121.7 | 5.79 | 11.8 | 12.8 | 2.24 | 0.83 | 0.00 | 0.00 | 6.31 |
| | J-1238-Chem-7 | 121.7 | 5.74 | 14.2 | 13.9 | 2.46 | 1.03 | 0.00 | 0.00 | 5.02 |
| Ravelin 1 | J-1244-Chem-5 | 143.7 | 5.74 | 11.9 | 12.2 | 2.06 | 0.94 | 0.00 | 0.00 | 15.44 |
| | J-1244-Chem-6 | 143.8 | 5.68 | 17.8 | 15.2 | 2.26 | 1.19 | 0.00 | 0.00 | 15.10 |
| Ravelin 2 | J-1238-Chem-1 | 110.5 | 5.74 | 16.1 | - | 2.26 | 0.34 | 0.00 | 0.05 | 5.75 |
| | J-1238-Chem-2 | 105.6 | 5.79 | - | - | 2.19 | 1.22 | 0.04 | 0.09 | 3.29 |
| | J-1238-Chem-3 | 112.0 | 5.65 | 14.4 | 13.3 | 2.54 | 1.33 | 0.00 | 0.09 | 3.39 |
| Shrimp Hole | J-1244-Chem-3 | 20.9 | 7.35 | 48.3 | - | 0.26 | 0.27 | 4.08 | 0.00 | 12.76 |
| | J-1244-Chem-4 | 19.5 | 7.39 | 51.2 | 9.5 | 0.26 | 0.31 | 2.83 | 0.00 | 14.82 |
| White Castle | J-1235-Chem-1 | 163.5 | 5.75 | 15.5 | - | 1.28 | 0.51 | 0.76 | 0.00 | 4.29 |
| | J-1235-Chem-2 | 167.2 | 5.85 | 21.2 | - | 1.31 | 0.36 | 1.82 | 0.00 | 3.43 |
| | J-1235-Chem-3 | 170.4 | 5.56 | 13.1 | 13.9 | 1.73 | 0.82 | 0.00 | 0.00 | 3.32 |
| X-18 | J-1235-Chem-4 | 37.0 | 7.23 | 39.7 | - | 0.84 | 0.20 | 10.32 | 0.01 | 4.77 |
| | J-1235-Chem-5 | 33.0 | 7.17 | 12.9 | - | 0.80 | 0.68 | 10.03 | 0.01 | 4.58 |
| | J-1235-Chem-6 | 33.0 | 7.21 | 39.5 | - | 0.74 | 0.07 | 9.33 | 0.00 | 4.93 |
| | J-1235-Chem-7 | 65.8 | 7.00 | 33.0 | 10.7 | 1.62 | 0.98 | 5.86 | 0.16 | 22.73 |

* The presence of elevated ammonia and nitrate concentration lower than seawater (Morrison and Nowlin, 1982) suggest that the main collection line on the HOG may have not been sufficiently flushed of hydrothermal fluid prior to collecting the deep seawater sample.

**Table 4.2: Non-carbon physiochemical properties for individual samples from the Piccard Vent Field**. Values for deep seawater are presented in Table 4.1.

| Location | Sample ID | Max T (°C) | pH | Mg (mmol/kg) | Ca (mmol/kg) | $H_2S$ (mM) | $PO_4^+$ (μM) | $NO_3^-$ (μM) | $NO_2^-$ (μM) | $NH_4^+$ (μM) |
|---|---|---|---|---|---|---|---|---|---|---|
| Beebe 4 | J-1242-LV-17 | 393.0 | 4.7 | - | - | 3.49 | 0.13 | 3.58 | 0.00 | 23.86 |
| | J-1242-LV-23 | 393.0 | 4.9 | - | - | 3.33 | 0.12 | 3.98 | 0.00 | 19.69 |
| | J-1242-LV-24 | 393.0 | 4.7 | 21.7 | 5.9 | 4.22 | 0.16 | 3.72 | 0.00 | 23.02 |
| Hot Chimlet | J-1239-Chem-1 | 98.6 | 5.6 | 45.5 | | 0.42 | 0.17 | 1.89 | 0.00 | 12.66 |
| | J-1239-Chem-2 | 98.5 | 5.7 | 44.8 | 9.0 | 0.43 | 0.22 | 2.64 | 0.00 | 7.88 |
| | J-1239-Chem-3 | 98.3 | 5.6 | 44.5 | 8.7 | 0.43 | 0.16 | 1.93 | 0.00 | 14.75 |
| | J-1239-LV-23 | 96.4 | 6.7 | - | - | 0.03 | 0.09 | 13.59 | 0.02 | 5.98 |
| Lots of Shrimp | J-1241-Chem-1 | 35.1 | 6.1 | 21.7 | 5.9 | 0.08 | 0.13 | 13.62 | 0.08 | 5.95 |
| | J-1241-Chem-2 | 36.4 | 6.0 | 25.0 | 10.7 | 0.11 | 0.11 | 14.56 | 0.07 | 9.29 |
| | J-1241-Chem-3 | 35.5 | 6.1 | 31.3 | 12.2 | 0.08 | 0.14 | 13.82 | 0.09 | 8.71 |
| | J-1242-Chem-3 | 25.6 | 6.2 | 38.2 | 6.1 | 0.08 | 0.10 | 9.01 | 0.17 | 8.07 |
| | J-1242-Chem-4 | 25.2 | 6.2 | 50.3 | 8.6 | 0.09 | 0.12 | 8.87 | 0.17 | 7.64 |
| Shrimpocolypse | J-1240-Chem-1 | 93.1 | 5.6 | 35.4 | 5.4 | 1.00 | 0.19 | 2.67 | 0.00 | 13.13 |
| | J-1240-Chem-3 | 96.4 | 5.5 | 47.2 | 8.4 | 1.05 | - | - | - | - |
| | J-1242-Chem-5 | 93.6 | 5.5 | 45.9 | 7.5 | 1.18 | 0.10 | 2.36 | 0.00 | 12.99 |
| South Hot Chimlet | J-1241-Chem-4 | 38.6 | 6.3 | 25.2 | 10.7 | 0.12 | 0.12 | 16.32 | 0.00 | 7.93 |
| | J-1241-Chem-5 | 33.0 | 6.4 | 26.8 | 12.2 | 0.13 | 0.10 | 16.63 | 0.00 | 8.68 |
| | J-1241-Chem-6 | 35.3 | 6.3 | 26.6 | 11.4 | 0.10 | 0.11 | 16.65 | 0.00 | 9.32 |
| South Lung Snack | J-1242-Chem-1 | 53.8 | 5.5 | 36.6 | 7.6 | 1.19 | 0.11 | 5.79 | 0.00 | 9.64 |
| | J-1242-Chem-2 | 57.3 | 5.4 | 47.8 | 8.7 | 1.47 | 0.10 | 4.99 | 0.00 | 10.36 |

**Table 4.3: Measured and calculated endmember vent fluid compositions and isotope values at the Mid-Cayman Rise.**

| Vent | Sample | Max Temp. (°C) | Mg (mM) | pH | DIC (mM)* | $\delta^{13}C_{DIC}$ (‰)* | $HCOO^-$ (μM) | E.M. DIC (mM)** | E.M. $\delta^{13}C_{DIC}$ (‰)↓ |
|---|---|---|---|---|---|---|---|---|---|
| Deep Seawater | AT42-22-CTD3-B1 | 4 | - | - | 2.25 | 1.6 | - | - | - |
| | J2_1244_Chem7 | 4 | 52.5 | 7.73 | - | - | Bdl | - | - |
| | | | | | Von Damm | | | | |
| Arrow Loop | J2_1243_Chem4 | 137 | 25.2 | 6.08 | 1.98 | 3.6 | 136.4 | 1.72 | 6.0 |
| | J2_1243_Chem5 | 140 | 26.3 | 5.93 | - | - | - | - | - |
| | J2_1243_Chem6 | 139 | 26.6 | 5.98 | 1.99 | 3.6 | 207.0 | 1.72 | 6.3 |
| Bartizan | J2_1244_Chem1 | 137 | 28.1 | 5.96 | 2.27 | 2.8 | - | 2.28 | 4.1 |
| | J2_1244_Chem2 | 139 | 30.7 | 6.09 | 2.21 | 2.5 | 126.1 | 2.16 | 3.9 |
| Mustard Stand | J2_1243_Chem1 | 105 | 25.0 | 6.02 | 1.88 | 4.0 | 459.7 | 1.54 | 7.1 |
| | J2_1243_Chem2 | 100 | 31.3 | 6.13 | 1.91 | 3.7 | 419.6 | 1.41 | 8.5 |
| | J2_1243_Chem3 | 104 | 27.0 | 6.11 | 1.83 | 3.8 | - | 1.39 | 7.5 |
| Old Man Tree | J2_1238_Chem4 | 122 | 13.3 | 5.74 | 1.78 | 4.4 | - | 1.61 | 5.7 |
| | J2_1238_Chem5 | 122 | 24.6 | 5.74 | 1.73 | 4.3 | 628.8 | 1.27 | 8.6 |
| | J2_1238_Chem6 | 122 | 11.8 | 5.79 | 1.84 | 3.9 | - | 1.72 | 4.8 |
| | J2_1238_Chem7 | 122 | 14.2 | 5.74 | 1.72 | 4.5 | - | 1.52 | 6.1 |
| Ravelin 1 | J2_1244_Chem5 | 144 | 11.9 | 5.74 | 2.06 | 3.8 | 233.4 | 2.00 | 4.5 |
| | J2_1244_Chem6 | 144 | 17.8 | 5.68 | 2.14 | 2.8 | 246.0 | 2.09 | 3.5 |
| Ravelin 2 | J2_1238_Chem1 | 111 | 16.1 | 5.74 | 1.69 | 4.9 | 930.9 | 1.44 | 7.1 |
| | J2_1238_Chem2 | 106 | - | 5.79 | 1.50 | 5.2 | 874.4 | - | - |
| | J2_1238_Chem3 | 112 | 14.4 | 5.65 | 1.62 | 4.6 | - | 1.38 | 6.4 |
| Shrimp Hole | J2_1244_Chem3 | 21 | 48.3 | 7.35 | 2.26 | 2.2 | - | - | - |
| | J2_1244_Chem4 | 19 | 51.2 | 7.39 | - | - | Bdl | - | - |
| White Castle | J2_1235_Chem1 | 164 | 15.5 | 5.75 | 2.21 | 2.8 | - | 2.19 | 3.3 |
| | J2_1235_Chem2 | 167 | 21.1 | 5.85 | 2.23 | 2.5 | 117.0 | 2.21 | 3.0 |
| | J2_1235_Chem3 | 170 | 13.1 | 5.56 | 2.07 | 2.4 | 145.6 | 2.01 | 2.6 |
| X-18 | J2_1235_Chem4 | 37 | 39.7 | 7.23 | 2.35 | 2.5 | Bdl | 2.63 | 4.8 |
| | J2_1235_Chem5 | 33 | 12.9 | 7.17 | 2.18 | 2.6 | - | 2.16 | 2.9 |
| | J2_1235_Chem6 | 33 | 39.5 | 7.21 | 2.33 | 2.5 | Bdl | 2.54 | 5.0 |
| | J2_1235_Chem7 | 66 | 33.0 | 7.00 | 2.45 | 3.0 | - | 2.77 | 4.9 |
| | | | | | Piccard | | | | |
| Beebe 4 | J2_1242_LV17 | 393 | - | 4.74 | 8.31 | -2.8 | - | - | - |
| | J2_1242_LV23 | 393 | 24.7 | 4.92 | 6.77 | -2.9 | Bdl | 10.78 | -3.8 |
| | J2_1242_LV24 | 393 | 21.7 | 4.7 | 7.72 | -2.5 | Bdl | 11.55 | -3.1 |
| Hot Chimlet | J2_1239_Chem1 | 99 | 45.5 | 5.58 | 5.05 | -1.6 | Bdl | - | - |
| | J2_1239_Chem2 | 98 | 44.8 | 5.74 | 5.03 | -1.6 | Bdl | - | - |
| | J2_1239_Chem3 | 98 | 44.5 | 5.64 | 5.05 | -1.7 | Bdl | - | - |
| | J2_1239_LV23 | 96 | - | 6.65 | 2.59 | 0.8 | Bdl | - | - |
| Lots of Shrimp | J2_1241_Chem1 | 35 | 31.6 | 6.09 | 2.89 | 0.4 | Bdl | 3.85 | -0.6 |
| | J2_1241_Chem2 | 36 | 52.9 | 6.04 | 2.97 | 0.2 | Bdl | - | - |
| | J2_1241_Chem3 | 35 | 48.4 | 6.11 | 2.99 | 0.2 | - | - | - |
| | J2_1242_Chem3 | 26 | 38.2 | 6.17 | 2.84 | 0.5 | Bdl | 4.40 | -1.0 |
| | J2_1242_Chem4 | 25 | 50.3 | 6.18 | 2.84 | 0.5 | Bdl | - | - |

| | | | | | | | | | |
|---|---|---|---|---|---|---|---|---|---|
| Shrimp-ocalypse | J2_1240_Chem1 | 93 | 35.4 | 5.55 | 4.70 | -1.4 | Bdl | 9.76 | -2.8 |
| | J2_1240_Chem3 | 96 | - | 5.54 | 4.83 | -1.6 | Bdl | - | - |
| | J2_1242_Chem5 | 94 | 45.9 | 5.48 | 4.80 | -1.5 | Bdl | - | - |
| South of Hot Chimlet | J2_1241_Chem4 | 39 | 51.8 | 6.33 | 2.88 | 0.5 | Bdl | - | - |
| | J2_1241_Chem5 | 33 | 52.2 | 6.37 | 2.95 | 0.4 | - | - | - |
| | J2_1241_Chem6 | 35 | 50.6 | 6.33 | 2.86 | 0.4 | Bdl | - | - |
| South of Lung Snack | J2_1242_Chem1 | 54 | 36.6 | 5.50 | 4.33 | -1.1 | 26.1 | 9.10 | -2.6 |
| | J2_1242_Chem2 | 57 | 47.8 | 5.43 | 4.62 | -1.2 | 28.1 | - | - |

* DIC concentrations and isotopes were run in duplicates.
** Endmember calculations are increasingly unreliable as sample Mg concentration approaches that of deep seawater and are omitted for some samples.

**Table 4.4: Mean measured SPE-DOC concentration and isotopic values from the Mid-Cayman Rise.** Hyphens indicate that column analyses are not available for the sample.

| Vent Name | Sample ID | SPE Cartridge Count | Mean $[DOC]_{SPE}$ (μM) | stdev | $\delta^{13}C_{SPE}$ (‰) | stdev | Mg (mM) |
|---|---|---|---|---|---|---|---|
| Deep Seawater | J-1244-LV24 | 5 | 28.5 | 3.5 | -22.3 | 0.5 | - |
| | CTD-002-B11 | 5 | 26.9 | 3.6 | -22.2 | 0.6 | 52.3 |
| Bartizan | J-1244-LV23 | 5 | 9.8 | 2.5 | -22.6 | 0.4 | 21.8 |
| Mustard Stand | J-1243-LV15 | 5 | 8.0 | 1.4 | -23.1 | 1.2 | 23.4 |
| Old Man Tree | J-1243-LV23 | 5 | 4.8 | 1.1 | -22.8 | 0.2 | - |
| Ravelin 2 | J-1238-LV23 | 5 | 6.9 | 1.0 | -23.2 | 0.3 | 16.1 |
| Shrimp Hole | J-1244-LV15 | 5 | 26.1 | 3.3 | -22.3 | 0.5 | 48.9 |
| White Castle | J-1235-LV15 | 3 | 3.4 | 1.3 | -24.2 | 0.9 | 10.7 |
| X-18 | J-1235-LV17 | 4 | 18.1 | 0.6 | -23.0 | 0.2 | 41.9 |
| | J-1235-LV24 | 5 | 16.9 | 2.3 | -23.0 | 0.7 | 39.3 |
| Beebe 4 | J-1242-LV24 | 4 | 32.1 | 17.1 | -25.2 | 0.7 | 21.7 |
| Hot Chimlet | J-1239-LV15 | 5 | 20.1 | 3.5 | -22.4 | 0.3 | 45.2 |
| Lots of Shrimp | J-1241-LV15 | 5 | 28.4 | 8.6 | -22.3 | 0.3 | - |
| Shrimpocolypse | J-1240-LV15 | 5 | 25.7 | 5.7 | -22.4 | 0.4 | 46.2 |

**Table 4.5: University of South Carolina measured bulk DOC samples.**

| Field | Site Name | Sample ID | DOC (μM) | Formate (μM) | % Formate | Mg (mmol/kg) |
|---|---|---|---|---|---|---|
| Von Damm | Arrow Loop | J-1243-Chem-6 | 254.6 | 207.0 | 81.3 | 26.6 |
| | Bartizan | J-1244-Chem-1 | 183.3 | 126.1 | 68.8 | 28.1 |
| | Mustard Stand | J-1243-Chem-2 | 452.3 | 419.6 | 92.8 | 27.0 |
| | Old Man Tree | J-1238-Chem-7 | 645.7 | 630.0 | 97.6 | 13.4 |
| | Ravelin 1 | J-1244-Chem-6 | 292.8 | 246.0 | 84.0 | 17.8 |
| | Ravelin 2 | J-1238-Chem-3 | 957.5 | 902.7 | 94.3 | 14.5 |
| | Shrimp Hole | J-1244-Chem-4 | 53.6 | bdl | - | 49.6 |
| | White Castle | J-1235-Chem-3 | 177.6 | 145.6 | 82.0 | 12.1 |
| | X18 | J-1235-Chem-5 | 65.1 | bdl | - | 12.9 |
| | X18 | J-1235-Chem-7 | 48.6 | bdl | - | 33.1 |
| Piccard | Beebe 4 | J-1242-LV-24 | 81.4 | bdl | - | 21.7 |
| | Hot Chimlet | J-1239-Chem-2 | 41.3 | bdl | - | 45.3 |
| | Lots of Shrimp | J-1241-Chem-1 | 56.2 | bdl | - | 31.6 |
| | Lots of Shrimp | J-1242-Chem-3 | 63.8 | bdl | - | 38.2 |
| | Shrimpocalypse | J-1240-Chem-3 | 43.9 | bdl | - | 47.2 |
| | Shrimpocalypse | J-1242-Chem-5 | 64.1 | bdl | - | 45.9 |
| | South of Hot Chimlet | J-1241-Chem-5 | 52.1 | bdl | - | 52.2 |
| | South of Lung Snack | J-1242-Chem-2 | 101.0 | 28.1 | 27.9 | 53.2 |
| Deep Seawater | | AT42-22-CTD2-B11 | 44.0 | bdl | - | 53.2 |
| | | AT42-22-CTD5-B18 | 43.8 | - | - | 52.0 |
| | | J2-1244-C7 | 46.5 | bdl | - | 52.5 |

**Table 4.6: Measured DOC isotopic characteristics from the Von Damm vent field.**

| Vent Name | Sample ID | Max. T (°C) | Bulk DOC (μM) | $\delta^{13}C_{Bulk}$ (‰) | SPE-DOC (μM)* | $\delta^{13}C_{SPE\text{-}DOC}$ (‰)* | $\Delta^{14}C_{Bulk}$ (‰) | Fm C |
|---|---|---|---|---|---|---|---|---|
| Deep Seawater | AT42-22-CTD2-B11 | 4 | 41 | -25.7 | 27.7 | -22.2 | -451 | 0.55 |
| White Castle | J-1235-Chem3 | 170 | 156 | -10.8 | 3.3 | -24.2 | -754 | 0.25 |
| Ravelin 2 | J-1238-Chem3 | 112 | 784 | -5.0 | 6.9 | -23.2 | -807 | 0.19 |
| Old Man Tree | J-1238-Chem7 | 122 | 599 | -6.8 | 4.8 | -22.8 | -806 | 0.19 |

*From large-volume IRMS aliquots for that site.

**Table 4.7: Identified GC-MS compounds and abundances within samples from the Mid-Cayman Rise.** Samples were identified using a >85% match within the NIST14 chemical database. Samples are grouped using the same classification applied to combining the SPE extracts, and can be found in Table 5.1

| Group | Compound | NIST14 %Match | Retention Time (min) | Bknd SW Abundance* | Von Damm Abundance* | Piccard Abundance* |
|---|---|---|---|---|---|---|
| Alcohol | Glycerol | 92 | 6.05 | ++ | +++ | |
| Amine | Serine | 90 | 6.998 | | + | |
| Aromatic | Benzoic acid | 95 | 5.85 | ++ | ++ | +++ |
| Aromatic | Methyl 4-hydroxyphenylacetate | 94 | 9.41 | +++++ | +++++ | |
| Aromatic | 4-Hydroxybenzeneacetic acid | 99 | 10.941 | +++ | +++ | |
| Aromatic | Fenoxanil | 95 | 29.905 | | +++ | |
| Fatty acid | 1-Dodecanol | 90 | 9.71 | | | ++ |
| Fatty acid | Isopropyl palmitate | 98 | 17.528 | | ++ | |
| Fatty acid | Palmitic acid | 97 | 17.944 | ++ | + | + |
| Fatty acid | Stearic acid | 88 | 21.288 | | + | + |
| Ether | Carbitol | 95 | 5.08 | | | +++++ |
| Ether | Butyl carbitol | 90 | 6.699 | | | +++ |
| Ether | Tripropylene glycol mono-n-butyl ether | 80 | 9.327 | | | +++ |
| Glycol | Diethylene glycol | 85 | 5.75 | +++++ | +++ | +++++ |
| Glycol | Triethylene glycol | 87 | 8.828 | +++ | +++ | +++ |
| Glycol | Tetraethylene glycol | 94 | 13.087 | | ++++ | +++ |
| Glycol | Pentaethylene glycol | 90 | 17.711 | | +++ | ++ |
| Glycol | Hexaethylene glycol | 91 | 21.155 | | + | + |
| Glycol | Heptaethylene glycol | 89 | 22.136 | | +++ | + |

* Approximate abundances grouped by GC-MS area. +++++, > 20,000; ++++, 10,000-20,000; +++, 2,000-10,000, ++, 1,000-2,000; +, <1,000.

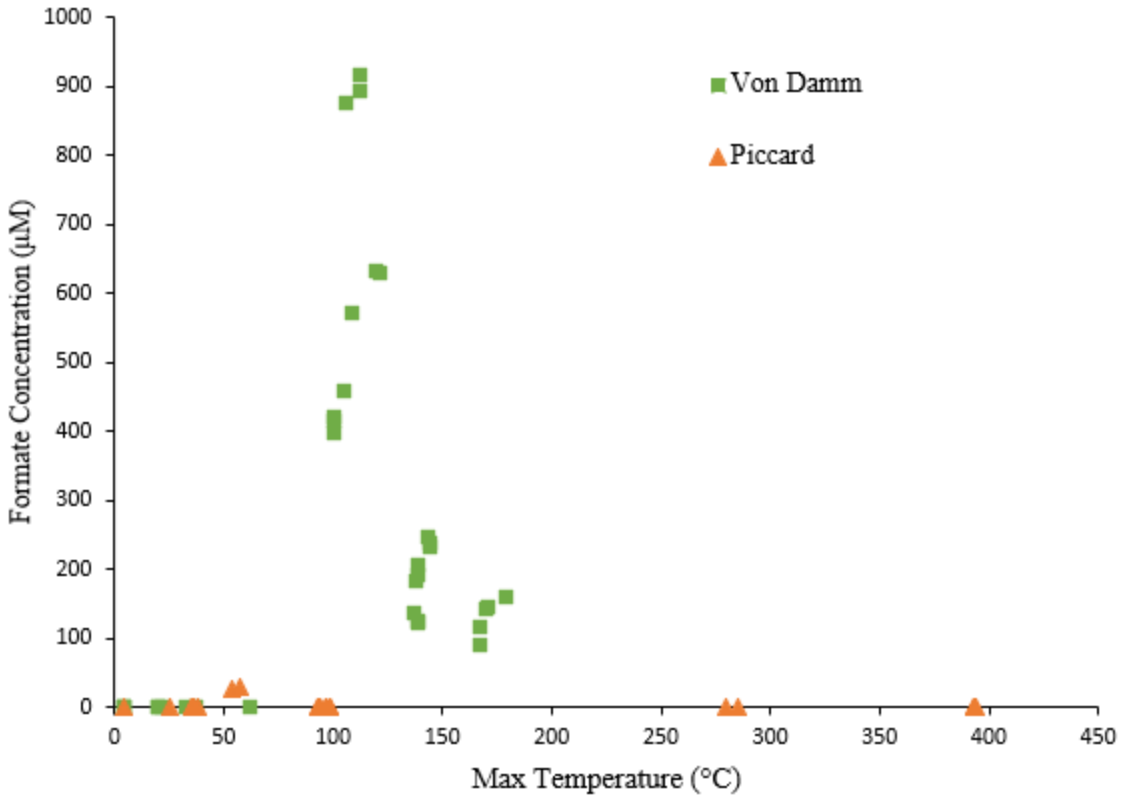


**Figure 4.1: Formate (µM) vs. maximum observed vent temperatures (°C).**

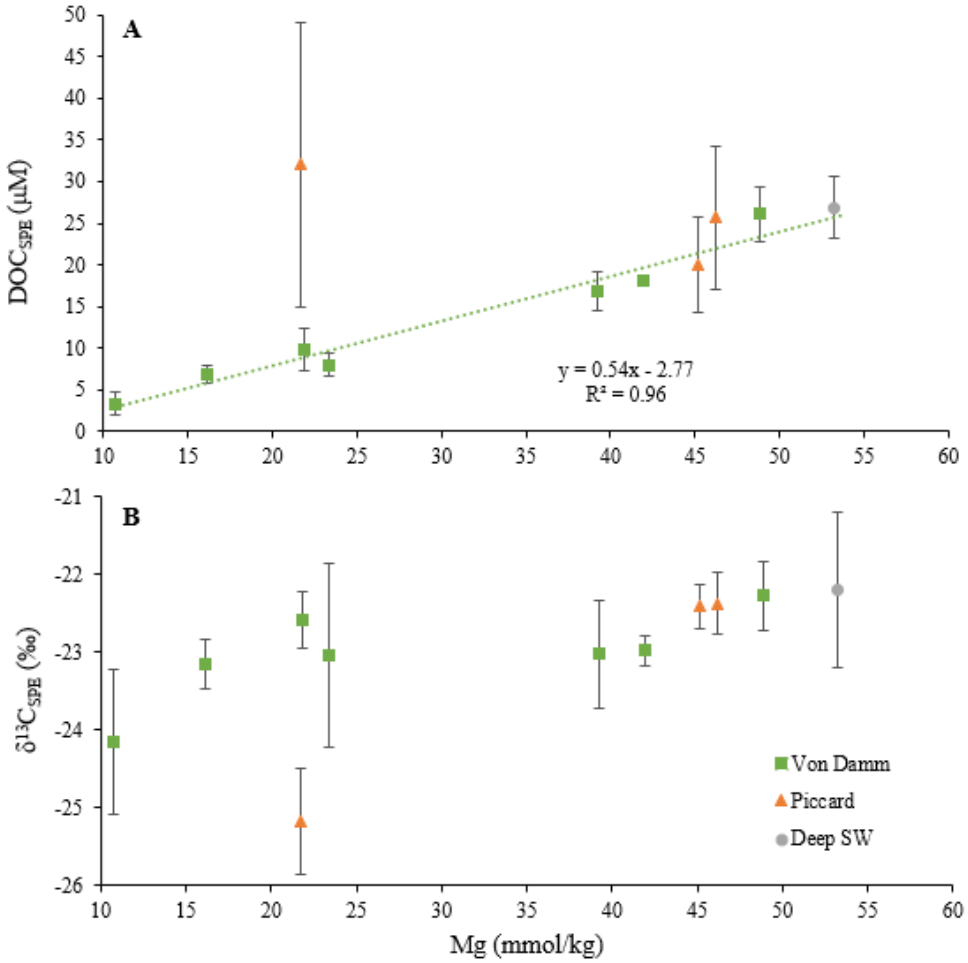


**Figure 4.2. Mean large-volume SPE-DOC concentration (A) and $\delta^{13}C$ (B) plotted against magnesium concentration for individual sites at Von Damm and Piccard.** Error bars are provided to indicate the standard deviation of multiple replicate cartridges of the same whole fluid sample (Table 4.4). Mg data is unavailable for Old Man Tree and Lots of Shrimp.

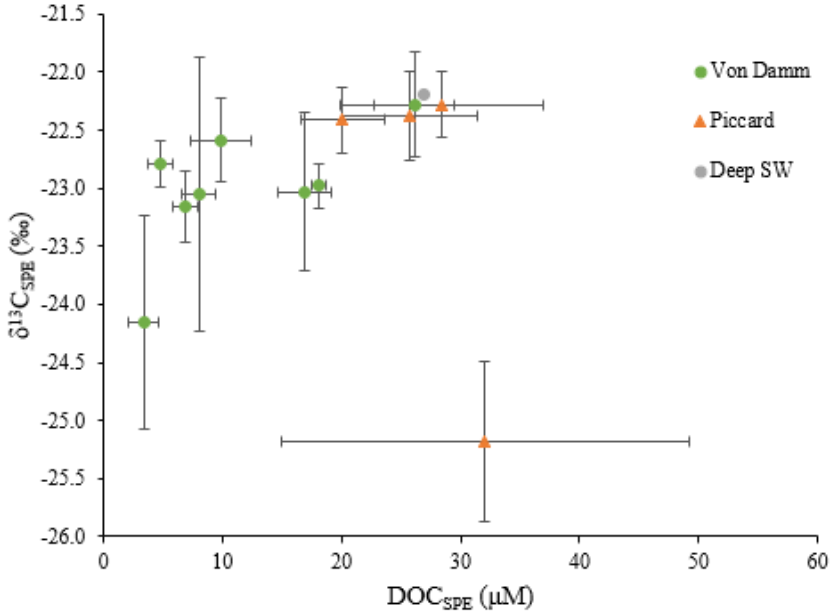


**Figure 4.3: SPE $\delta^{13}C$ vs. SPE- DOC concentrations for all large-volume samples acquired at the Mid-Cayman Rise.**

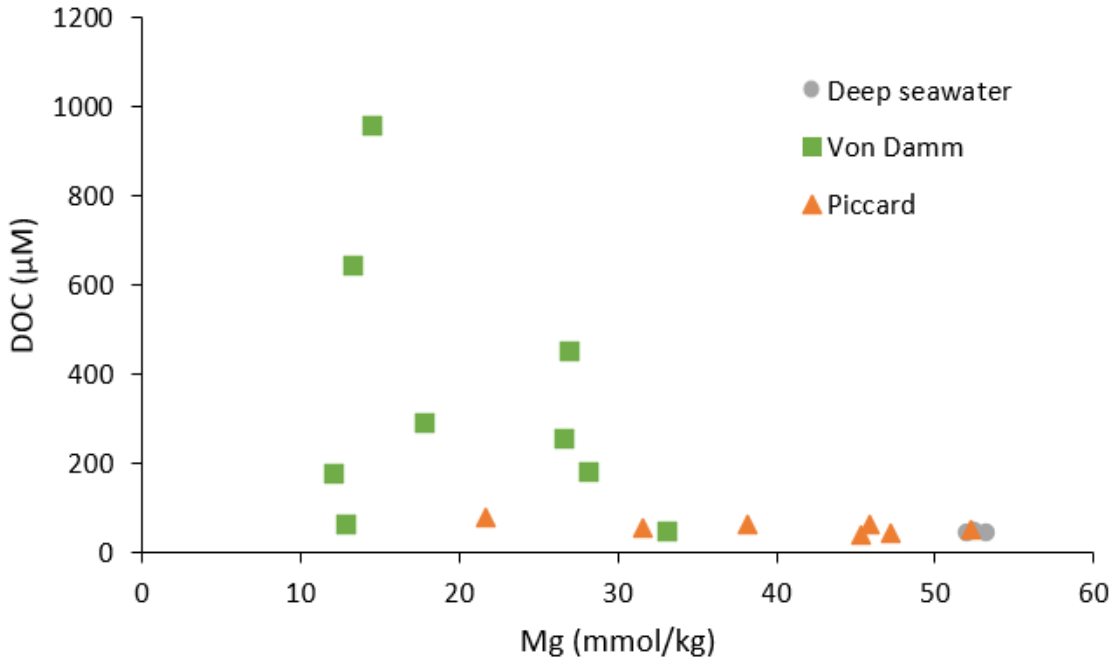


**Figure 4.4: Bulk DOC concentrations by high temperature combustion (µM) vs. magnesium (mmol/kg).**

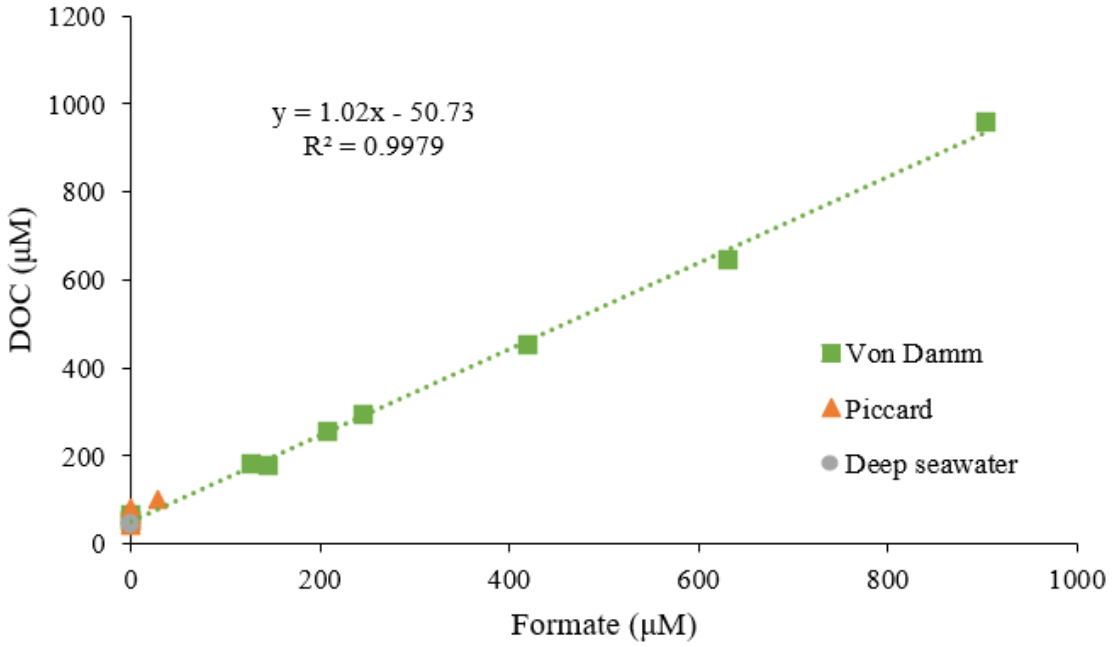


**Figure 4.5: DOC concentrations plotted against formate.** A linear trendline is constructed for Von Damm samples.

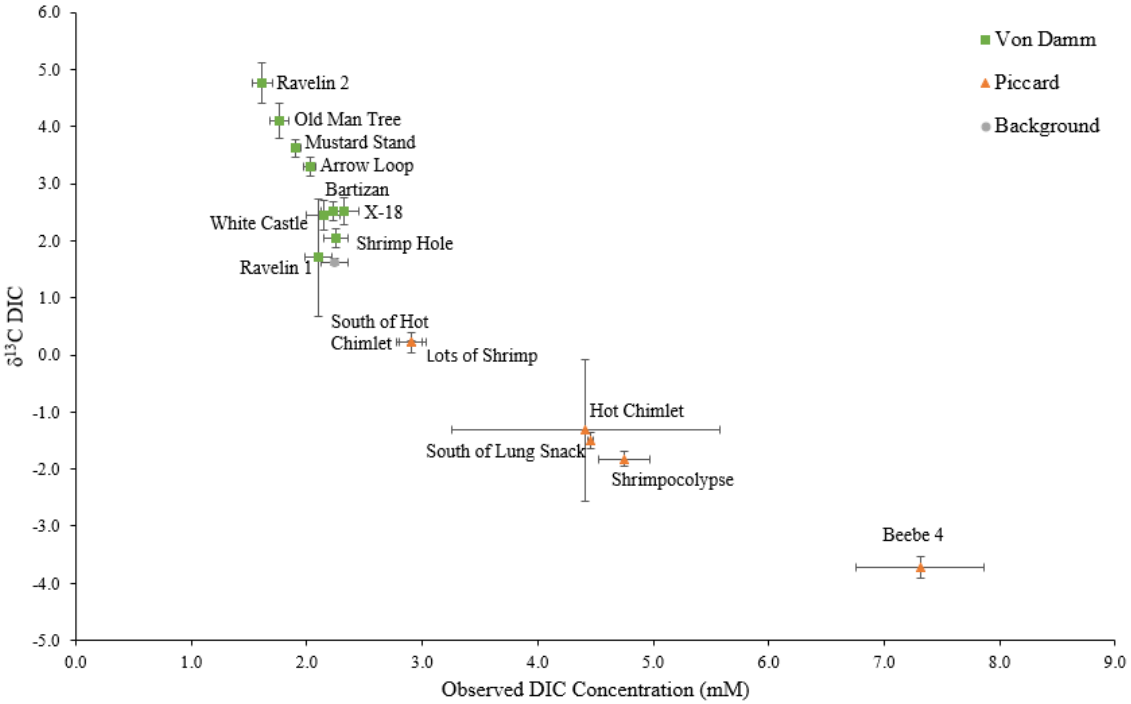


**Figure 4.6: Observed $\delta^{13}C_{DIC}$ plotted against DIC concentrations**.

# CHAPTER 5: DISCUSSION

## *5.1 DOC Concentrations and Isotopes*

Marine DOC, in contrast to DIC, is composed of hundreds of thousands of different compounds (Jiao et al., 2010; Hertkorn et al., 2013). Though there are many challenges in assessing such a mixture of compounds, DOC can be broadly characterized to discern lability, age, and dominant functional groups. Marine DOC of deep seawater has a concentration of 41 to 45 μM with a $\delta^{13}C$ of approximately -22 ‰ (Hansell, 2013). In this work, we further characterized DOC concentrations with the radioisotope, $^{14}C$, which has a radiocarbon Fm of 0.62 ($\Delta^{14}C$ = -390 ‰) in deep Atlantic seawater (Druffel et al., 2016).

The bulk DOC from the Von Damm Southern Mound had significantly higher concentrations than at sites on the Northern Mound (>400 vs. <250 μM, respectively) and correlated very strongly with increasing formate concentrations (Table 4.5; Figure 4.5). This geographical observation was consistent between DOC concentrations determined by high temperature combustion and by UV oxidation, though the latter concentrations were 7 – 22 % lower. Spatial differences are also indicated in the bulk $\delta^{13}C_{DOC}$, which was at least 4 ‰ more negative at the Northern Mound (White Castle, -10.8 ‰) than the Southern Mound (Ravelin 2 and Old Man Tree; -6.8 to -5.0 ‰). The Southern Mound DOC also had Fm values (0.19) that were 0.06 lower than that from the Northern Mound (0.25). Combined, these results suggest that increasing DOC concentrations are

accommodated by an increased ratio of $^{13}C_{DOC}$ and a lower Fm. Since formate contributes 82 – 94% of the DOC, these trends primarily reflect the different extent of formate synthesis at different locations.

These DOC concentrations and $\delta^{13}C$ values are very different from samples of mafic hydrothermal environments, such as the low temperature, ridge-flank Baby Bare seamount of the Juan de Fuca Ridge (64 °C, 11 μM, $\delta^{13}C$ = -34.5 ‰), despite comparable radiocarbon values (Fm = 0.17; McCarthy et al., 2010). Another low temperature system (<20 °C), North Pond within the Sargasso Sea, has been assessed for DOCs. Concentrations and $\delta^{13}C$ of DOC decrease from measured bottom water (41 μM, -23.3 ‰) to as low as 18 μM and -26.6 ‰, respectively (Walter et al., 2018). As a highly-sedimented system, this loss and fractionation of DOC is attributed to heterotrophic update by microorganisms. At Von Damm, sediment is not as extensive at North Pond and temperatures exceed 122 °C, the hypothesized upper-temperature for life (Takei et al., 2004; Yang et al., 2021). Radiocarbon values at North Pond (Fm = 0.38 ± 0.06) are also different than observed at Von Damm (0.21 ± 0.03), indicating decay through a relatively stagnant fluid and selective isotopic consumption during heterotrophy (Walter et al., 2018). At both the Juan de Fuca ridge and at North Pond, the loss of DOC was attributed to heterotrophic uptake by microorganisms.

The DOC concentrations at Von Damm are much higher than those of Baby Bare or North Pond due to the abiotic formation of formate discussed in section 5.3. This formate, which is much of the DOC within the Von Damm samples (Figure 4.5), results in organic matter with very different $^{13}C$ and $^{14}C$ values. The controls on the $^{13}C$ of the

DOC likely reflect the fractionation factor associated with the abiotic conversion of DIC to formate, as discussed in more detail below (section 5.5).

The causes for the $^{14}C$ values of DOC at Von Damm, however, are less clear. Entrainment of $^{14}C$-rich background seawater is expected at the Southern Mound (McDermott et al., 2015), though the Fm is highest at the Northern Mound. Since mantle carbon does not contain $^{14}C$ (Fm = 0), as a more endmember-like fluid presents a higher concentration of $^{14}C$. Formate in Lost City fluids varies in concentrations and radiocarbon abundances across the field, with higher concentrations associated with formate that contains more $^{14}C$ (Lang et al., 2018). This pattern is interpreted as requiring two sources of formate, one sourced from mantle carbon in the subseafloor and a second additional source added to fluids from more modern seawater DIC. This trend is opposite of the pattern observed at Von Damm, where higher concentrations of formate are associated with lower Fm values.

The data also highlights the complexity of these mixed/ultramafic systems in which the input of magmatic sources is unclear, fluid pathways are not entirely constrained, and few $^{14}C$ data are available. Further sampling may help identify how $^{14}C$-free carbon is preferentially introduced into the fluids feeding the Southern Mound.

*5.2 SPE-DOC Characterizations*

DOC isolated by solid-phase extraction represents refractory DOC, as smaller, hydrophilic compounds are not retained (Hawkes et al., 2016; Johnson et al., 2017). Of this SPE-DOC pool, there have been few observations taken from hydrothermal fluids and the influences on this reservoir remain poorly constrained. In deep seawater, SPE-

DOC has been measured to be around 35 μM with a $\delta^{13}C$ of -23 ‰ (Zigah et al., 2017), though SPE-DOC from hydrothermal systems can range from 15 – 539 μM, with lower concentrations generally associated with lower Mg values and purer endmember fluid (Hawkes et al., 2015).

The samples from Piccard did not have sufficient spread in Mg values to fully assess whether similarly pure hydrothermal fluids were correlated with lower SPE-DOC concentrations. The SPE-DOC concentrations of the lower-temperature PVF (25 – 99 °C) fluids ranged from 15.8 to 34.2 μM with $\delta^{13}C$ values of -22.0 to -23.0 ‰. While the concentrations differed from background seawater samples (27.7 ± 3.5 μM), the isotopic composition was similar (-22.2 ± 0.6 ‰; Figure 4.3). These low-temperature locations, however, did have high concentrations of Mg (45.2 to 48.9 mmol/kg) which were comparable to that of background seawater (52.3 mmol/kg; Table 4.2).

In contrast to the low-temperature PVF samples, Beebe 4 (393 °C) had SPE-DOC concentrations (32.1 ± 17.1 μM) significantly higher than other hydrothermal sites of comparable Mg concentrations (Figure 5.1) and isotopic compositions (-25.2 ± 0.7 ‰) are significantly more negative than deep seawater (-22.2 ± 0.6 ‰; Table 4.4).

In contrast, the SPE-DOC at Von Damm decreases in concentration and $\delta^{13}C_{SPE\text{-}DOC}$ values at more endmember-like conditions (Figure 4.2; Table 4.4). White Castle is the hottest location sampled (170 °C) and has SPE-DOC concentrations (3.4 ± 1.3 μM) that are 12% of deep Mid-Cayman Rise seawater (27.7 ± 3.5 μM) and $\delta^{13}C_{SPE\text{-}DOC}$ that is 2‰ lower (-24.2 ± 0.9 vs -22.2 ± 0.5 ‰). This loss of SPE-DOC extends to relatively low temperature vents such as X-18 (62 °C).

To investigate how the distribution of compounds that were lost, altered, added, or survived circulation through the hydrothermal system we carried out NMR analysis on the SPE extracts. To obtain sufficient carbon for resolvable NMR peaks (~5 mg C; Simpson et al., 2011), extracts from multiple similar locations were combined according to preliminary physiochemical and IRMS aliquot data (Table 5.1). The SPE blank had small peaks throughout the spectra that could be subtracted from the sample data in all regions with the exception of the $^{1}$H aromatics region between 6.5 to 8.5 ppm where they are substantially interfered (Figure 5.2). Data in the aromatics region is therefore not reported.

$^{1}$H NMR data indicate that with the exception of the Beebe 4 sample, the spectra resemble that of background seawater with an uncharacterized hump in the aliphatic to CRAM region (1 – 2.75 ppm) and peaks in the carbohydrate region at 3.25 and 3.7 ppm (Figure 5.3). Carbohydrate peaks were less pronounced in background seawater and the intermediate Von Damm sample (108 to 119 °C). Our $^{1}$H NMR is very similar to the spectra to that of SPE-DOC isolated in the Pacific Ocean (Lin et al., 2019), including a broad uncharacterized hump within the aliphatic region and a peak within the carbohydrates. The $^{1}$H NMR spectra of cooler Piccard samples (36 to 98 °C, Figure 5.3) are more similar to that of the Von Damm samples than that of background seawater, though it is unclear which compounds, bonds, or functional groups may be actively changing in these lower-temperature settings.

The $^{1}$H NMR of Beebe 4, or the hot PVF sample “L”, lacked the broad uncharacterized hump present in all other samples (Figure 5.3, Figure 5.4). Peaks were sharp and well defined with large peak areas, suggesting the presence of only a few

compounds rather than the thousands of structurally similar refractory compounds that typically contribute to seawater DOC (Hertkorn et al., 2006; 2013).

Further analysis of the Beebe 4 with 2D methods was used to potentially identify the compounds within the sample. $^{1}H$-$^{13}C$ HMBC NMR indicated that there were many carbon atoms close to oxygen, with distinct aliphatic and O-C bonded regions. This interpretation was reinforced by trends in $^{1}H$-$^{13}C$ HSQC NMR which indicated H-C bonds in similar associations with oxygen (Figure 5.5). $^{1}H$ DOSY made it possible to identify two different compounds, one with peaks at around 2 ppm of $^{1}H$ NMR were attributed to a compound different from other atoms, likely acetic acid or a carboxylated compound. $^{1}H$-$^{1}H$ COSY elucidated that there were few heterogeneous bonds in the sample, with O-C bonds from HMBC likely in a chain. Combined, the NMR indicated two different compounds. An ethoxylated compound "carbitol" (2-(2-ethoxyethoxy)ethanol), was the dominant compound in the sample, and smaller amounts of a carboxylated compound such as acetic acid. These compounds had a very close match to simulated $^{1}H$-$^{13}C$ HMBC NMR spectra (Figure 5.6).

*5.3 Organic Acid Concentrations*

Organic acids are very simple labile compounds that are therefore typically only present in low concentrations in the oceanic water column. As an important intermediate for biosynthesis, formate concentrations and isotopes become increasingly important in order to assess the lability of DOC and pathways for biosynthesis. Organic acids like formate can be formed from abiotic processes when $H_2$ concentrations are elevated (McCollom and Seewald, 2003a; Seewald et al, 2006; McDermott et al., 2020). Formate

concentrations have been measured at hydrothermal environments before, such as at Lost City (up to 144 μM; Lang et al., 2010), the Kidd Creek Mine (up to 1,000 μM; Sherwood Lollar et al., 2020), and the Mid-Cayman Rise (up to 669 μM; McDermott et al. 2015; 2020). To assess both the labile and refractory fractions of DOC, it is imperative to assess organic acids to begin to understand the labile portion. Considering only the one-carbon OA, formate, was observed there may be a special relationship between the labile DOC pool and inorganic carbon.

There are many proposed synthesis pathways for formate, with biotic and abiotic mechanisms proposed at different environments (McCollom and Seewald, 2003a; Lang et al., 2010; McDermott et al., 2015; 2020; Lollar et al., 2021). At the Mid-Cayman Rise, formate has been proposed to abiotically derive from seawater DIC (such as $CO_2$) which is reduced by high-$H_2$ endmember conditions (Equation 5.1; McDermott et al., 2015). At the Northern Mound, formate concentrations were as high as 352 μM (White Castle) in 2012. It is proposed that formate concentrations are even higher at the Southern Mound (up to 669 μM) due to increased entrainment of background seawater DIC during circulation, which also acts to lower temperature and increase pH.

$$CO_2 + H_2 \leftrightarrow HCOOH \leftrightarrow HCOO^- + H^+ \qquad (5.1)$$

Mantle $CO_2$, with a $\delta^{13}C$ of ~ -5 ‰, is not considered as a carbon source given vent $\delta^{13}C_{DIC}$ observations at Von Damm are substantially more positive with $\delta^{13}C$ values of at least +2 ‰ (Figure 4.6, Table 4.3). Rather, Von Damm vent fluid DIC concentrations are thought to be modified from background seawater (McDermott et al., 2018).

DIC-formate speciation, as a function of pH, suggests that formate should be the dominant compound at pH ranges of warm fluids of Von Damm (Figure 5.7). This is also true for the hottest, most endmember-like locations at Von Damm such as White Castle, where formate concentrations reach 117 μM (Table 4.3). Previous studies have noted higher formate concentrations at the Southern Mound, due in part to decreasing temperatures and increasing pH that accompany subseafloor entrainment of seawater DIC (McDermott et al., 2015). Formate concentrations were highest at the Southern Mound at sites such as Old Man Tree and Ravelin 2. In general, the temperature range of 100 – 122 °C at the Southern Mound had the highest concentrations of formate. Ravelin 1, which was venting at around 144 °C, had concentrations of 239 ± 9 μM and was significantly lower than that of Ravelin 2 in the immediate vicinity (902 ± 40 μM formate; T ~ 109 °C; Figure 5.8). Based on Mg concentrations, Ravelin 1 (14.9 ± 4 mM) was slightly more endmember-like than Ravelin 2 (15.3 ± 1 mM), which could suggest less background seawater had been entrained either at the point of sampling or in the subseafloor.

In contrast to Von Damm, formate was detected at only one location at Piccard, South of Lung Snack (27.1 ± 1 μM, 55 °C). Formate was absent at Hot Chimlet and Shrimpocalypse (Shrimp Gulley) where they were detected in samples from 2012 and 2013 (Figure 5.8; McDermott et al., 2020). 2020 Samples from Hot Chimlet (97 °C) were 51 °C cooler than in 2012 (148 °C), where the highest concentrations of formate were detected (54 to 167 μM; McDermott et al., 2020). This may relate to sampling, as the 2020 samples had Mg concentrations of 44.5 mmol/kg or higher which indicates at least 84% seawater. Hot Chimlet samples from 2012 also had Mg concentrations in this range, and showed formate concentrations decreasing as Mg increased. The lower temperature

when sampling may be conducive to microbial consumption of formate, which is not extensively detected in 2020. Given only one site at the PVF had detectable levels of formate in 2020, a correlation between formate and temperature cannot be drawn in the same way for samples from 2012 (McDermott et al., 2020).

*5.4 DIC Concentrations and Isotopes*

Dissolved inorganic carbon serves as a nearly ubiquitous reservoir of ocean carbon. Though dissolved organic carbon remains the focus of this study, it is dwarfed in size by the marine DIC pool. As the starting material of autotrophic and abiotic organic synthesis reactions, DIC concentrations and isotopes are key to deconvoluting reaction pathways. DIC consists only $CO_2$, $H_2CO_3$, $HCO_3^-$, and $CO_3^{2-}$ and has concentrations in deep Caribbean seawater of around 2.25 mM with a $\delta^{13}C$ of around 1.1 ‰ (Figure 5.9; Tschumi et al., 2011; McDermott et al., 2015). Literature values for DIC concentrations at hydrothermal vents are as high as 28 mM with $\delta^{13}C$ ranging from -11 to +10 ‰ (Figure 5.10).

An essential comparison of the DIC data collected at the Mid-Cayman Rise is to those of previous years. Concentrations and the carbon isotopic composition of DIC in 2012 range from 1.80 mM and 2.6 ‰ (Old Man Tree) to 2.79 mM and 0.8 ‰ (East Summit; McDermott et al., 2015). DIC concentrations from 2020 at White Castle, the hottest location at Von Damm also sampled in 2012, had lower concentration than those from 2012 (2.21 versus 2.51 mM), but are also a higher $\delta^{13}C_{DIC}$ value (2.8 versus 1.5 ‰). This difference in DIC concentration is not likely due to seawater entrainment, as the Mg concentrations were nearly identical in 2020 (13.5 mmol/kg) and 2012 (13.1 mmol/kg).

A potential explanation for the higher DIC concentrations in 2020 could therefore be due to lower formate concentrations. DIC and formate concentrations, when summed, remain stable across the Von Damm vent field at 2.3 ± 0.1 μM (Figure 5.11) and as formate concentrations increase, DIC concentrations decrease and $\delta^{13}C_{DIC}$ increase (Figure 5.12). This is consistent between both the Northern and Southern Mounds.

DIC concentrations for Piccard from 2012 and 2013 are available for high-temperature fluids. The Beebe 3 vent, adjacent to Beebe 4, has fluids with DIC concentrations as high as 26.3 mM (McDermott et al., 2018). Lower temperature vents, such as Hot Chimlet and Shrimp Gulley, have concentrations of 10.1 and 6.0 μM respectively (McDermott et al., 2020). These literature values at the Beebe vents are approximately 14.7 mM higher than our endmember values at Beebe 4 (10.8 to 11.6 mM) and almost twice those we observed at Hot Chimlet (5.6 to 6.7 mM). The DIC samples from 2012 and 2013 were collected using IGT samplers that prevent the loss of volatile species. Our HOG bag samples were unpressurized, potentially causing the degassing of DIC and $H_2S$ (which was also much lower) prior to analysis. This degassing particularly impacts the low pH sample (where DIC is preferentially present as volatile $CO_2$) with high concentrations (which causes supersaturation).

The lower DIC concentrations at Von Damm is similar to observed trends at other hydrothermal fields, though they may be for different reasons. The low-temperature ultramafic system, Lost City, has DIC concentrations far below those of Von Damm which is attributed primarily to carbonate precipitation (Kelley et al., 2005; Proskurowski et al., 2008). Von Damm DICs are distinguishable from hotter mixed systems in the Atlantic such as Menez Gwen ($\delta^{13}C$ = -9.1 to -6.8 ‰, 17 – 20 mM) and Ashadze ($\delta^{13}C$ =

0.2 to 2.1 ‰, 3.7 mM; Charlou et al., 2000; 2010). Von Damm's DIC concentrations are most comparable to those of the ulramafic/mixed vent fields Logatchev and Ashadze along the Mid-Atlantic Ridge (Figure 5.10). DIC $\delta^{13}C$ values at Logatchev are 4.1 to 9.5 ‰ which are more positive than deep seawater (~1.1 ‰; Tschumi et al., 2011; Charlou et al., 2010). The Ashadze (2.1 to 4.6 ‰) vent field also shows $\delta^{13}C$ DIC signatures more positive than those of background seawater. DICs from hydrothermal fields commonly have $\delta^{13}C$ DIC signatures that are more negative than background seawater. A similar process for abiotic synthesis of formate may be present at the Logatchev and Ashadze fields, though formate concentrations have not been reported and physiochemical conditions such as pH and temperature differ (Charlou et al., 2010).

Meanwhile, high-temperature systems such as the East Pacific Rise, Rainbow or TAG field have DIC concentrations exceeding 13 mM due to magmatic inputs (Von Damm et al., 1985; Lilley et al., 1993; Charlou et al., 2010). Piccard is situated atop thin crust and magmatic inputs are to be expected to increase the concentration of DIC with a mantle $CO_2$ signature of -9 to -4 ‰ (Bischoff and Disckson, 1975; Proskurowski et al., 2008), which nearly overlaps with the DIC endmember at Beebe 4 of -3.8 ‰. This range is commonly observed in mafic environments (Figure 5.10).

The DIC isotopic signatures for background seawater are more positive than those reported in the literature. Sample AT42-22-CTD3-B1 had a DIC concentration of 2.3 mM and a $\delta^{13}C$ of 1.6 ‰ whereas J-1244-C7 had a concentration of 2.2 mM and $\delta^{13}C$ of 1.6 ‰. Since sample J-1244-C7 is thought to have been cross-contaminated or entrained a small amount of hydrothermal fluid (Section 4.1) we do not consider this value further. These observations of background $\delta^{13}C_{DIC}$ are higher by 0.5 ‰ than those measured in

2012 (1.1 ‰; McDermott et al. 2015), though this is within the analytical error of the measurements.

*5.5 Isotopic Fractionation of Formate Synthesis*

If the formate at Von Damm is exclusively synthesized from DIC and there are no other major gains or losses of either species, then their isotopic compositions can be used to define a fractionation factor of the formate synthesis reaction. While formate fractionation factors have been determined for biosynthetic reactions (Penning and Conrad, 2006), it has not yet been determined for abiotic synthesis reactions. Given the temperatures of the Von Damm fluids, formate synthesis has been interpreted as being exclusively abiotically synthesized (McDermott et al., 2015). Therefore, this suite of samples could provide clear constraints on abiotic synthesis fractionation factors that could be used to interpret isotopic signatures of formate in other locales. To assess this fractionation, we approach using a closed system equilibrium model.

Prior to modeling, it is important to constrain which samples are indicative of abiotic formate synthesis at Von Damm. From the endmember DIC $\delta^{13}C$ and concentrations, the site X-18 does not follow the general trends from other sites in the field (Figure 5.13). Values at X-18 have a higher $\delta^{13}C$ (4.8 to 5.0 ‰) than seawater, but also have higher DIC concentrations (2.5 to 2.8 mM) whereas other sites suggest they should fall below the background seawater DIC of 2.25 mM. Shrimp Hole had magnesium values exceeding 48.3 mM which indicate >92 % seawater (Table 4.3) and are therefore unreliable for endmember calculations.

In equilibrium fractionation, we assume a closed system where DIC and formate are free to equilibrate with each other. Initially, only DIC is present as a starting material and no formate is present. Over time, some of this DIC is converted to formate, but the total amount of carbon in the system remains the same (Figure 5.11). Thus, the concentration of DIC at time t ($C_t$) is equal to the amount that was initially present in the starting fluid ($C_o$) minus the amount lost to the sole product, formate ($C_p$).

$$C_t = C_o - C_p \qquad (5.2)$$

To account for the $^{13}C$ as a mass balance, the equation can be transformed by multiplying through by the $^{13}C/^{12}C$ ratio (R) of each constituent. To convert from $\delta^{13}C$ values to R values, see Eq. 5.9.

$$C_t R_t = C_o R_o - C_p R_p \qquad (5.3)$$

This equation can be rewritten to solve for the only unknown, $R_p$:

$$\frac{C_t R_t + C_o R_o}{C_p} = R_p \qquad (5.4)$$

The fractionation factor, α, is defined as the $^{13}C/^{12}C$ of the product over the reactant. In this case, $\alpha$ is representing the fractionation between formate and DIC, where DIC is the reactant.

$$\alpha_{DIC-formate} = \frac{R_p}{R_t} \qquad (5.5)$$

However, this equation presents two unknowns. $R_p$, and $\alpha$. $R_p$ is unavailable as $\delta^{13}C_{formate}$ has not been measured. We can define the fraction of remaining DIC.

$$f = \frac{C_t}{C_t + C_p} \qquad (5.6)$$

Substituting this $f$ value into Eq. 5.2:

$$C_f = C_o - (1 - f)C_o \qquad (5.7)$$

Similarly, $C_f$ can be substituted into Eq. 5.4 to express α as a function of *f*:

$$\alpha = \frac{R_f C_f - R_0 C_0}{C_f - C_0} \qquad (5.8)$$

Since α and $R_f$ remain unknown, α can be deterministically constrained such that modeled values of $R_f$ align with measured endmembers of DIC ($R_t$). By adjusting the value of α to match observed DIC concentrations and isotopic ratios, α was determined to be approximately 0.990. This approach assumes that the isotopic fractionation of DIC to formate is constant throughout the reaction process, despite changing in situ conditions that may impact it, such as temperature.

This can be translated into $\delta^{13}C$ (‰) notation using the equation:

$$\varepsilon = (\alpha - 1) * 1000 \qquad (5.9)$$

and ε can be deduced to be approximately -10 ‰ (Figure 5.14a). However, this value of ε does not clearly capture the DOC endmember $\delta^{13}C$, of which the majority is expected to be formate (Figure 4.5). Further adjustment of α to fit the DOC isotopes results in an ε of -14.5 ‰ (Figure 5.14b).

These fractionation factors (-14.5 to -10 ‰) can be compared to those determined experimentally for biological synthesis reactions, and those that have been previously observed in other environmental settings. Aqueous formate fractionation has been observed in other applications (Table 5.2), though the fractionation factors found here are not a perfect match with any particular study. Penning and Conrad (2006) analyzed the fractionation factor between $CO_2$ and formate, deducing an ε between $CO_2$ and formate of approximately -14.5 ‰. This value for ε was deduced from isotopic equilibrium in a chemostat headspace, where the $\delta^{13}C_{CO2}$ and $\delta^{13}C_{formate}$ settled at approximately -7 ‰ and -21.5 ‰, respectively. This value of ε, while comparable to the lower extreme of our

equilibrium model, is taken from a biological setting where 10 mM of glucose is decomposed in cultures of *C. papyrosolvens* at a pH of 7.2, which is not directly comparable to the organic, pH, or microbial conditions at Von Damm.

Lang et al. (2018) observed formate $\delta^{13}C$ values at Lost City Hydrothermal Field that increased with increasing concentrations, though the fractionation factor ranged from -7.1 to -1.8 ‰ assuming mantle $CO_2$ was the starting material. Our equilibrium fractionation factors differ by at least 2.9 ‰ from this range. Lost City has other processes influencing DIC concentrations and isotopes, such as carbonate precipitation and biological mechanisms which may differ from Von Damm's (Kelley et al., 2005; Proskurowski et al., 2008).

Another study looked at formate and DICs from a billion year-old aquifer of the Canadian Shield: The Kidd Creek Mine boreholes (Sherwood Lollar et al., 2020). They identified $\delta^{13}C_{DIC}$ of -8.8 to -0.5 ‰, and $\delta^{13}C_{formate}$ of -17.7 to -9.7 ‰, resulting in ε values between -17.2 and +0.9 ‰. This range of ε envelops ours from Von Damm (-14.5 to -10 ‰) and shows formate being depleted relative to source DIC, though the sample environments are not directly comparable. The Kidd Creek Mine is located within the Canadian shield, with highly variable mineralogies ranging from felsic to highly metamorphosed ultramafics (Sherwood Lollar et al., 2020). Borehole temperatures were all below 27 °C at a pH of ~6.2 and analogous sample such as X-18 or Shrimp Hole from Von Damm did not have detectable concentrations of formate (Table 4.3).

These factors being considered, the fractionation factors from equilibrium fractionation have some overlap with values reported in literature. However, the environments themselves are not entirely comparable and may not accurately represent

the processes at work. Though our range of ε (-14.5 to -10 ‰) is comparable to that of biological fractionation (-14.5; Penning and Conrad, 2006), locations at Von Damm with the most formate are pushing the threshold of the upper temperature of life (100 to 170 °C; Takei et al., 2004; Yang et al., 2021). Similarly, the mineralogies of the Kidd Creek boreholes are much more felsic, perhaps allowing for formate at geochemical conditions which is not detected at similar conditions of Von Damm. However, these ε data help define the abiotic synthesis of formate at Von Damm where there are relatively few field data which assess such a process. Discerning the fractionation factor is particularly important as formate comprises the majority of DOC at Von Damm. If DOC is being abiotically added from DIC in extensive quantities, it is an essential geochemical control on other processes which also utilize carbon from those pools and may be an important mechanism for other systems with mixed host-rocks.

### *5.6 Is Refractory DOC Removed at Von Damm and Piccard?*

Our main hypothesis was that the refractory DOC carried with deep seawater is removed during hydrothermal circulation at the Von Damm and Piccard vent fields. At mafic locations such as Baby Bare, the Main Endeavour Field, and North Pond, the loss of seawater DOC can be clearly observed by bulk concentrations that are lower than seawater (Lang et al., 2006; Walter et al., 2018; Lin et al., 2019). At the Von Damm field, extremely high concentrations of formate lead to high DOC concentrations, and may mask removal of seawater DOC.

Therefore, to address if dissolved organic carbon is sequestered at the mixed host-rock Von Damm site, the non-formate refractory reservoir must be assessed. The SPE-

DOC results at Von Damm are inversely proportional with Mg, indicating that this portion of the DOC pool is lost during circulation (Figure 4.2). In comparison to background seawater (average SPE-DOC: 27.7 ± 3.5 μM), White Castle has lost nearly 90% of its SPE-DOC (3.4 ± 1.3 μM; Table 4.4). A similar loss of SPE-DOC has been previously observed at hydrothermal environments, with lower concentrations in fluids with lower Mg concentrations at many different vent fields (Hawkes et al., 2015). At Von Damm, this loss of SPE-DOC occurred in conjunction with a preferential removal of $^{13}C$ constituents (Figure 4.3). The preferential removal of $^{13}C$-containing molecules has been observed previously at the Juan de Fuca ridge flank, though the exact mechanism causing this feature remains unknown (Lin et al., 2019).

The removal of SPE-DOC can be further characterized by $^{1}H$ NMR and GC-MS, which indicate that some background heterogeneity is lost during alteration. Results of NMR analysis indicate that deep seawater exhibits a broad hump through the aliphatic and carbohydrate sections of the spectra, representing hundreds of thousands of individual compounds (Hertkorn et al., 2013). At Von Damm, spectra are similar to that of background seawater but also exhibit sharp peaks which are not present in deep seawater (Figure 5.3). The $^{1}H$ NMR spectra of the more diffuse and cooler locations of Von Damm are similar to background seawater, likely reflecting the substantial amounts of seawater that are entrained in these locations.

While a similar loss of refractory organic matter was expected at the Piccard vent field, a clear relationship between lower Mg samples and lower SPE-DOC concentrations was not able to be documented, in large part because of the characteristics of the sampled locations. Two of the three SPE-DOC concentrations of the low temperature Piccard

samples are similar to deep seawater, and only one is slightly lower. All three low-temperature PVF samples have isotopic compositions similar to seawater. The Beebe sample has SPE-DOC concentrations higher than deep seawater but an NMR spectra that lacks many of the characteristic features of refractory DOC. At this time it is unclear whether refractory organic matter is removed during circulation through the Piccard field.

At Von Damm, there is a removal of refractory DOC indicated by concentrations of SPE-DOC (Figure 4.2a) and could be attributed to several potential mechanisms: heterotrophy by microbes, thermal breakdown to $CO_2$ or $CH_4$ under high temperature regimes, or sorbing to mineral surfaces.

Refractory DOC may be taken up by organisms during hydrothermal recharge, though isotopic fractionation would suggest enrichment rather than depletion of $^{13}C$ and distinct radiocarbon values (McCarthy et al., 2010; Walter et al., 2018). The maximum reported temperature at Von Damm (> 226 °C) far exceeds the threshold for life (~122 °C), so chemoautorophy of DOC would be unlikely within endmember fluids (Takei et al., 2004). Though calcareous sediments have been reported around Von Damm (Hodgkinson et al., 2015), venting locations at the North and South Mounds are defined by talc chimneys and igneous outcrops with sediments not comparable to other hydrothermal locations in the literature (Simoneit et al., 1993; Lin et al., 2017; Walter et al., 2018; Lin et al., 2019). At cooler locations around Von Damm, such as Mustard Stand (~105 °C), measured fluid DOC is lower than background seawater but shares many geochemical similarities in DICs and formate to hotter locations such as Ravelin 1 (~144 °C) and White Castle (~175 °C). At another hydrothermal field, Lost City is comparable to Von Damm with ultramafic and gabbroic basement rock and more

moderate temperatures (<100 °C) but it is unclear what role heterotrophy plays in that system (Lang et al. 2006).

Another sink could come from volatilization via pyrolysis or cracking reactions, which could begin at 150 °C (Simoneit et al., 1992). This would preferentially break up refractory components into smaller compounds that may not have been retained on or eluted from our PPL SPE cartridges (McCollom et al., 1999b; Seewald, 2003; Hawkes et al, 2015). At the ultramafic Rainbow and Lost City fields, many aliphatic, aromatic, and carboxylated compounds were identified within the fluids (Konn et al., 2009). However, neither low-carbon number alkanes nor PAHs were detected in high abundance or quality in sample GC-MS spectra of SPE extracts from the Mid-Cayman Rise. Other studies, however, utilized HLB cartridges with three different elution agents: hexane, methanol, and dichloromethane. This series of elutions may account for the lack of nonpolar compounds which are presented in literature (Konn et al., 2009). This may have been increasingly pronounced at Piccard, as high-temperature pyrolysis could preferentially contribute to methane or DIC pools which are elevated relative to background seawater (McDermott et al. 2015; 2018).

The removal of refractory organic matter could also be due to sorption of organic molecules onto mineral surfaces. The role of sorption onto clay surfaces is not insignificant and montmorillonite clays have been found to have an affinity for sorbing hydrophilic compounds (Conte et al. 2011). Montmorillonite, a smectite clay formed from high temperature (>160 °C) alteration of mafic igneous rock, would be expected at Von Damm along with chlorite (220-350 °C) at the Von Damm vent field (Fulignati, 2020). Clay formation could happen as early as 150 °C and smectite and chlorite clays

have been found in olivine gabbros along the Mid-Cayman Rise (Ito and Anderson, 1983). Studies have shown that both clays have a high potential to sorb DOC, with smectite sorbing up to 25.33 mg of DOC per gram of clay and chlorite having a high partition coefficient for common phytoplankton DOM (Saidy et al., 2013).

*5.7 Addition of Labile DOC at Von Damm and Piccard*

Our second hypothesis stated that hydrothermal environments can produce chemically-distinct labile DOC depending on the host rock, temperature, and fluid composition. Though Von Damm fluids have lost refractory seawater DOC, they also contain high concentrations of labile DOC in the form of formate. Compared to previous work at Cayman, formate is present at similar concentrations with the exception of the Northern Mound and Ravelin 2 of the Southern Mound (Figure 5.8; McDermott et al., 2015; McDermott et al., 2020). Concentrations of formate were lower than previously seen at White Castle (131 ± 20 μM versus 352 μM) and Arrow Loop (172 ± 50 μM versus 274 μM) which had comparable values for Mg at White Castle (13.1 mmol/kg versus 13.5 mmol/kg in 2012).

There are many reasons formate concentrations may be lower between 2012 and 2020, such as changes in entrainment of deep seawater. Ultramafic components of a mixed system, such as peridotites or gabbros of the Von Damm vent field continue to change over time as serpentinization drives the alteration of fluid pathways with cracking and exposure to fresh rock over time (MacDonald and Fyfe, 1985; Palandri and Reed, 2004; Iyer et al., 2008). Ravelin 2 on the other hand, was nearly double the formate concentration in 2020 (902 ± 40 μM) that was observed in 2012 (474 μM) and had the

highest concentration of any measured vent. Again, Mg values were very comparable between years so sample quality is unlikely to account for these differences. In 2012, hydrothermal fluid samples were collected exclusively using IGTs, whereas in 2020 the HOG and IGTs were both deployed to collect samples. Samples analyzed from the site Old Man Tree on the Southern Mound was sampled by both the HOG sampler (632 μM) and IGTs (634 μM), with concentrations within 1.9 μM of each other. This suggests that changes in formate concentrations are not attributable to sampling techniques, and data are valid for comparison with IGTs from a method standpoint. Sample processing differed, as values of formate were analyzed in 2012 by ion chromatography whereas 2020 values were discerned from high-performance liquid chromatography.

One interesting comparison is that of Ravelin 1 (144 °C) and Ravelin 2 (109 °C), which have differences in DIC and formate which have been discussed in sections 5.3 and 5.4. These sites may differ so drastically because of the elevated temperatures at Ravelin 1, which make it more comparable to the hot endmember-like fluids of the Northern Mound. This may suggest that whatever formate formation pathway could have a relationship with temperature, as sample temperatures >137 °C have shown significantly lower formate perhaps due to less entrainment of 4°C seawater (Figure 4.1).

From a physiochemical standpoint, formate is the dominant species at Von Damm for a pH exceeding 5.5 at temperatures of around 110 °C (Figure 5.7). The synthesis of formate is likely deriving from an abiotic source, as few living organisms would be detectable above the upper limit of life (Takei et al., 2004; McDermott et al., 2020). Instead, this synthesis is likely due to the entrainment of background seawater DIC which is then mixed with endmember fluids characterized by high $H_2$ concentrations and

temperatures (McDermott et al., 2015; 2020). At lower temperatures (<122 °C), biological processes may begin to play a role in regulating the abundance of labile DOC and DIC.

*5.8 Dominant Component of Piccard SPE-DOC*

At Beebe 4, however, NMR spectra of SPE-DOC were strikingly different from all other locations on the MCR. The concentrations of SPE-DOC are somewhat higher at Beebe 4 than background seawater (32.1 ± 17.1 vs 27.7 ± 3.6 uM), though its isotopic composition was substantially lower (-25.2 ± 0.7 vs -22.2 ± 0.5 ‰). The highest individual SPE-DOC concentration at Beebe 4 was measured to be at 65.8 μM and accounted for most of the variability in the sample mean. However, this value is encompassed by the bulk DOC from Beebe 4 (81.4 μM). Work is still underway to assess IRMS SPE-DOC concentrations relative to a more conventional TOC method, though preliminary data still indicate that Beebe 4 SPE-DOC is much higher than expected (Figure A.3).

Elevated SPE-DOC concentrations at the Beebe vents were also observed in 2012 samples collected using mini-Niskin (23 μM) and gas tight (~31 μM) fluid samplers. Notably, the Beebe locations were anomalously high for all other vent fields (Figure 5.1). There is no evidence of further analysis on the 2012 SPE-DOC samples in literature, prompting further analysis to try and characterize the anomalously high carbon from Beebe.

Using $^{1}H$ and 2D NMR methods paired with GC-MS, the organic content of these fluids was determined to be dominated by only a few simple compounds (Table 4.7,

Figure 5.5, Figure 5.6). The presence of carbitol could be confirmed by both the GC-MS analysis and by modeling an idealized carbitol molecule by 2-D NMR, which matched the measured pattern of the Beebe sample.

Carbitol is constructed of multiple low-energy C-O bonds which are significantly less stable at high temperatures than benzene rings or additional π bonds between carbons but are comparable to a C-C σ bond.

A potential source of carbitol would be from ship or sampling equipment contamination. The high temperatures of the Beebe vents make it unlikely that carbitol would be stable. Carbitol was identified in SPE GC-MS spectra with a series of polyethylene glycols, which are common solvents used in cleaners and soaps. However, carbitol was only detected in the samples from Beebe 4 from a single dive and was the dominant signal by far (Figure 5.16). Contamination may come from sampling apparatus such as the HOG or IGTs. Similarly, contamination may also derive from vessel or ROV specific soaps, oils, or cleaners as the 2020 expedition used the *R/V* Atlantis and *ROV JASON*. Given the similarity in concentration of SPE-DOC from 2020 and 2013 (reported in Hawkes et al. 2015), it is unclear whether contamination is consistent with findings from the 2013 expedition, which used *ROV Nereus* aboard *R/V Falkor*. Preliminary University of South Carolina GC-MS analysis of some vessel oils and cleaners used on JASON and have not detected carbitol.

Carbitol and other ethoxylated compounds have been reported in natural settings and laboratory experiments. Laboratory simulations at have synthesized glycerols and carbitol-like compounds from long-chain alkanes at temperatures of 150 to 250 °C (Rushdi and Simoneit, 2006). Esters were shown to form under high temperatures and are

proposed to be stable at temperatures exceeding 300 °C (Rushdi and Simoneit, 2006; Simoneit et al., 2007; Shock et al., 2013). In a natural setting, carbitol was identified from the Sutter's Mill meteorite, a carbonaceous chondrite rich in organic matter. Samples were extracted from the meteorite by subjecting a powdered subsample to a week of aqueous conditions 300 °C, 100 MPa, and characterized carbon via EA-IRMS and NMR (Pizarrello et al. 2013). The GC-MS fragmentation spectra confirmed that the compound in the Beebe 4 sample was carbitol with a 99% match to the NIST14 database (Figure 5.15). This was confirmed by passing small volumnes (10, 25, and 50 μL) a carbitol standard (150 ng/μL) over an SPE column and observing carbitol in resultant GC-MS. With low concentrations of carbon, there may be limitations on NMR as $^{13}C$ – essential for 2D analyses – may become less reliable (Simpson et al., 2011).

These thoughts being considered, there is still work underway to test for potential contaminants. Carbitol and ethoxylated compounds, though synthesized in some lab settings (Simoneit et al., 2007), are also associated with oils and cleaners. Lab analyses using GC-MS are currently being performed to search for carbitol in materials commonly associated with sampling, including materials from the R/V *Atlantis* and ROV *JASON*. Though polyethylene glycols were present in samples from every dive (Table 4.7), carbitol was unique to the Beebe 4 samples from the PVF. It is difficult to pinpoint exactly what could contaminate large volumes of sample during one specific dive, though sample fluids were over 200 °C hotter than any other samples collected using the HOG.

**Table 5.1: Combined samples from SPE extracts for NMR analysis.** Samples were grouped by SPE-DOC aliquot signature, temperature, and geographic position.

| NMR sample name (ID) | Vent contents | Sample IDs | Max temp. (°C) | Aliquot $[C]_{SPE}$ (mg) | $\delta^{13}C_{SPE}$ (‰) |
|---|---|---|---|---|---|
| Background Seawater (I) | - | AT42-22-CTD-02 | 4 | 1.8 | -22.2 |
| | | J2-1244-LV24 | 4 | 1.9 | -22.3 |
| Hot Von Damm (J) | Bartizan | J2-1244-LV23 | 137 | 0.9 | -22.6 |
| | Ravelin 2 | J2-1238-LV23 | 113 | 0.7 | -23.2 |
| | White Castle | J2-1235-LV15 | 175 | 0.3 | -24.2 |
| Intermediate Von Damm (J1)* | Mustard Stand | J2-1243-LV15 | 108 | 0.8 | -23.1 |
| | Old Man Tree | J2-1243-LV23 | 119 | 0.5 | -22.8 |
| Cool Von Damm (K) | Shrimp Hole | J2-1244-LV15 | 23 | 1.8 | -22.3 |
| | X-18** | J2-1235-LV17, 24 | 66 | 2.4 | -23.0 |
| Hot Piccard (L) | Beebe 4 | J2-1242-LV24 | 393 | 1.7 | -25.2 |
| Cool Piccard (M) | Hot Chimlet | J2-1239-LV15 | 98 | 1.4 | -22.4 |
| | Lots of Shrimp | J2-1241-LV15 | 36 | 1.9 | -22.3 |
| | Shrimpocalpyse | J2-1240-LV15 | 94 | 1.7 | -22.4 |

* Sample J1 was later combined into sample J for GC-MS analysis.
** X-18 had two extracts added to sample K for additional carbon.

**Table 5.2: Comparison to literature fractionation between DIC/$CO_2$ and formate.**

| $\delta^{13}C_{formate}$ | $\delta^{13}C_{DIC}$ | $\delta^{13}C_{CO2}$ | $\varepsilon_{formate\text{-}DIC}$ | $\varepsilon_{formate\text{-}CO2}$ | Reference | Reference note |
|---|---|---|---|---|---|---|
| -21.5 | - | -7 | - | -14.5 | Penning and Conrad, 2006 | Steady state equilibrium of chemostat culture |
| -12.1 to -6.8 | - | -5 | - | -7.1 to -1.8 | Lang et al., 2018 | Lost City fluid observations assuming mantle signature of $CO_2$ |
| -17.7 to -9.7 | -8.8 to -0.5 | - | -17.2 to -0.9 | - | Sherwood Lollar et al. 2021 | DIC and formate from Kidd Creek boreholes |
| - | - | - | -14.5 to -10 | - | This study | Equilibrium fractionation model |

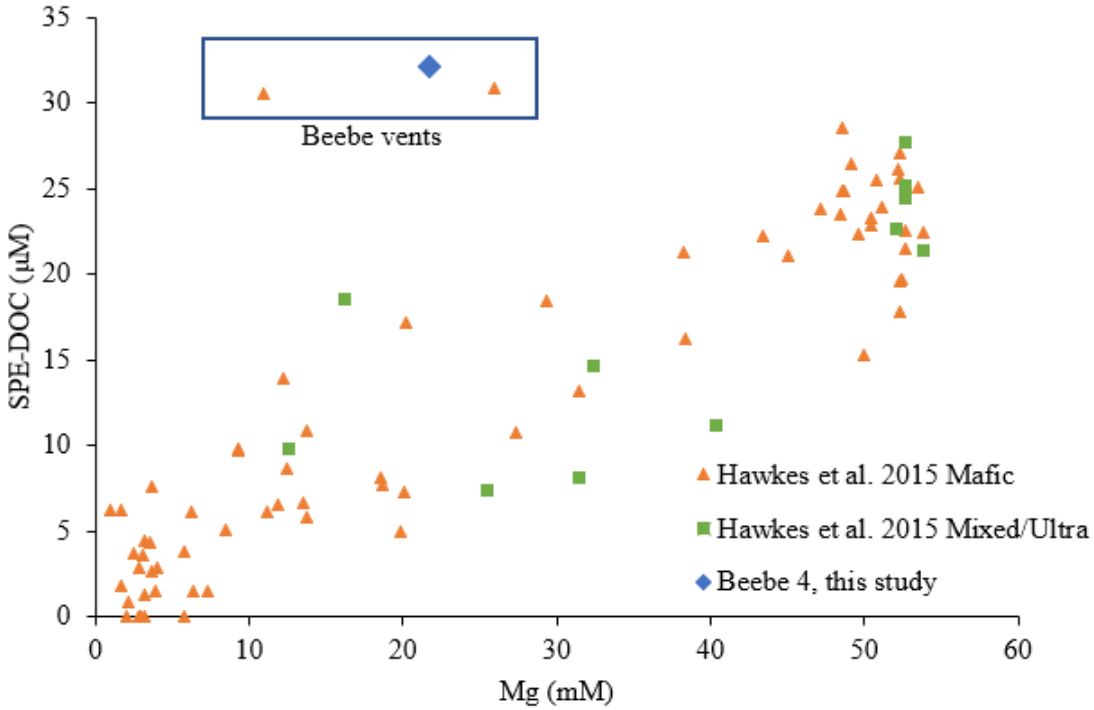


**Figure 5.1: SPE-DOC concentrations for mafic and ultramafic vent fields**. Data are from SI of Hawkes et al. 2015. The SPE-DOC for Beebe 4 is shown as a blue diamond. Values boxed in blue are all from the Beebe vents of the PVF.

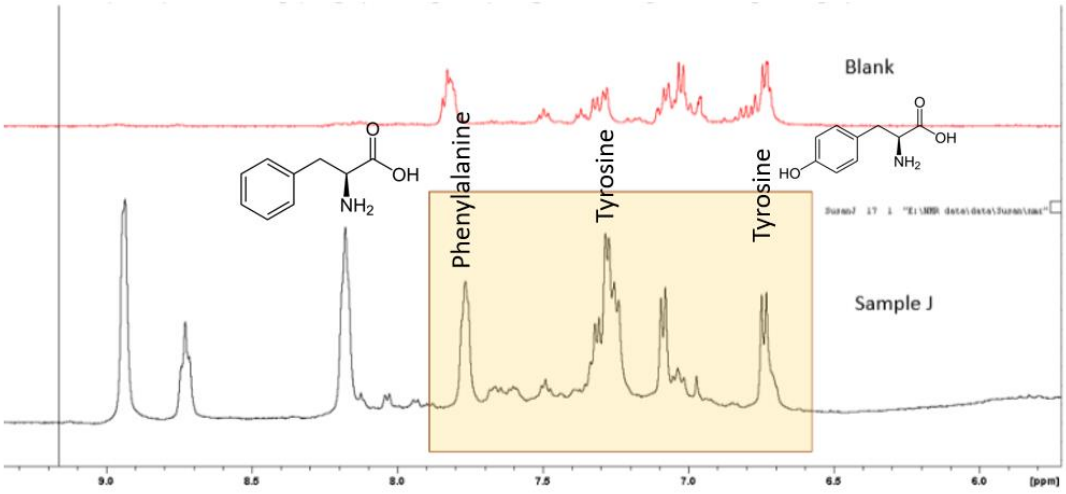


**Figure 5.2: $^{1}$H NMR of the aromatics region between the SPE blank and sample J (Von Damm).** Contamination within the blank was unable to be removed in this region, due to the background presence of phenylalanine (left) and tyrosine (right).

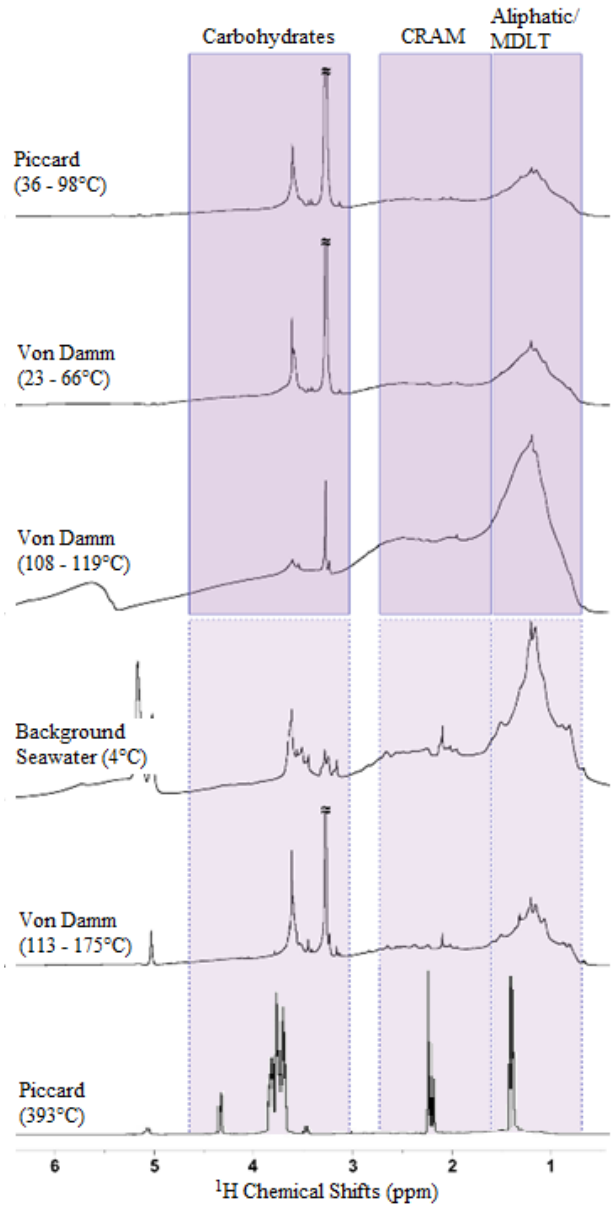


**Figure 5.3: 1H NMR spectra for samples from the Mid-Cayman Rise.**

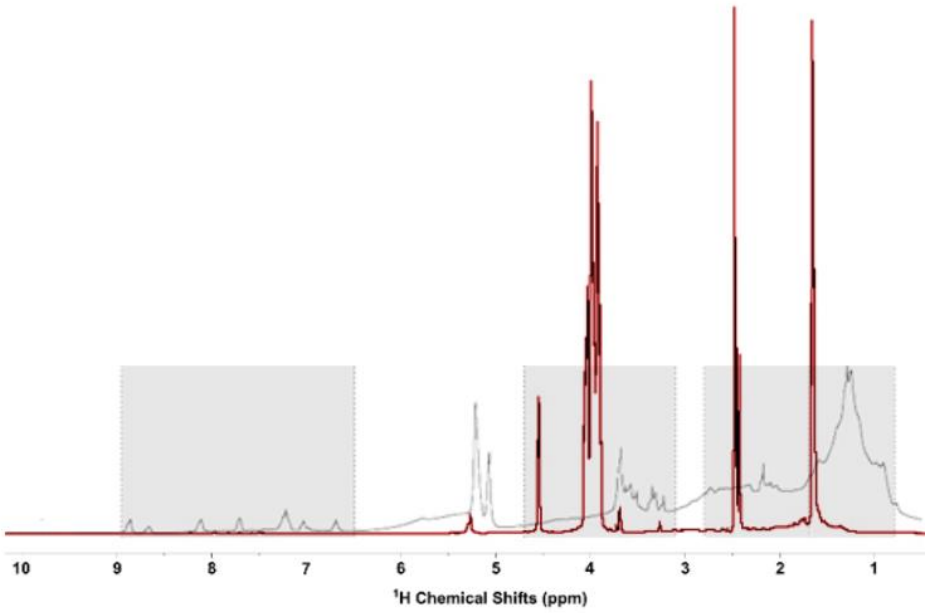


**Figure 5.4: Overlay of $^{1}$H NMR spectra for Beebe 4 (red) and deep seawater SPE extracts (grey).** Rectangles indicate organic characteristics outlined in figure 5.3.

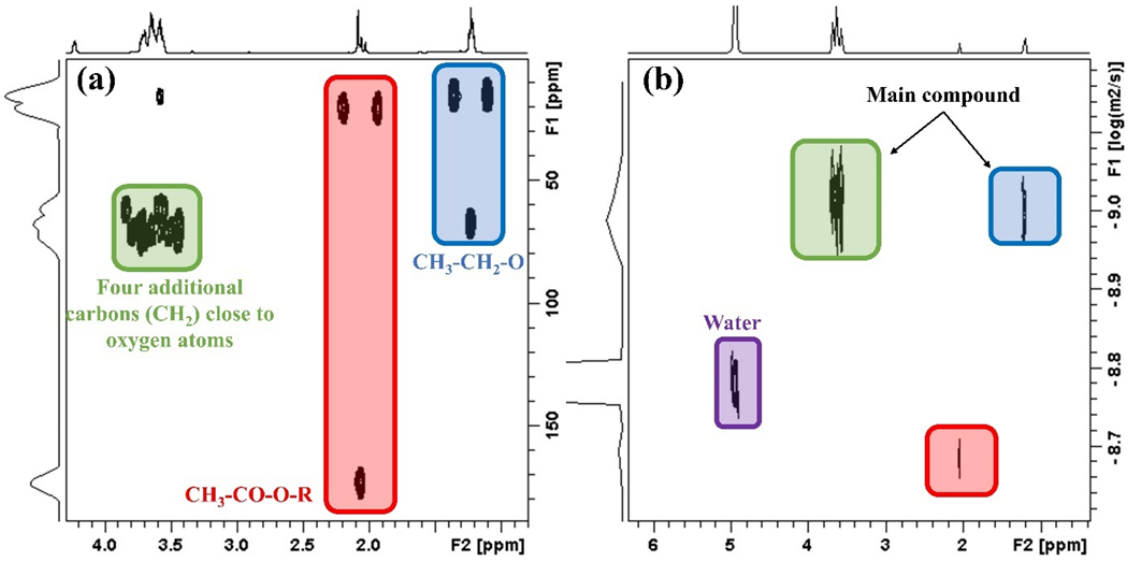


**Figure 5.5: $^{1}$H-$^{13}$C HMBC (a) and $^{1}$H DOSY (b) NMR spectra for sample L.** Blue and green regions correspond to ethoxylated regions of carbitol. The region in red corresponds to an acetic acid-like compound. The purple region is indicative of water, only identifiable in DOSY.

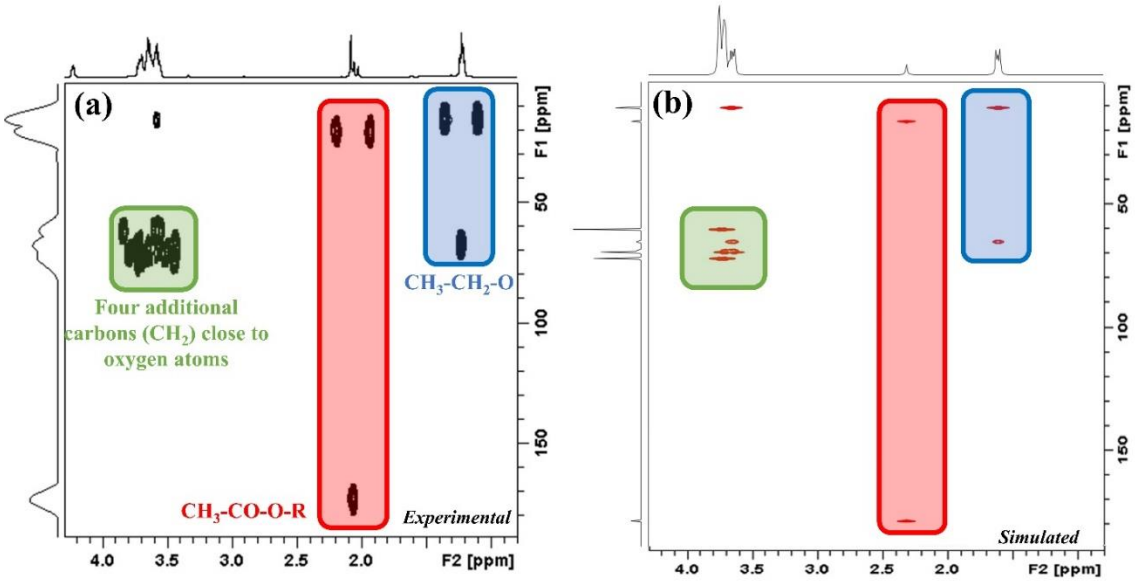


**Figure 5.6: $^{1}$H-$^{13}$C HMBC NMR spectra from Beebe 4 (a) and a simulated carbitol/acetic acid solution (b).** Areas in green and blue indicate the ethoxy chain in carbitol (2-(2-ethoxyethoxy)ethanol) whereas the region in red indicates acetic acid.

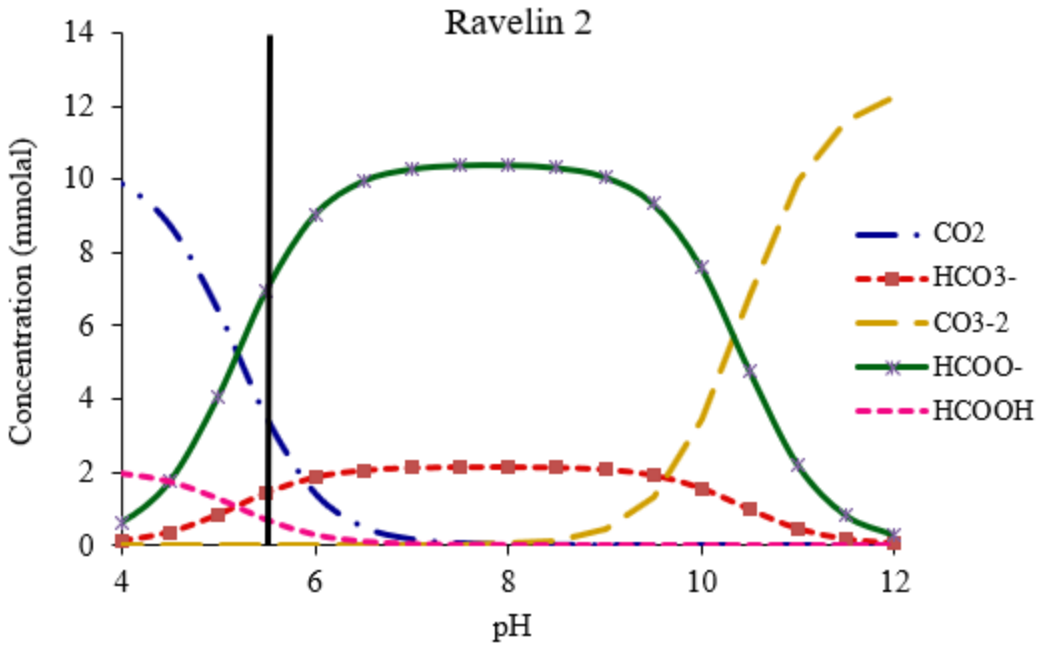


**Figure 5.7: Bjerrum plot of inorganic carbon species, formate, and formic acid at Ravelin 2**. The vertical black line indicates the approximate pH sampled at Ravelin 2, where formate would be the dominant species.

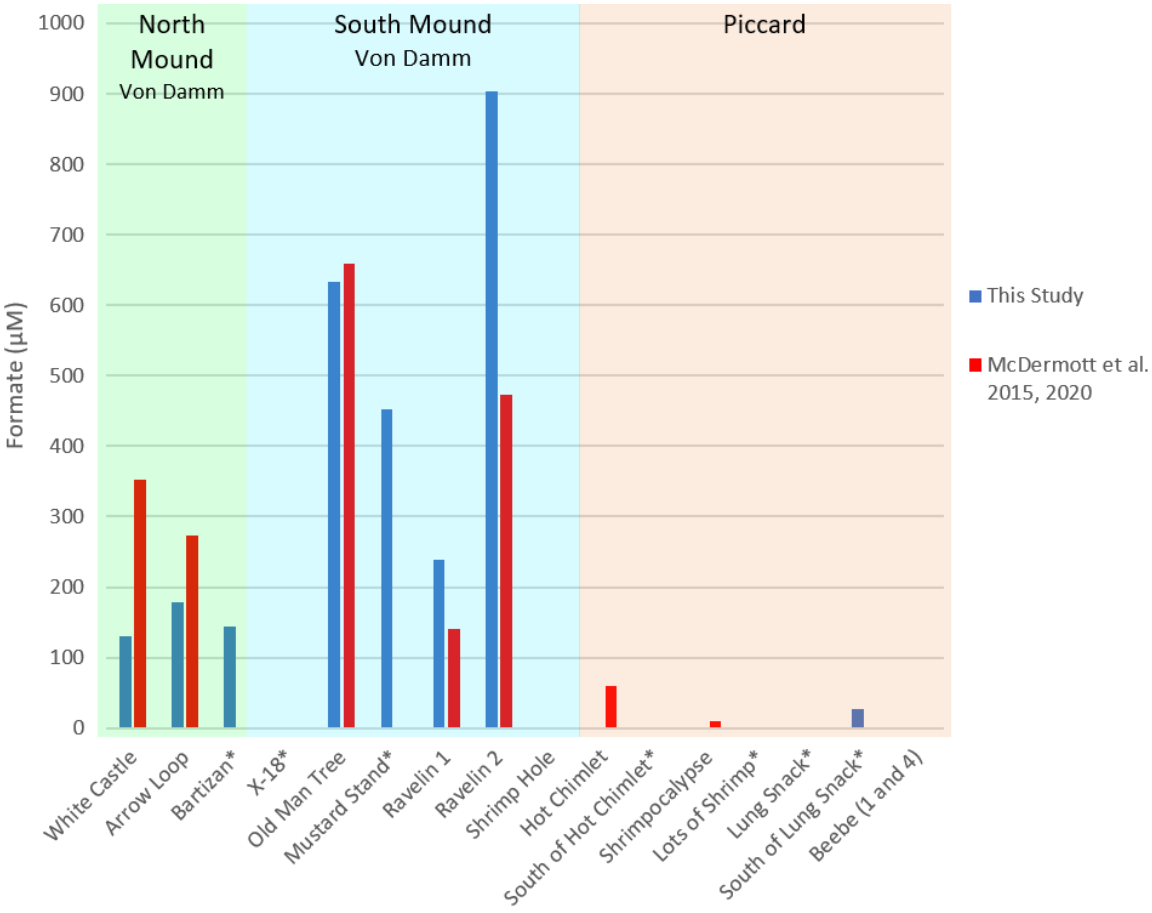


**Figure 5.8: Bar chart of observed formate in this study and those reported in literature.** Asterisks indicate newly-sampled sites not reported in literature.

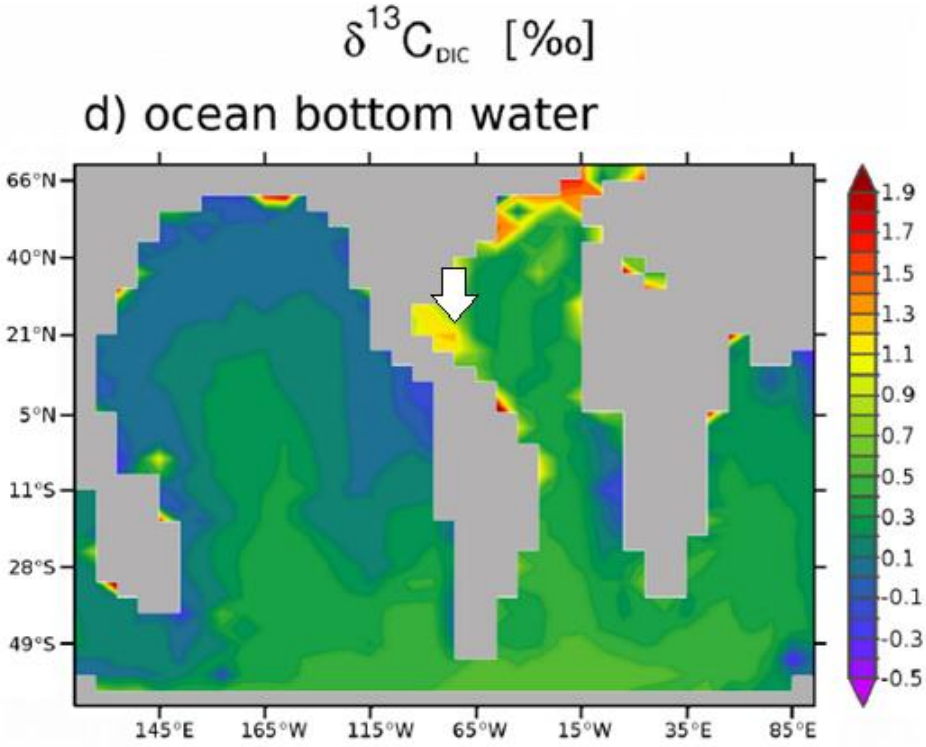


**Figure 5.9: Modeled $\delta^{13}C$ isotopic concentrations for ocean bottom water (Tschumi et al., 2011).** An arrow highlights the MCR.

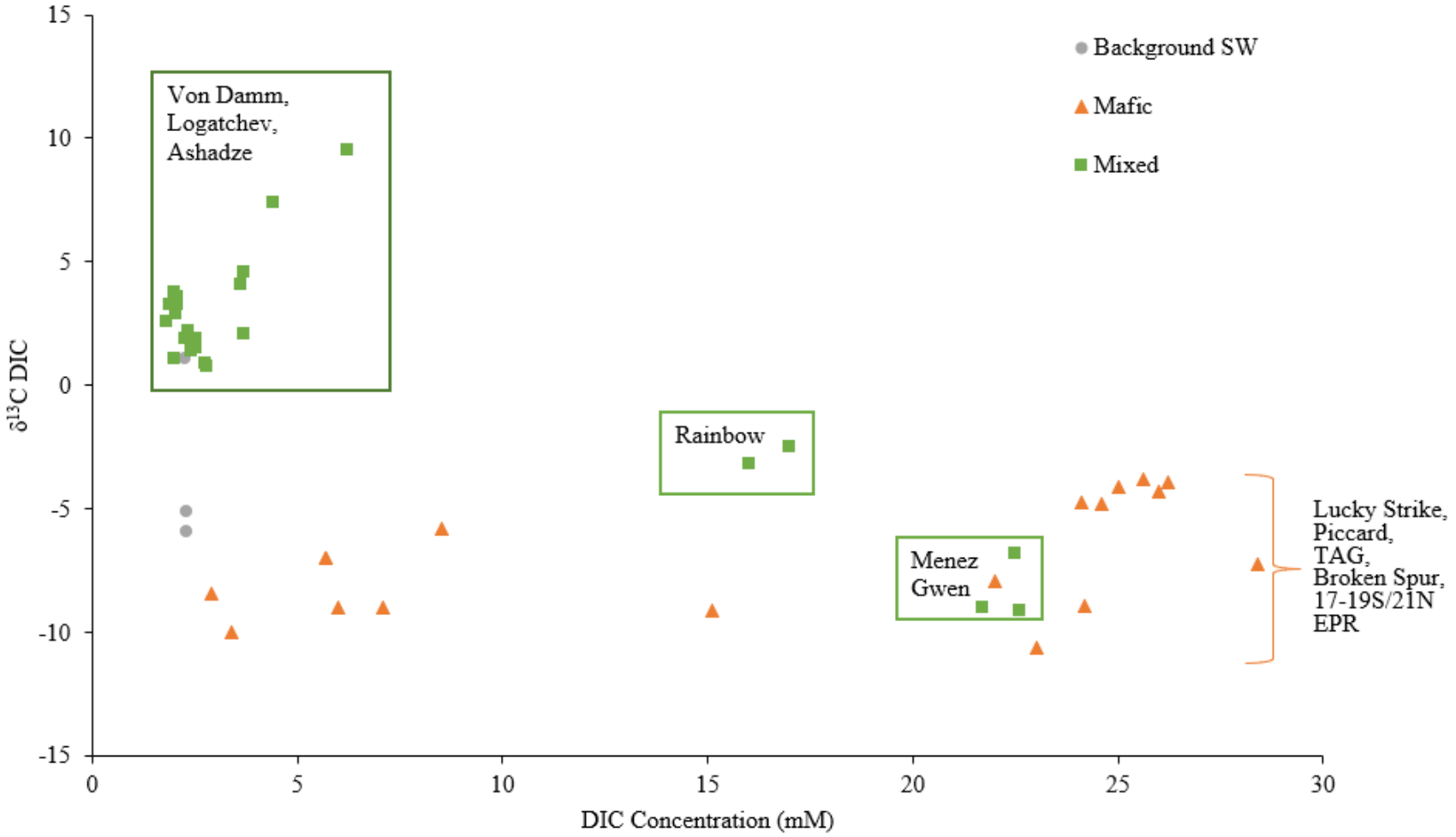


**Figure 5.10: Comparison of MCR DIC $\delta^{13}C$ and concentrations reported in literature.** Data are grouped by host rock type from Charlou et al., 2010; McCollom and Seewald, 2007.

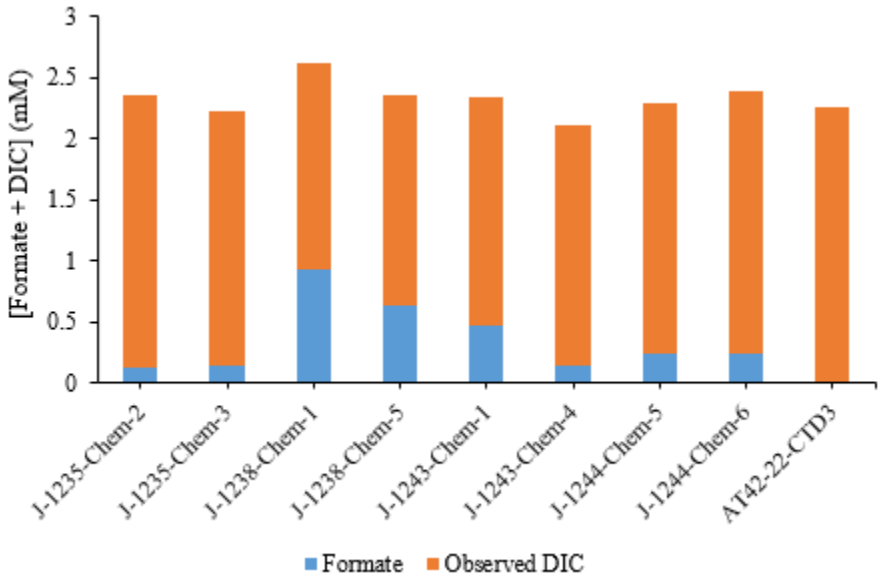


**Figure 5.11: Sums of observed DIC and formate concentrations (mM) for samples taken from Von Damm.** Samples averaged [Formate + DIC] of 2.3 ± 0.12 mM. Samples had Mg concentrations indicating > 50% seawater, with the exception of AT42-22-CTD3.

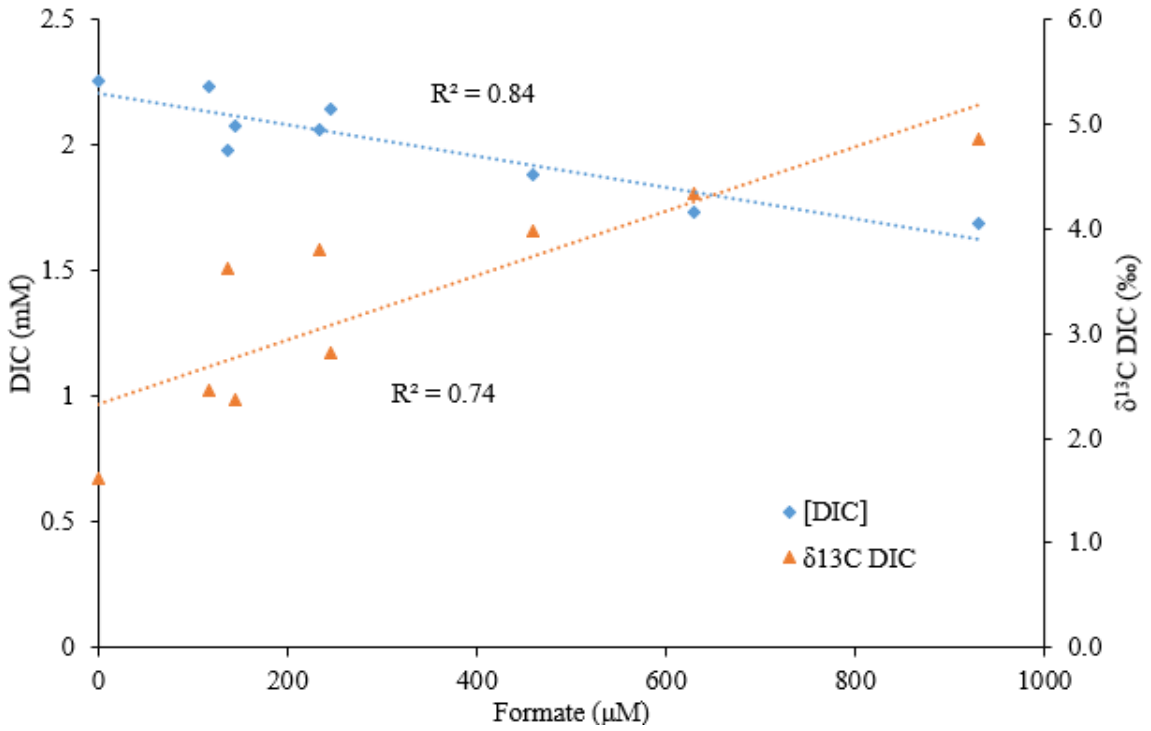


**Figure 5.12: Concentrations (mM, left axis, blue diamonds) and $\delta^{13}C$ (‰, right axis, orange triangles) of DIC plotted against formate (µM).**

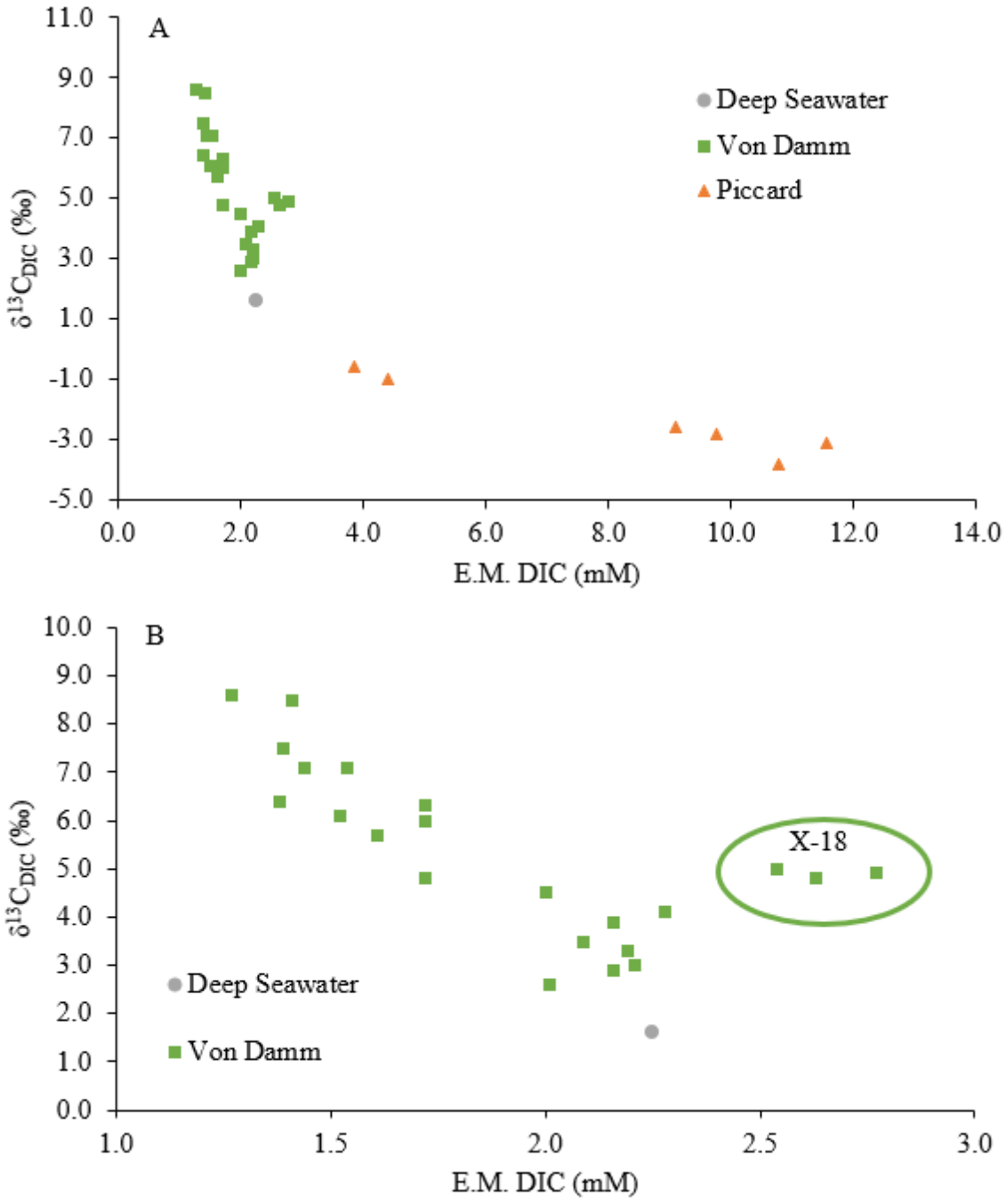


**Figure 5.13: DIC endmember $\delta^{13}C$ and concentration for Von Damm and Piccard (A) and exclusively Von Damm (B).** Values encircled in B are from X-18 and do not have comparable DICs to elsewhere in the field.

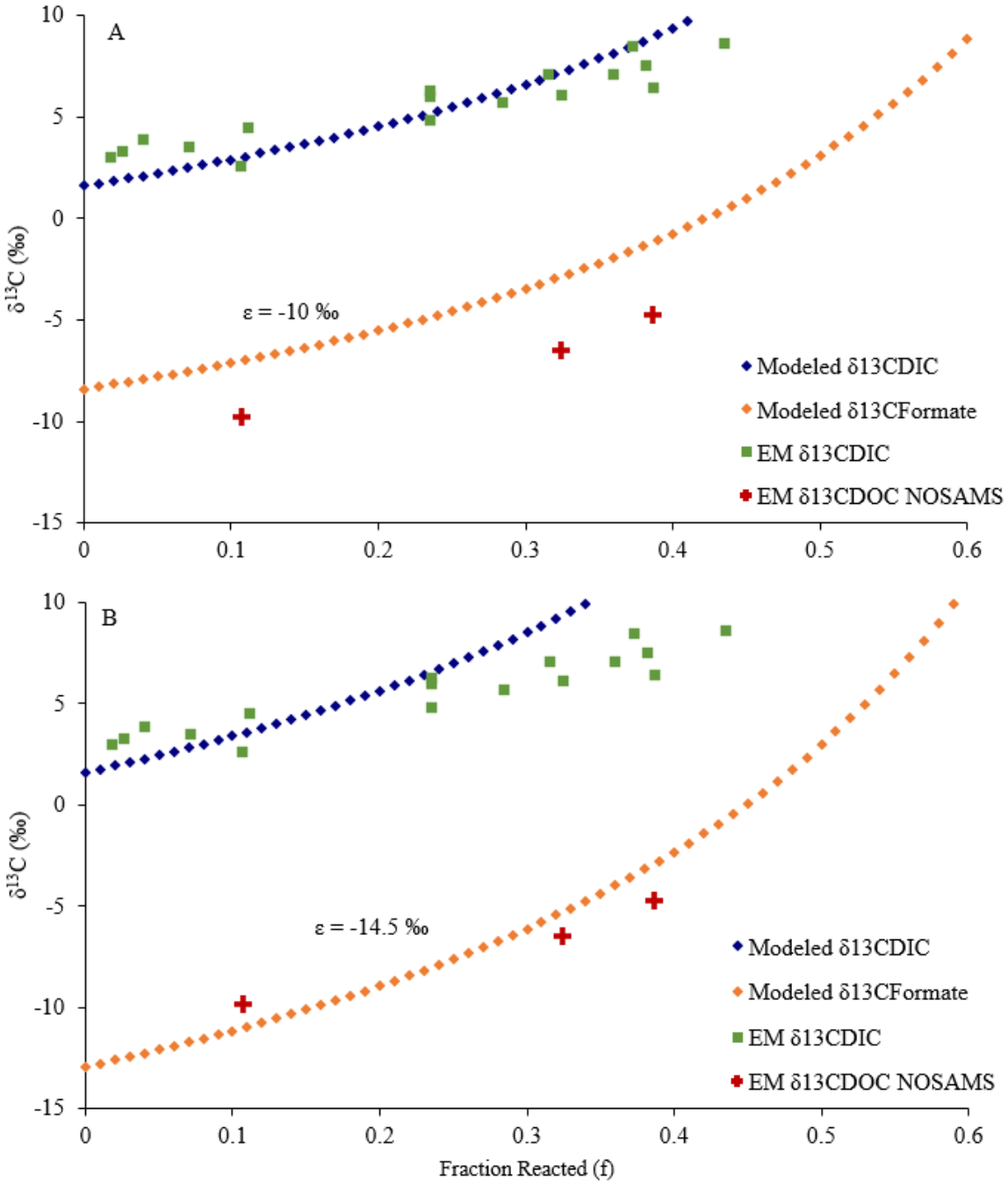


**Figure 5.14: Closed system equilibrium fractionation model between DIC and formate for ε = -10 ‰ (A) and -14.5 ‰ (B).** Endmember DIC $\delta^{13}C$ values from samples are indicated by green squares, whereas NOSAMS $\delta^{13}C_{DOC}$ are indicated by red crosses.

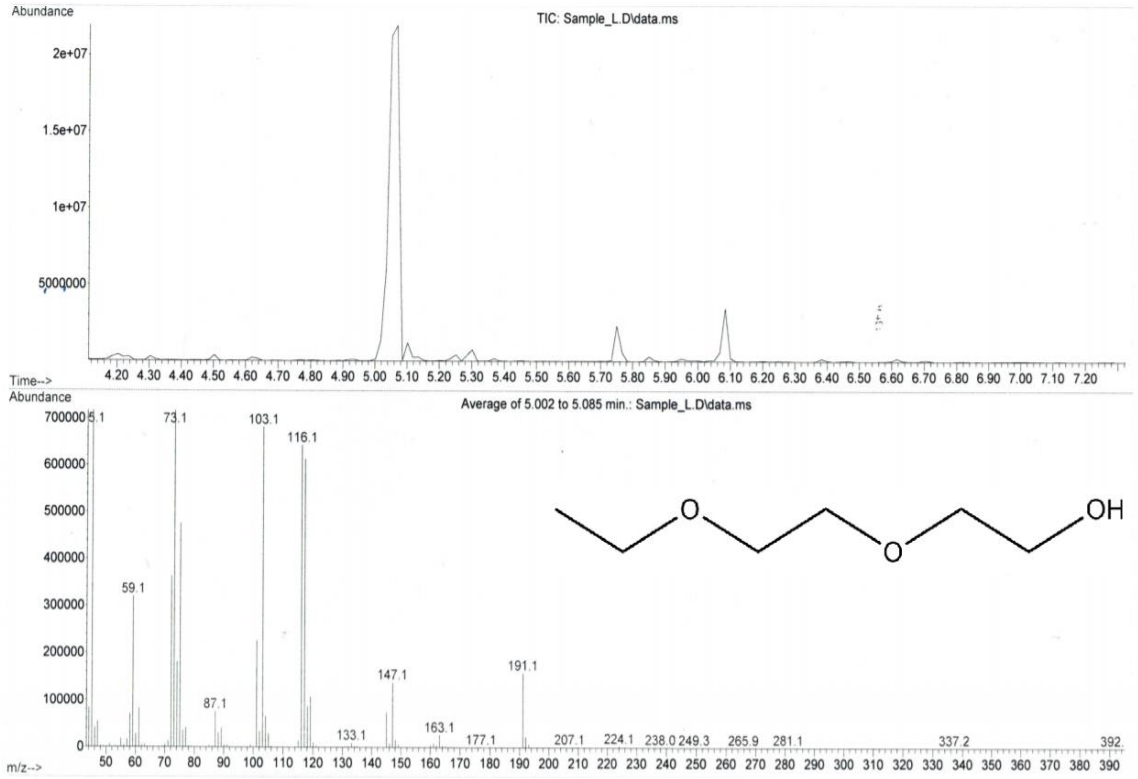


**Figure 5.15: GC-MS Total ion chromatogram (top) with fragmentogram and carbitol structure (bottom).**

# CHAPTER 6: CONCLUSIONS

Dissolved organic carbon is a mystery in both marine and fresh water environments. By assessing the refractory components of DOC at two distinct hydrothermal fields, it was found that refractory DOC was lost at the ultramafic Von Damm vent field. We did not have sufficient data to assess the loss of refractory DOC at the Piccard field. Possible removal mechanisms include sorption to clays, pyrolysis, or microbial heterotrophy. At Piccard, the only site significantly different from background seawater was at a near-supercritical orifice, Beebe 4, which only had a handful of organic compounds as opposed to thousands typically seen in seawater. The identified compound, carbitol, has not previously been reported in hydrothermal systems and may be derived from contamination or other unknown alteration pathways.

The trends observed suggest that ultramafic environments remove refractory DOC from seawater whereas mafic locations, when hot enough, will act to either pyrolyze or homogenize it into fractions which are not retained by conventional sampling methods. In the purview of carbon budgets, ultramafic environments may have a sequestration flux which is underestimated considering how few DOC data have been taken from hydrothermal environments.

When analyzing the labile fraction of DOC at each vent field, Von Damm showed an extreme abundance of the organic acid formate at moderate (T ~ 110 °C) vents.

Ravelin 2, Old Man Tree, and Mustard Stand of the Von Damm Southern Mound had concentrations of formate exceeding 400 μM, which is higher than other unsedimented ultramafic environments such as Lost City (~100 μM). When considering formation pathways, the subsurface entrainment of deep seawater is particularly important to synthesize formate at Von Damm where $H_2$-rich endmember fluids have equilibrated with DIC. Formate was absent from nearly all of Piccard, suggesting that abiotic synthesis is favored at the physiochemical conditions of Von Damm.

The findings presented from this work contribute to a dataset of hydrothermal organic chemistry and demonstrate that different hydrothermal environments have distinct roles on deep water DOC. By understanding Earth's DOC, we can construct analogues to other undiscovered systems or those on other ocean worlds. When considering Earth's carbon budgets, and the origin of life, sites such as those found on the Mid-Cayman Rise can be analogous to other venting systems – terrestrial or not.

# REFERENCES


Albert, D. B., & Martens, C. S. (1997). Determination of low-molecular-weight organic acid concentrations in seawater and pore-water samples via HPLC. *Marine Chemistry*, 56(1–2), 27–37. https://doi.org/10.1016/s0304-4203(96)00083-7

Anderson, R. E., Beltrán, M. T., Hallam, S. J., & Baross, J. A. (2013). Microbial community structure across fluid gradients in the Juan de Fuca Ridge hydrothermal system. *FEMS Microbiology Ecology*, 83(2), 324–339. https://doi.org/10.1111/j.1574-6941.2012.01478.x

Anderson, R. E., Reveillaud, J., Reddington, E., Delmont, T. O., Eren, A. M., McDermott, J. M., Seewald, J. S., & Huber, J. A. (2017). Genomic variation in microbial populations inhabiting the marine subseafloor at deep-sea hydrothermal vents. *Nature Communications*, 8(1). https://doi.org/10.1038/s41467-017-01228-6

Ardyna, M., Lacour, L., Sergi, S., d'Ovidio, F., Sallée, J. B., Rembauville, M., Blain, S., Tagliabue, A., Schlitzer, R., Jeandel, C., Arrigo, K. R., & Claustre, H. (2019). Hydrothermal vents trigger massive phytoplankton blooms in the Southern Ocean. *Nature Communications*, 10(1). https://doi.org/10.1038/s41467-019-09973-6

Beaupré, S. R., Druffel, E. R. M., & Griffin, S. (2007). A low-blank photochemical extraction system for concentration and isotopic analyses of marine dissolved organic carbon. *Limnology and Oceanography: Methods*, 5(6), 174–184. https://doi.org/10.4319/lom.2007.5.174

Beaulieu, S. E., Baker, E. T., German, C. R., & Maffei, A. (2013). An authoritative global database for active submarine hydrothermal vent fields. Geochemistry, Geophysics, Geosystems, 14(11), 4892–4905. https://doi.org/10.1002/2013gc004998

Beaulieu, S.E., Szafranski, K. (2020) InterRidge Global Database of Active Submarine Hydrothermal Vent Fields, Version 3.4. World Wide Web electronic publication available from http://vents-data.interridge.org Accessed 2021-05-21.

Benner, R., Pakulski, J. D., McCarthy, M., Hedges, J. I., & Hatcher, P. G. (1992). Bulk Chemical Characteristics of Dissolved Organic Matter in the Ocean. *Science*, 255(5051), 1561–1564. https://doi.org/10.1126/science.255.5051.1561

Bennett, S. A., Coleman, M., Huber, J. A., Reddington, E., Kinsey, J. C., McIntyre, C., Seewald, J. S., & German, C. R. (2013). Trophic regions of a hydrothermal plume dispersing away from an ultramafic-hosted vent-system: Von Damm vent-site, Mid-Cayman Rise. *Geochemistry, Geophysics, Geosystems*, 14(2), 317–327. https://doi.org/10.1002/ggge.20063

Bischoff, J. L., & Dickson, F. W. (1975). Seawater-basalt interaction at 200°C and 500 bars: Implications for origin of sea-floor heavy-metal deposits and regulation of seawater chemistry. *Earth and Planetary Science Letters*, 25(3), 385–397. https://doi.org/10.1016/0012-821x(75)90257-5

Bischoff, J. L. (1991). Densities of liquids and vapors in boiling NaCl-H 2 O solutions; a PVTx summary from 300 degrees to 500 degrees C. *American Journal of Science*, 291(4), 309–338. https://doi.org/10.2475/ajs.291.4.309

Bourbonnais, A., Lehmann, M. F., Butterfield, D. A., & Juniper, S. K. (2012). Subseafloor nitrogen transformations in diffuse hydrothermal vent fluids of the Juan de Fuca Ridge evidenced by the isotopic composition of nitrate and ammonium. *Geochemistry, Geophysics, Geosystems*, 13(2), n/a. https://doi.org/10.1029/2011gc003863

Broek, T. A. B., Walker, B. D., Guilderson, T. P., Vaughn, J. S., Mason, H. E., & McCarthy, M. D. (2020). Low Molecular Weight Dissolved Organic Carbon: Aging, Compositional Changes, and Selective Utilization During Global Ocean Circulation. *Global Biogeochemical Cycles*, 34(6). https://doi.org/10.1029/2020gb006547

Butterfield, D. A., McDuff, R. E., Mottl, M. J., Lilley, M. D., Lupton, J. E., & Massoth, G. J. (1994). Gradients in the composition of hydrothermal fluids from the endeavour segment vent field: Phase separation and brine loss. *Journal of Geophysical Research: Solid Earth*, 99(B5), 9561–9583. https://doi.org/10.1029/93jb03132

Charlou, J. L., Donval, J. P., Douville, E., Jean-Baptiste, P., Radford-Knoery, J., Fouquet, Y., Dapoigny, A., & Stievenard, M. (2000). Compared geochemical signatures and the evolution of Menez Gwen (37°50′N) and Lucky Strike (37°17′N) hydrothermal fluids, south of the Azores Triple Junction on the mid-atlantic ridge. *Chemical Geology*, 171(1-2), 49–75. https://doi.org/10.1016/s0009-2541(00)00244-8

Charlou, J. L., Donval, J. P., Konn, C., Ondréas, H., Fouquet, Y., Jean-Baptiste, P., & Fourré, E. (2010). High production and fluxes of H2 and CH4 and evidence of abiotic hydrocarbon synthesis by serpentinization in ultramafic-hosted hydrothermal systems on the Mid-Atlantic Ridge. *Geophysical Monograph Series*, 265–296. https://doi.org/10.1029/2008gm000752

Chen, M., Kim, S., Park, J. E., Jung, H. J., & Hur, J. (2016). Structural and compositional changes of dissolved organic matter upon solid-phase extraction tracked by multiple analytical tools. *Analytical and Bioanalytical Chemistry*, 408(23), 6249–6258. https://doi.org/10.1007/s00216-016-9728-0

Cline, J. D. (1969). Spectrophotometric Determination of Hydrogen Sulfide in Natural Waters. *Limnology and Oceanography*, 14(3), 454–458. https://doi.org/10.4319/lo.1969.14.3.0454

Connelly, D. P., Copley, J. T., Murton, B. J., Stansfield, K., Tyler, P. A., German, C. R., Van Dover, C. L., Amon, D., Furlong, M., Grindlay, N., Hayman, N., Hühnerbach, V., Judge, M., Le Bas, T., McPhail, S., Meier, A., Nakamura, K. I., Nye, V., Pebody, M., Pedersen, R., Plouviez, S., Sands, C., Searle, R. C., Stevenson, P., &

Wilcox, S. (2012). Hydrothermal vent fields and chemosynthetic biota on the world's deepest seafloor spreading centre. *Nature Communications*, 3(1). https://doi.org/10.1038/ncomms1636

Conte, P., Abbate, C., Baglieri, A., Nègre, M., Pasquale, C. D., Alonzo, G., & Gennari, M. (2011). Adsorption of dissolved organic matter on clay minerals as assessed by infra-red, CPMAS 13C NMR spectroscopy and low field T1 NMR relaxometry. *Organic Geochemistry*, 42(8), 972–977. https://doi.org/10.1016/j.orggeochem.2011.03.002

Dittmar, T., Koch, B., Hertkorn, N., & Kattner, G. (2008). A simple and efficient method for the solid-phase extraction of dissolved organic matter (SPE-DOM) from seawater. *Limnology and Oceanography: Methods*, 6(6), 230–235. https://doi.org/10.4319/lom.2008.6.230

Druffel, E. R. M., Williams, P. M., Bauer, J. E., & Ertel, J. R. (1992). Cycling of dissolved and particulate organic matter in the open ocean. *Journal of Geophysical Research*, 97(C10), 15639. https://doi.org/10.1029/92jc01511

Druffel, E. R., Griffin, S., Coppola, A. I., & Walker, B. D. (2016). Radiocarbon in dissolved organic carbon of the Atlantic Ocean. *Geophysical Research Letters*, 43(10), 5279–5286. https://doi.org/10.1002/2016gl068746

Foustoukos, D. I., Pester, N. J., Ding, K., & Seyfried, W. E. (2009). Dissolved carbon species in associated diffuse and focused flow hydrothermal vents at the Main Endeavour Field, Juan de Fuca Ridge: Phase equilibria and kinetic constraints. *Geochemistry, Geophysics, Geosystems*, 10(10), n/a. https://doi.org/10.1029/2009gc002472

Fruh-Green, G. L., Kelley, D. S., Bernasconi, S. M., Karson, J. A., Ludwig, K. A., Butterfield, D. A., Boschi, C., & Proskurowski, G. (2003). 30,000 Years of Hydrothermal Activity at the Lost City Vent Field. *Science*, 301(5632), 495–498. https://doi.org/10.1126/science.1085582

Fulignati, P. (2020). Clay Minerals in Hydrothermal Systems. *Minerals*, 10(10), 919. https://doi.org/10.3390/min10100919

German, C. R., Bowen, A., Coleman, M. L., Honig, D. L., Huber, J. A., Jakuba, M. V., Kinsey, J. C., Kurz, M. D., Leroy, S., McDermott, J. M., de Lepinay, B. M., Nakamura, K., Seewald, J. S., Smith, J. L., Sylva, S. P., van Dover, C. L., Whitcomb, L. L., & Yoerger, D. R. (2010). Diverse styles of submarine venting on the ultraslow spreading Mid-Cayman Rise. *Proceedings of the National Academy of Sciences*, 107(32), 14020–14025. https://doi.org/10.1073/pnas.1009205107

Hansell, D. A., Carlson, C. A., & Schlitzer, R. (2012). Net removal of major marine dissolved organic carbon fractions in the subsurface ocean. *Global Biogeochemical Cycles*, 26(1), n/a. https://doi.org/10.1029/2011gb004069

Hansell, D. A. (2013). Recalcitrant Dissolved Organic Carbon Fractions. *Annual Review of Marine Science*, 5(1), 421–445. https://doi.org/10.1146/annurev-marine-120710-100757

Hawkes, J. A., Rossel, P. E., Stubbins, A., Butterfield, D., Connelly, D. P., Achterberg, E. P., Koschinsky, A., Chavagnac, V., Hansen, C. T., Bach, W., & Dittmar, T. (2015). Efficient removal of recalcitrant deep-ocean dissolved organic matter during hydrothermal circulation. *Nature Geoscience*, 8(11), 856–860. https://doi.org/10.1038/ngeo2543

Hawkes, J. A., Hansen, C. T., Goldhammer, T., Bach, W., & Dittmar, T. (2016). Molecular alteration of marine dissolved organic matter under experimental hydrothermal conditions. *Geochimica et Cosmochimica Acta*, 175, 68–85. https://doi.org/10.1016/j.gca.2015.11.025

Hertkorn, N., Benner, R., Frommberger, M., Schmitt-Kopplin, P., Witt, M., Kaiser, K., Kettrup, A., & Hedges, J. I. (2006). Characterization of a major refractory component of marine dissolved organic matter. *Geochimica et Cosmochimica Acta*, 70(12), 2990–3010. https://doi.org/10.1016/j.gca.2006.03.021

Hertkorn, N., Harir, M., Koch, B. P., Michalke, B., & Schmitt-Kopplin, P. (2013). High-field NMR spectroscopy and FTICR mass spectrometry: powerful discovery tools for the molecular level characterization of marine dissolved organic matter. *Biogeosciences*, 10(3), 1583–1624. https://doi.org/10.5194/bg-10-1583-2013

Hodgkinson, M. R. S., Webber, A. P., Roberts, S., Mills, R. A., Connelly, D. P., & Murton, B. J. (2015). Talc-dominated seafloor deposits reveal a new class of hydrothermal system. *Nature Communications*, 6(1). https://doi.org/10.1038/ncomms10150

Huber, J. A., Mark Welch, D. B., Morrison, H. G., Huse, S. M., Neal, P. R., Butterfield, D. A., & Sogin, M. L. (2007). Microbial population structures in the deep marine biosphere. *Science*, 318(5847), 97–100. https://doi.org/10.1126/science.1146689

Ito, E., & Anderson, A.T. (1983). Submarine metamorphism of gabbros from the Mid-Cayman Rise: Petrographic and mineralogic constraints on hydrothermal processes at slow-spreading ridges. *Contrib Mineral Petrol 82*, 371–388. https://doi.org/10.1007/BF00399714

Iyer, K., Jamtveit, B., Mathiesen, J., Malthesorenssen, A., & Feder, J. (2008). Reaction-assisted hierarchical fracturing during serpentinization. *Earth and Planetary Science Letters*, 267(3-4), 503–516. https://doi.org/10.1016/j.epsl.2007.11.060

Jiao, N., Herndl, G. J., Hansell, D. A., Benner, R., Kattner, G., Wilhelm, S. W., Kirchman, D. L., Weinbauer, M. G., Luo, T., Chen, F., & Azam, F. (2010). Microbial production of recalcitrant dissolved organic matter: long-term carbon storage in the global ocean. *Nature Reviews Microbiology*, 8(8), 593–599. https://doi.org/10.1038/nrmicro2386

Johnson, W. M., Kido Soule, M. C., & Kujawinski, E. B. (2017). Extraction efficiency and quantification of dissolved metabolites in targeted marine metabolomics. *Limnology and Oceanography: Methods*, 15(4), 417–428. https://doi.org/10.1002/lom3.10181

Karl, D. M., Wirsen, C. O., & Jannasch, H. W. (1980). Deep-Sea Primary Production at the Galápagos Hydrothermal Vents. *Science*, 207(4437), 1345–1347. http://www.jstor.org/stable/168344

Kawagucci, S., Matsui, Y., & Früh-Green, G. L. (2020). Radiocarbon content of carbon dioxide and methane in hydrothermal fluids of Okinawa Trough vents. *GEOCHEMICAL JOURNAL*, 54(3), 129–138. https://doi.org/10.2343/geochemj.2.0595

Kelley, D. S., Karson, J. A., Fruh-Green, G. L., Yoerger, D. R., Shank, T. M., Butterfield, D. A., Hayes, J. M., Schrenk, M. O., Olson, E. J., Proskurowski, G., Jakuba, M., Bradley, A., Larson, B., Ludwig, K. A., Glickson, D., Buckman, K., Bradley, A. S., Brazelton, W. J., Roe, K., Elend, M. J., Delacour, A., Bernasconi, S. M., Lilley, M. D., Baross, J. A., Summons, R. E., & Sylva, S. P. (2005). A Serpentinite-Hosted Ecosystem: The Lost City Hydrothermal Field. *Science*, 307(5714), 1428–1434. https://doi.org/10.1126/science.1102556

Klein, E. M., & Langmuir, C. H. (1987). Global correlations of ocean ridge basalt chemistry with axial depth and crustal thickness. *Journal of Geophysical Research*, 92(B8), 8089. https://doi.org/10.1029/jb092ib08p08089

Konn, C., Charlou, J., Donval, J., Holm, N., Dehairs, F., & Bouillon, S. (2009). Hydrocarbons and oxidized organic compounds in hydrothermal fluids from Rainbow and Lost City ultramafic-hosted vents. *Chemical Geology*, 258(3–4), 299–314. https://doi.org/10.1016/j.chemgeo.2008.10.034

Konn, C., Charlou, J. L., Donval, J. P., & Holm, N. G. (2011). Characterisation of dissolved organic compounds in hydrothermal fluids by stir bar sorptive extraction - gas chomatography - mass spectrometry. Case study: the Rainbow field (36°N, Mid-Atlantic Ridge). *Geochemical Transactions*, 13(1). https://doi.org/10.1186/1467-4866-13-8

Kvenvolden, K. A., & Simoneit, B. R. (1990). Hydrothermally derived petroleum: Examples from Guaymas Basin, Gulf of California, and Escanaba Trough, Northeast Pacific Ocean. *AAPG Bulletin*, 74. https://doi.org/10.1306/0c9b22a9-1710-11d7-8645000102c1865d

Lang, S. Q., Butterfield, D. A., Lilley, M. D., Paul Johnson, H., & Hedges, J. I. (2006). Dissolved organic carbon in ridge-axis and ridge-flank hydrothermal systems. *Geochimica et Cosmochimica Acta*, 70(15), 3830–3842. https://doi.org/10.1016/j.gca.2006.04.031

Lang, S. Q., Butterfield, D. A., Schulte, M., Kelley, D. S., & Lilley, M. D. (2010). Elevated concentrations of formate, acetate and dissolved organic carbon found at the Lost City hydrothermal field. *Geochimica et Cosmochimica Acta*, 74(3), 941–952. https://doi.org/10.1016/j.gca.2009.10.045

Lang, S. Q., Bernasconi, S. M., & Früh-Green, G. L. (2012). Stable isotope analysis of organic carbon in small (μg C) samples and dissolved organic matter using a GasBench preparation device. *Rapid Communications in Mass Spectrometry*, 26(1), 9–16. https://doi.org/10.1002/rcm.5287

Lang, S. Q., Früh-Green, G. L., Bernasconi, S. M., Brazelton, W. J., Schrenk, M. O., & McGonigle, J. M. (2018). Deeply-sourced formate fuels sulfate reducers but not methanogens at Lost City hydrothermal field. *Scientific Reports*, 8(1). https://doi.org/10.1038/s41598-017-19002-5

Lang, S., Osburn, M., & Steen, A. (2019). Carbon in the Deep Biosphere: Forms, Fates, and Biogeochemical Cycling. In B. Orcutt, I. Daniel, & R. Dasgupta (Eds.), Deep Carbon: Past to Present (pp. 480-523). *Cambridge: Cambridge University Press*.

Lang, S. Q., & Benitez-Nelson, B. (2021). Hydrothermal Organic Geochemistry (HOG) sampler for deployment on deep-sea submersibles. *Deep Sea Research Part I: Oceanographic Research Papers*, 173, 103529. https://doi.org/10.1016/j.dsr.2021.103529

Lang, S. Q., Lilley, M. D., Baumberger, T., Früh-Green, G. L., Walker, S. L., Brazelton, W. J., Kelley, D. S., Elend, M., Butterfield, D. A., & Mau, A. J. (2021). Extensive decentralized hydrogen export from the Atlantis Massif. *Geology*. Published. https://doi.org/10.1130/g48322.1

Lévy, L., Fridriksson, T., Findling, N., Lanson, B., Fraisse, B., Marino, N., & Gibert, B. (2020). Smectite quantification in hydrothermally altered volcanic rocks. *Geothermics*, 85, 101748. https://doi.org/10.1016/j.geothermics.2019.101748

Lewis, C. B., Walker, B. D., & Druffel, E. R. (2020). Isotopic and optical heterogeneity of solid phase extracted marine dissolved organic carbon. *Marine Chemistry*, 219, 103752. https://doi.org/10.1016/j.marchem.2020.103752

Li, Y., Harir, M., Uhl, J., Kanawati, B., Lucio, M., Smirnov, K. S., Koch, B. P., Schmitt-Kopplin, P., & Hertkorn, N. (2017). How representative are dissolved organic matter (DOM) extracts? A comprehensive study of sorbent selectivity for DOM isolation. *Water Research*, 116, 316–323. https://doi.org/10.1016/j.watres.2017.03.038

Li, J., Mara, P., Schubotz, F., Sylvan, J. B., Burgaud, G., Klein, F., Beaudoin, D., Wee, S. Y., Dick, H. J. B., Lott, S., Cox, R., Meyer, L. A. E., Quémener, M., Blackman, D. K., & Edgcomb, V. P. (2020). Recycling and metabolic flexibility dictate life in the lower oceanic crust. *Nature*, 579(7798), 250–255. https://doi.org/10.1038/s41586-020-2075-5

Lilley, M. D., Butterfield, D. A., Olson, E. J., Lupton, J. E., Macko, S. A., & McDuff, R. E. (1993). Anomalous CH4 and NH4+ concentrations at an unsedimented mid-ocean-ridge hydrothermal system. *Nature*, 364(6432), 45–47. https://doi.org/10.1038/364045a0

Lin, H. T., Cowen, J. P., Olson, E. J., Amend, J. P., & Lilley, M. D. (2012). Inorganic chemistry, gas compositions and dissolved organic carbon in fluids from sedimented young basaltic crust on the Juan de Fuca Ridge flanks. *Geochimica et Cosmochimica Acta*, 85, 213–227. https://doi.org/10.1016/j.gca.2012.02.017

Lin, H. T., Amend, J. P., LaRowe, D. E., Bingham, J. P., & Cowen, J. P. (2015). Dissolved amino acids in oceanic basaltic basement fluids. *Geochimica et Cosmochimica Acta*, 164, 175–190. https://doi.org/10.1016/j.gca.2015.04.044

Lin, H. T., Repeta, D. J., Xu, L., & Rappé, M. S. (2019). Dissolved organic carbon in basalt-hosted deep subseafloor fluids of the Juan de Fuca Ridge flank. *Earth and Planetary Science Letters*, 513, 156–165. https://doi.org/10.1016/j.epsl.2019.02.008

Lin, Y. S., Koch, B. P., Feseker, T., Ziervogel, K., Goldhammer, T., Schmidt, F., Witt, M., Kellermann, M. Y., Zabel, M., Teske, A., & Hinrichs, K. U. (2017). Near-surface Heating of Young Rift Sediment Causes Mass Production and Discharge of Reactive Dissolved Organic Matter. *Scientific Reports*, 7(1). https://doi.org/10.1038/srep44864

Lollar, B., Heuer, V., McDermott, J., Tille, S., Warr, O., Moran, J., Telling, J., & Hinrichs, K. U. (2021). A window into the abiotic carbon cycle – Acetate and formate in fracture waters in 2.7 billion year-old host rocks of the Canadian Shield. *Geochimica et Cosmochimica Acta*, 294, 295–314. https://doi.org/10.1016/j.gca.2020.11.026

Lowell, R. P., & Rona, P. A. (2002). Seafloor hydrothermal systems driven by the serpentinization of peridotite. *Geophysical Research Letters*, 29(11). https://doi.org/10.1029/2001gl014411

Ludwig, K. A., Kelley, D. S., Butterfield, D. A., Nelson, B. K., & Früh-Green, G. (2006). Formation and evolution of carbonate chimneys at the Lost City Hydrothermal Field. *Geochimica et Cosmochimica Acta*, 70(14), 3625–3645. https://doi.org/10.1016/j.gca.2006.04.016

Macdonald, A. H., & Fyfe, W. S. (1985). Rate of serpentinization in seafloor environments. *Tectonophysics*, 116(1–2), 123–135. https://doi.org/10.1016/0040-1951(85)90225-2

Martin, W., Baross, J., Kelley, D., & Russell, M. J. (2008). Hydrothermal vents and the origin of life. *Nature Reviews Microbiology*, 6(11), 805–814. https://doi.org/10.1038/nrmicro1991

McCarthy, M. D., Beaupré, S. R., Walker, B. D., Voparil, I., Guilderson, T. P., & Druffel, E. R. M. (2010). Chemosynthetic origin of 14C-depleted dissolved organic matter in a ridge-flank hydrothermal system. *Nature Geoscience*, 4(1), 32–36. https://doi.org/10.1038/ngeo1015

McCollom, T. M., Ritter, G., & Simoneit, B. R. T. (1999a). Lipid Synthesis Under Hydrothermal Conditions By Fischer-Tropsch-Type Reactions. *Origins of Life and Evolution of the Biosphere*, 29(2), 153–166. https://doi.org/10.1023/a:1006592502746

McCollom, T. M., Simoneit, B. R. T., & Shock, E. L. (1999b). Hydrous Pyrolysis of Polycyclic Aromatic Hydrocarbons and Implications for the Origin of PAH in Hydrothermal Petroleum. *Energy & Fuels*, 13(2), 401–410. https://doi.org/10.1021/ef980089i

McCollom, T. M., & Seewald, J. S. (2003a). Experimental constraints on the hydrothermal reactivity of organic acids and acid anions: I. Formic acid and formate. *Geochimica et Cosmochimica Acta*, 67(19), 3625–3644. https://doi.org/10.1016/s0016-7037(03)00136-4

McCollom, T. M., & Seewald, J. S. (2003b). Experimental study of the hydrothermal reactivity of organic acids and acid anions: II. Acetic acid, acetate, and valeric acid. *Geochimica et Cosmochimica Acta*, 67(19), 3645–3664. https://doi.org/10.1016/s0016-7037(03)00135-2

McCollom, T. M., & Bach, W. (2009). Thermodynamic constraints on hydrogen generation during serpentinization of ultramafic rocks. *Geochimica et Cosmochimica Acta*, 73(3), 856–875. https://doi.org/10.1016/j.gca.2008.10.032

McDermott, J. M., Seewald, J. S., German, C. R., & Sylva, S. P. (2015). Pathways for abiotic organic synthesis at submarine hydrothermal fields. *Proceedings of the National Academy of Sciences*, 112(25), 7668–7672. https://doi.org/10.1073/pnas.1506295112

McDermott, J. M., Sylva, S. P., Ono, S., German, C. R., & Seewald, J. S. (2018). Geochemistry of fluids from Earth's deepest ridge-crest hot-springs: Piccard hydrothermal field, Mid-Cayman Rise. *Geochimica et Cosmochimica Acta*, 228, 95–118. https://doi.org/10.1016/j.gca.2018.01.021

McDermott, J. M., Sylva, S. P., Ono, S., German, C. R., & Seewald, J. S. (2020). Abiotic redox reactions in hydrothermal mixing zones: Decreased energy availability for the subsurface biosphere. *Proceedings of the National Academy of Sciences*, 117(34), 20453–20461. https://doi.org/10.1073/pnas.2003108117

McNichol, A. P., & Aluwihare, L. I. (2007). The Power of Radiocarbon in Biogeochemical Studies of the Marine Carbon Cycle: Insights from Studies of Dissolved and Particulate Organic Carbon (DOC and POC). *Chemical Reviews*, 107(2), 443–466. https://doi.org/10.1021/cr050374g

Meinzer, O. E. (1934). The history and development of ground-water hydrology. *Journal of the Washington Academy of Sciences*, 24(1), 6–32. http://www.jstor.org/stable/24532897

Meyer, J. L., Jaekel, U., Tully, B. J., Glazer, B. T., Wheat, C. G., Lin, H.-T., Hsieh, C.-C., Cowen, J. P., Hulme, S. M., Girguis, P. R., & Huber, J. A. (2016). A distinct and active bacterial community in cold oxygenated fluids circulating beneath the western flank of the Mid-Atlantic Ridge. *Scientific Reports*, 6(1). https://doi.org/10.1038/srep22541

Morrison, J. M., & Nowlin, W. D. (1982). General distribution of water masses within the eastern Caribbean Sea during the winter of 1972 and fall of 1973. *Journal of Geophysical Research*, 87(C6), 4207. https://doi.org/10.1029/jc087ic06p04207

Palandri, J. L., & Reed, M. H. (2004). Geochemical models of metasomatism in ultramafic systems: serpentinization, rodingitization, and sea floor carbonate chimney precipitation. *Geochimica et Cosmochimica Acta*, 68(5), 1115–1133. https://doi.org/10.1016/j.gca.2003.08.006

Penning, H., & Conrad, R. (2006). Carbon isotope effects associated with mixed-acid fermentation of saccharides by clostridium papyrosolvens. *Geochimica Et Cosmochimica Acta*, 70(9), 2283–2297. https://doi.org/10.1016/j.gca.2006.01.017

Perner, M., Hansen, M., Seifert, R., Strauss, H., Koschinsky, A., & Petersen, S. (2013). Linking geology, fluid chemistry, and microbial activity of basalt- and ultramafic-hosted deep-sea hydrothermal vent environments. *Geobiology*, 11(4), 340–355. https://doi.org/10.1111/gbi.12039

Peters, J., Murray, R., Sparks, J., & Coleman, D. (2000). Terrigenous matter and dispersed ash in sediment from the Caribbean Sea: results from Leg 165. *Proceedings of the Ocean Drilling Program*, 165 Scientific Results. Published. https://doi.org/10.2973/odp.proc.sr.165.003.2000

Pizzarello, S., Davidowski, S. K., Holland, G. P., & Williams, L. B. (2013). Processing of meteoritic organic materials as a possible analog of early molecular evolution in planetary environments. *Proceedings of the National Academy of Sciences*, 110(39), 15614–15619. https://doi.org/10.1073/pnas.1309113110

Proskurowski, G., Lilley, M. D., Seewald, J. S., Fru h-Green, G. L., Olson, E. J., Lupton, J. E., Sylva, S. P., & Kelley, D. S. (2008). Abiogenic Hydrocarbon Production at Lost City Hydrothermal Field. *Science*, 319(5863), 604–607. https://doi.org/10.1126/science.1151194

Reddy, C. M., Pearson, A., Xu, L., McNichol, A. P., Benner, B. A., Wise, S. A., Klouda, G. A., Currie, L. A., & Eglinton, T. I. (2002). Radiocarbon as a tool to apportion the sources of polycyclic aromatic hydrocarbons and black carbon in environmental samples. *Environmental Science & Technology*, 36(8), 1774–1782. https://doi.org/10.1021/es011343f

Reid, W. D. K., Sweeting, C. J., Wigham, B. D., Zwirglmaier, K., Hawkes, J. A., McGill, R. A. R., Linse, K., & Polunin, N. V. C. (2013). Spatial Differences in East Scotia Ridge Hydrothermal Vent Food Webs: Influences of Chemistry, Microbiology and Predation on Trophodynamics. *PLoS ONE*, 8(6), e65553. https://doi.org/10.1371/journal.pone.0065553

Reimer, P. J., Brown, T. A., & Reimer, R. W. (2004). Discussion: Reporting and calibration of post-bomb 14C data. *Radiocarbon*, 46(3), 1299–1304. https://doi.org/10.1017/s0033822200033154

Reveillaud, J., Reddington, E., McDermott, J., Algar, C., Meyer, J. L., Sylva, S., Seewald, J., German, C. R., & Huber, J. A. (2016). Subseafloor microbial communities in hydrogen-rich vent fluids from hydrothermal systems along the Mid- Cayman Rise. *Environmental Microbiology*, 18(6), 1970–1987. https://doi.org/10.1111/1462-2920.13173

Rushdi, A. I., & Simoneit, B. R. (2006). Abiotic condensation synthesis of glyceride lipids and wax esters under simulated hydrothermal conditions. *Origins of Life and Evolution of Biospheres*, 36(2), 93–108. https://doi.org/10.1007/s11084-005-9001-6

Saidy, A., Smernik, R., Baldock, J., Kaiser, K., & Sanderman, J. (2013). The sorption of organic carbon onto differing clay minerals in the presence and absence of hydrous iron oxide. *Geoderma*, 209–210, 15–21. https://doi.org/10.1016/j.geoderma.2013.05.026

Savage, P. E. (1999). Organic chemical reactions in supercritical water. *Chemical Reviews*, 99(2), 603–622. https://doi.org/10.1021/cr9700989

Scheuermann, P. P., Xing, Y., Ding, K., & Seyfried, W. E. (2020). Experimental measurement of H2(aq) solubility in hydrothermal fluids: Application to the Piccard hydrothermal field, Mid-Cayman Rise. *Geochimica et Cosmochimica Acta*, 283, 22–39. https://doi.org/10.1016/j.gca.2020.05.020

Seewald, J. S., & Seyfried, W. E. (1990). The effect of temperature on metal mobility in subseafloor hydrothermal systems: constraints from basalt alteration experiments. *Earth and Planetary Science Letters*, 101(2–4), 388–403. https://doi.org/10.1016/0012-821x(90)90168-w

Seewald, J. S. (2003). Organic–inorganic interactions in petroleum-producing sedimentary basins. Nature, 426(6964), 327–333. https://doi.org/10.1038/nature02132

Seewald, J. S., Zolotov, M. Y., & McCollom, T. (2006). Experimental investigation of single carbon compounds under hydrothermal conditions. *Geochimica et Cosmochimica Acta*, 70(2), 446–460. https://doi.org/10.1016/j.gca.2005.09.002

Seyfried, W. E., & Mottl, M. J. (1982). Hydrothermal alteration of basalt by seawater under seawater-dominated conditions. *Geochimica et Cosmochimica Acta*, 46(6), 985–1002. https://doi.org/10.1016/0016-7037(82)90054-0

Seyfried, W. E., Berndt, M. E., & Seewald, J. S. (1988). Hydrothermal alteration processes at mid-ocean ridges; constraints from diabase alteration experiments, hot spring fluids and composition of the oceanic crust. *The Canadian Mineralogist*, 26 (3): 787–804.

Shen, Y., & Benner, R. (2018). Mixing it up in the ocean carbon cycle and the removal of refractory dissolved organic carbon. *Scientific Reports*, 8(1). https://doi.org/10.1038/s41598-018-20857-5

Shock, E. L., & Schulte, M. D. (1998). Organic synthesis during fluid mixing in hydrothermal systems. *Journal of Geophysical Research: Planets*, 103(E12), 28513–28527. https://doi.org/10.1029/98je02142

Shock, E. L., & Canovas, P. (2010). The potential for abiotic organic synthesis and biosynthesis at seafloor hydrothermal systems. *Geofluids*. Published. https://doi.org/10.1111/j.1468-8123.2010.00277.x

Shock, E. L., Canovas, P., Yang, Z., Boyer, G., Johnson, K., Robinson, K., Fecteau, K., Windman, T., & Cox, A. (2013). Thermodynamics of Organic Transformations in Hydrothermal Fluids. *Reviews in Mineralogy and Geochemistry*, 76(1), 311–350. https://doi.org/10.2138/rmg.2013.76.9

Simoneit, B. R. T., Goodfellow, W. D., & Franklin, J. M. (1992). Hydrothermal petroleum at the seafloor and organic matter alteration in sediments of Middle Valley, Northern Juan de Fuca Ridge. *Applied Geochemistry*, 7(3), 257–264. https://doi.org/10.1016/0883-2927(92)90041-z

Simoneit, B. R. T. (1993). Aqueous high-temperature and high-pressure organic geochemistry of hydrothermal vent systems. *Geochimica Et Cosmochimica Acta*, 57(14), 3231–3243. https://doi.org/10.1016/0016-7037(93)90536-6

Simoneit, B. R., Rushdi, A. I., & Deamer, D. W. (2007). Abiotic formation of acylglycerols under simulated hydrothermal conditions and self-assembly properties of such lipid products. *Advances in Space Research*, 40(11), 1649–1656. https://doi.org/10.1016/j.asr.2007.07.034

Simpson, A. J., McNally, D. J., & Simpson, M. J. (2011). NMR spectroscopy in environmental research: From molecular interactions to global processes. *Progress in Nuclear Magnetic Resonance Spectroscopy*, 58(3–4), 97–175. https://doi.org/10.1016/j.pnmrs.2010.09.001

Simpson, A. J., Simpson, M. J., & Soong, R. (2017). Environmental nuclear magnetic resonance spectroscopy: An overview and a primer. *Analytical Chemistry*, 90(1), 628–639. https://doi.org/10.1021/acs.analchem.7b03241

Tagliabue, A., Bopp, L., Dutay, J. C., Bowie, A. R., Chever, F., Jean-Baptiste, P., Bucciarelli, E., Lannuzel, D., Remenyi, T., Sarthou, G., Aumont, O., Gehlen, M., & Jeandel, C. (2010). Hydrothermal contribution to the oceanic dissolved iron inventory. *Nature Geoscience*, 3(4), 252–256. https://doi.org/10.1038/ngeo818

Takai, K., Gamo, T., Tsunogai, U., Nakayama, N., Hirayama, H., Nealson, K. H., & Horikoshi, K. (2004). Geochemical and microbiological evidence for a hydrogen-based, hyperthermophilic subsurface lithoautotrophic microbial ecosystem (HyperSLiME) beneath an active deep-sea hydrothermal field. *Extremophiles*, 8(4), 269–282. https://doi.org/10.1007/s00792-004-0386-3

Tschumi, T., Joos, F., Gehlen, M., & Heinze, C. (2011). Deep ocean ventilation, carbon isotopes, marine sedimentation and the deglacial CO2 rise. *Climate of the Past*, 7(3), 771–800. https://doi.org/10.5194/cp-7-771-2011

Tudor, A., Fowler, A., Foustoukos, D. I., Moskowitz, B., Wang, L., Tan, C., & Seyfried, W. E. (2021). Geochemistry of vapor-dominated hydrothermal vent deposits in Yellowstone Lake, Wyoming. *Journal of Volcanology and Geothermal Research*, 414, 107231. https://doi.org/10.1016/j.jvolgeores.2021.107231

Von Damm, K., Edmond, J., Measures, C., & Grant, B. (1985). Chemistry of submarine hydrothermal solutions at Guaymas Basin, Gulf of California. *Geochimica et Cosmochimica Acta*, 49(11), 2221–2237. https://doi.org/10.1016/0016-7037(85)90223-6

Walter, S. R., Jaekel, U., Osterholz, H., Fisher, A. T., Huber, J. A., Pearson, A., Dittmar, T., & Girguis, P. R. (2018). Microbial decomposition of marine dissolved organic matter in cool oceanic crust. *Nature Geoscience*, 11(5), 334–339. https://doi.org/10.1038/s41561-018-0109-5

Watson, R. J., Butler, E. C. V., Clementson, L. A., & Berry, K. M. (2005). Flow-injection analysis with fluorescence detection for the determination of trace levels of ammonium in seawater. *Journal of Environmental Monitoring*, 7(1), 37. https://doi.org/10.1039/b405924g

Webber, A. P., Roberts, S., Murton, B. J., & Hodgkinson, M. R. S. (2015). Geology, sulfide geochemistry and supercritical venting at the Beebe Hydrothermal Vent Field, Cayman Trough. *Geochemistry, Geophysics, Geosystems*, 16(8), 2661–2678. https://doi.org/10.1002/2015gc005879

Yang, Y., Zhao, W., & Xiao, X. (2021). The upper temperature limit of life under high hydrostatic pressure in the deep biosphere. *Deep Sea Research Part I: Oceanographic Research Papers*, *176*, 103604. https://doi.org/10.1016/j.dsr.2021.103604

Zigah, P. K., McNichol, A. P., Xu, L., Johnson, C., Santinelli, C., Karl, D. M., & Repeta, D. J. (2017). Allochthonous sources and dynamic cycling of ocean dissolved organic carbon revealed by carbon isotopes. *Geophysical Research Letters*, 44(5), 2407–2415. https://doi.org/10.1002/2016gl071348

# APPENDIX A: SUPPLEMENTARY INFORMATION

**Table A.1: Site-specific DOC and SPE-DOC acquired via TOC.**

| SPE Sample Designator | Site | n | Mg (mmol/kg) | SPE-DOC (μM) | SPE-DOC stdev (μM) | Bulk DOC (μM) | SPE Recovery (%) | Formate (μM) | Unknown Carbon (μM) |
|---|---|---|---|---|---|---|---|---|---|
| AT42-22-CTD-002-B11 | Deep Seawater | 5 | 52.3 | 35.5 | 6.3 | 44.0 | 80.8 | bdl | 8.5 |
| J-1235-LV15 | White Castle | 2 | 10.7 | 13.2 | 8.7 | 177.6 | 7.4 | 145.6 | 18.8 |
| J-1235-LV17 | X-18 | 4 | 41.9 | 25.0 | 2.3 | 56.9 | 44.1 | bdl | 31.8 |
| J-1235-LV24 | X-18 | 4 | 39.3 | 21.5 | 7.9 | 56.9 | 37.9 | bdl | 35.3 |
| J-1238-LV23 | Ravelin 2 | 4 | 16.1 | 12.0 | 4.3 | 957.5 | 1.2 | 902.7 | 42.8 |
| J-1239-LV15 | Hot Chimlet | 5 | 45.2 | 23.9 | 3.1 | 41.3 | 57.9 | bdl | 17.4 |
| J-1240-LV15 | Shrimpocalypse | 4 | 46.2 | 22.8 | 3.8 | 54.0 | 42.2 | bdl | 31.2 |
| J-1241-LV15 | Lots of Shrimp | 3 | - | 32.2 | 6.9 | 60.0 | 53.7 | bdl | 27.8 |
| J-1242-LV24 | BB4 | 4 | 21.7 | 22.9 | 5.2 | 81.4 | 28.1 | bdl | 58.5 |
| J-1243-LV15 | Mustard Stand | 5 | 23.4 | 10.2 | 3.4 | 452.3 | 2.3 | 419.6 | 22.5 |
| J-1243-LV23 | Old Man Tree | 4 | - | 7.0 | 5.6 | 645.7 | 1.1 | 630.0 | 8.7 |
| J-1244-LV15 | Shrimp Hole | 4 | 48.9 | 24.2 | 2.3 | 53.6 | 45.1 | bdl | 29.4 |
| J-1244-LV23 | Bartizan | 4 | 21.8 | 13.4 | 1.9 | 183.3 | 7.3 | 126.1 | 43.8 |
| J-1244-LV24 | Deep Seawater | 5 | - | 33.8 | 5.2 | 46.5 | 72.6 | bdl | 12.7 |

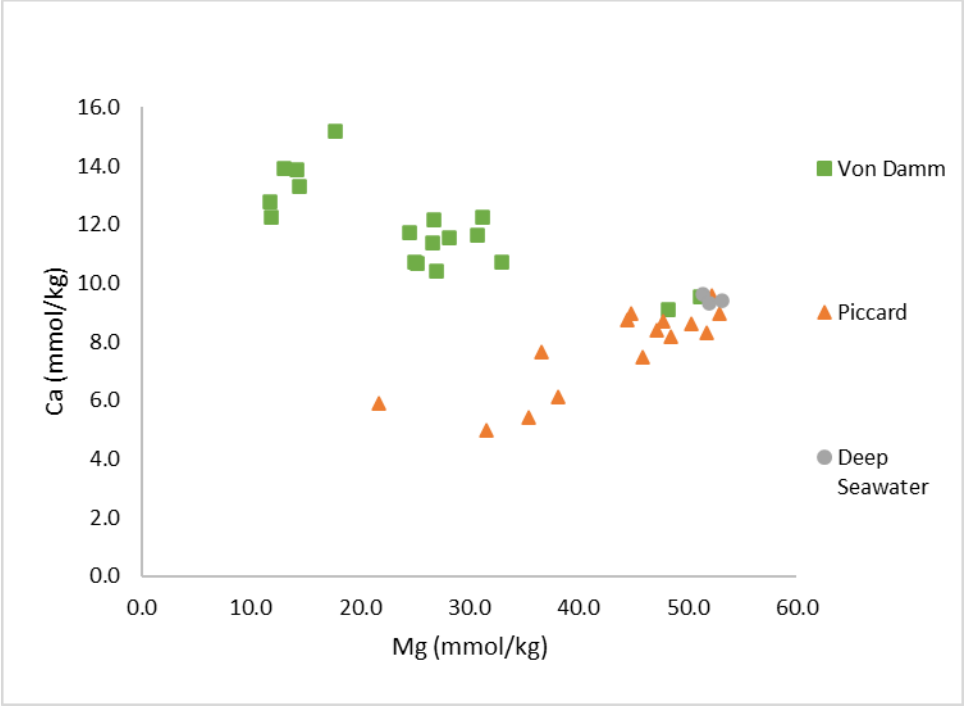


**Figure A.1: Major ion plot of Ca versus Mg for Von Damm and Piccard.**

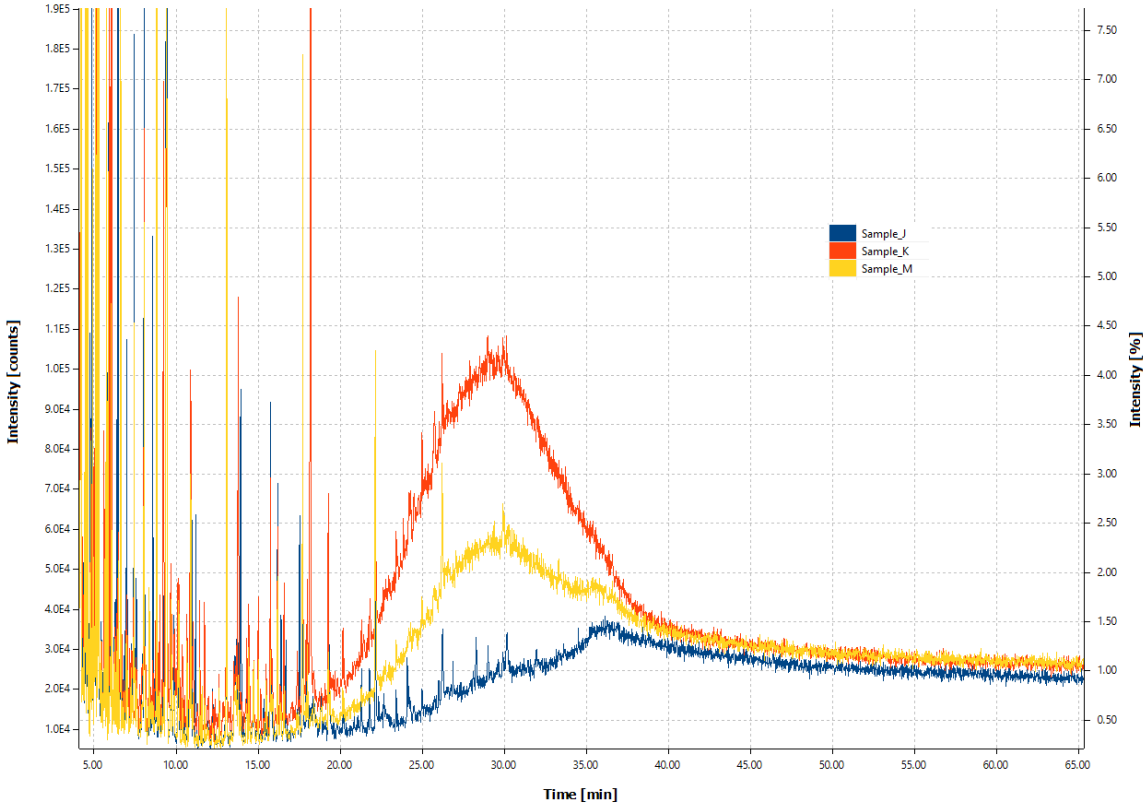


**Figure A.2: GC-MS chromatograms for NMR samples J, K, and M from the Mid-Cayman Rise.** The UCM hump is present to some extent between 20 and 36 minutes.

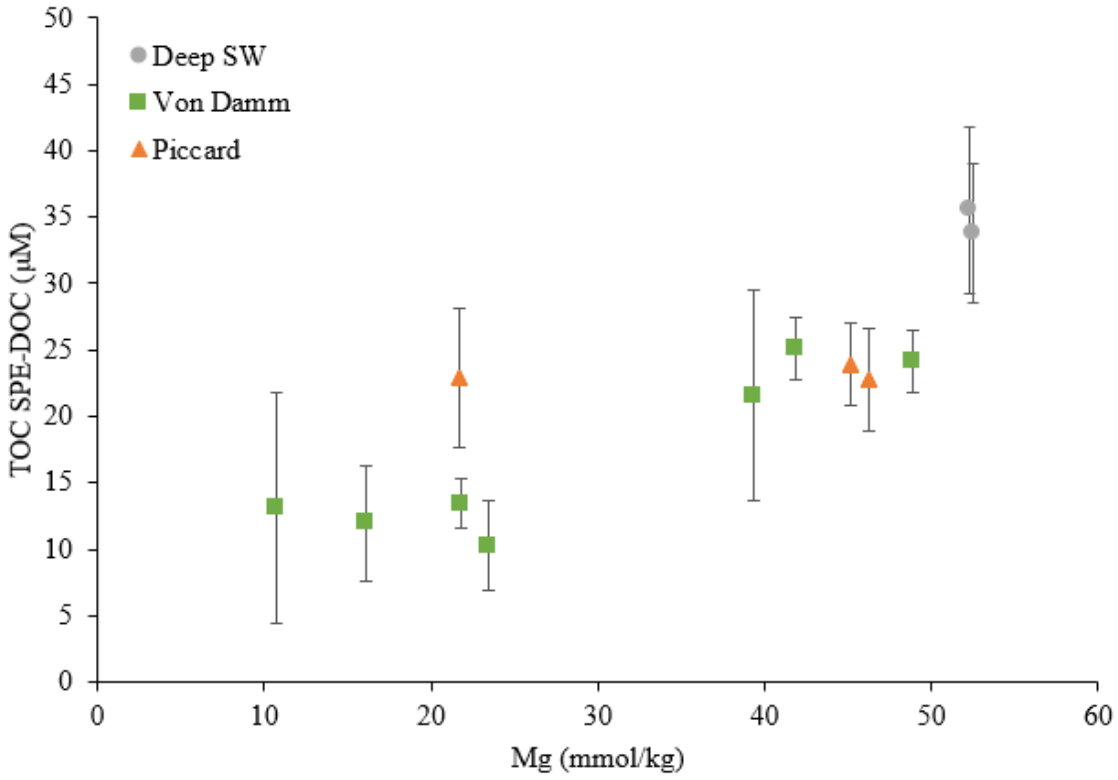


**Figure A.3: Mean sample SPE-DOC concentrations from Shimadzu TOC plotted against Mg.** Error bars are indicative of one standard deviation from the mean.

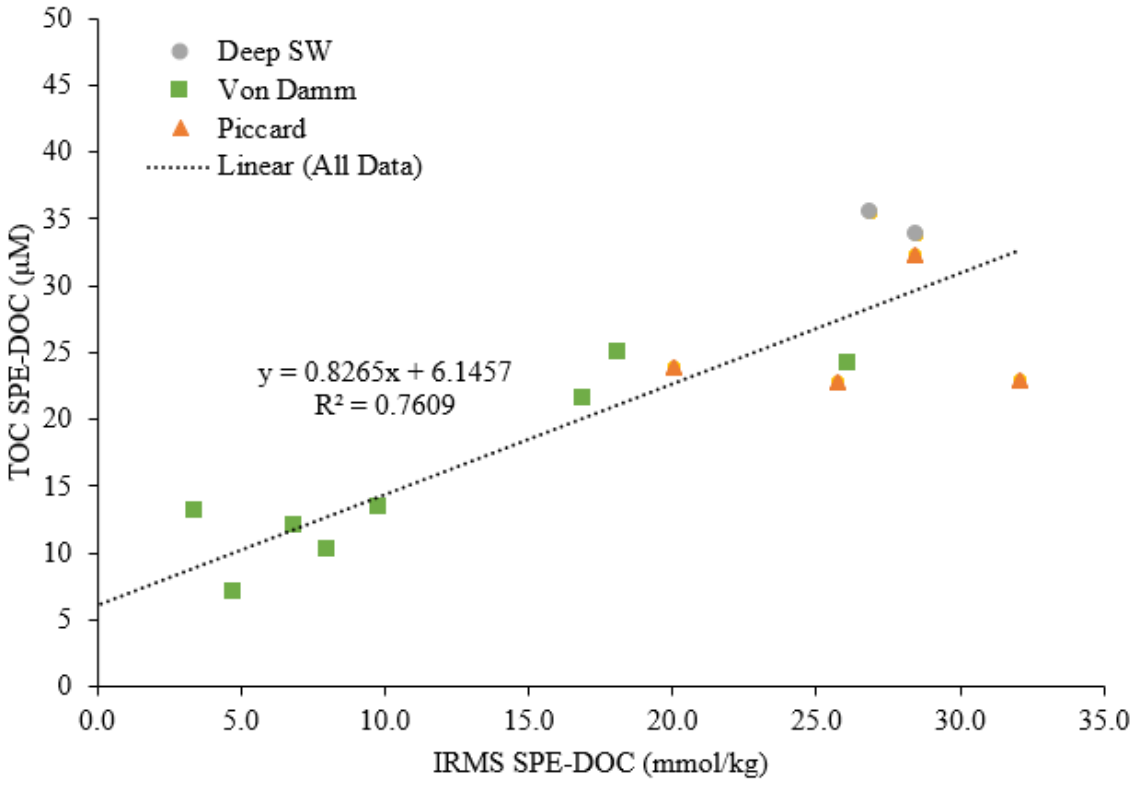


**Figure A.4: Shimadzu TOC SPE-DOC vs IRMS SPE-DOC concentrations.** A linear trendline is provided for all data, indicating Shimadzu TOC SPE-DOC tends to be higher for MCR samples.

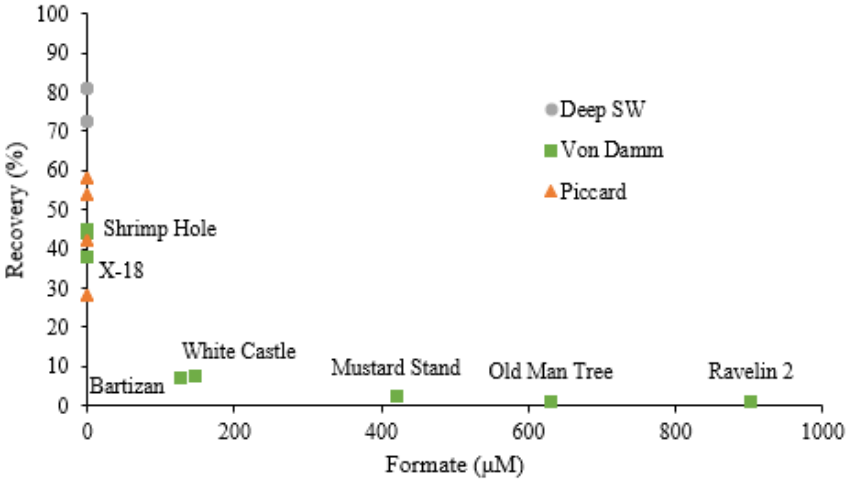


**Figure A.5: Shimadzu TOC SPE-DOC Recovery (%) plotted against formate concentration (µM).**

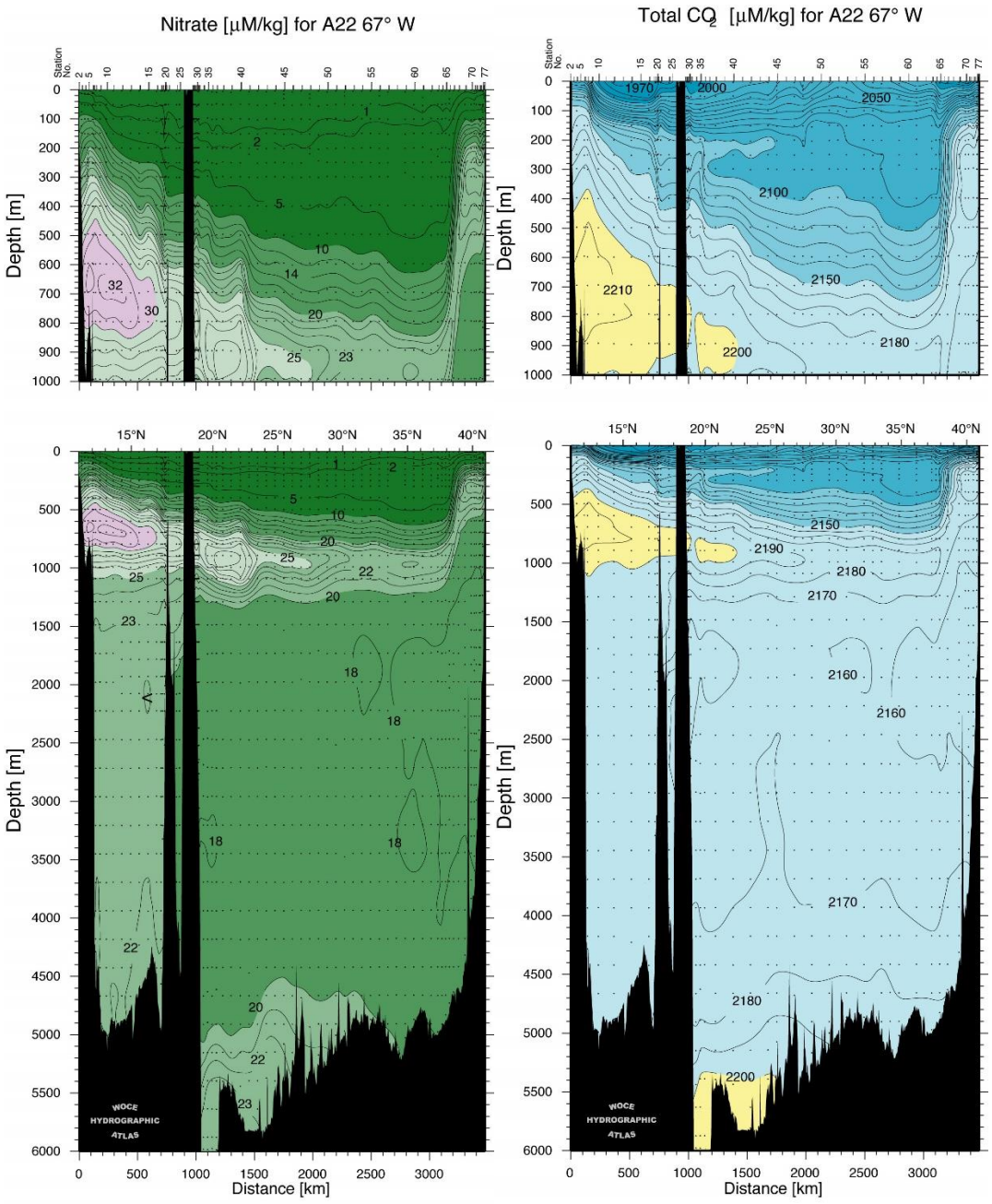


**Figure A.6: Nitrate (left) and total $CO_2$ (right) from WOCE cruise A-22.** Top panels provide greater detail at 0 – 1000 m depth. Figures from WOCE Atlas 3 (http://whp-atlas.ucsd.edu/atlantic/a22/sections/printatlas/printatlas.htm).

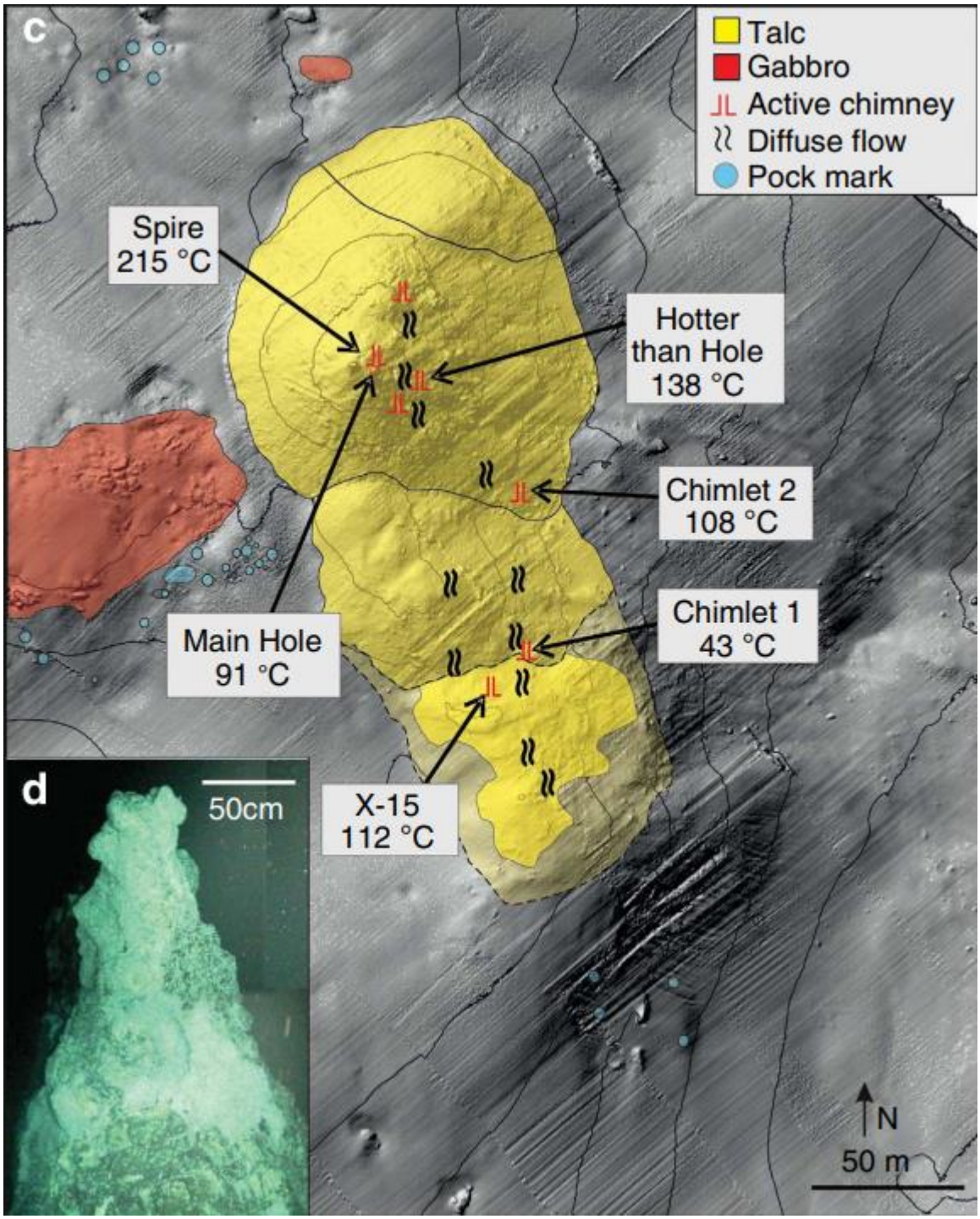


**Figure A.7: Bathymetry of the VDVF with highlighted rock types and features (c).** The Northern Mound is indicated by the talc feature with the hottest venting sites, such as Spire and Hotter than Hole. The Southern Mound is defined by milder temperatures to the south, including X-15 and Chimlet 1. A photomosaic of the Spire is given in (d). Figure from Webber et al. 2015.

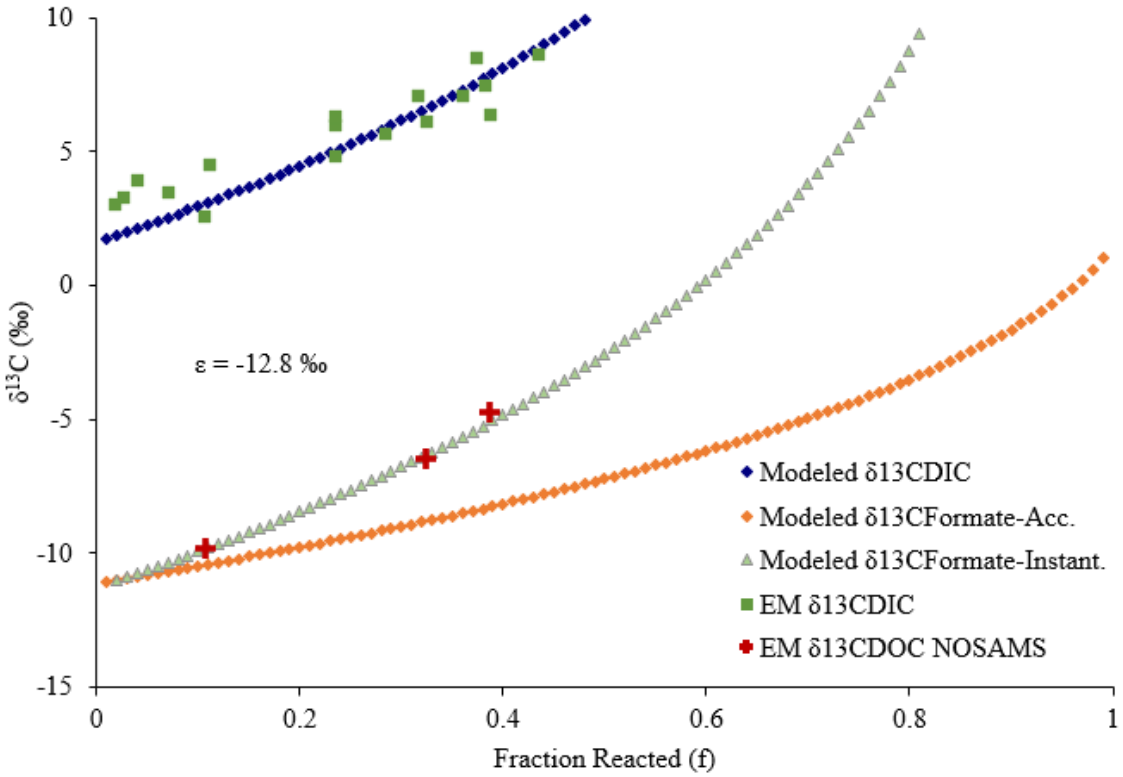


**Figure A.8: Open system Rayleigh fractionation model between DIC and formate, ε = -12.8 ‰.** Three reservoirs are represented: DIC, accumulated formate, and instantaneous formate. Endmember values for DIC and DOC are provided to guide the determination of ε by fitting modeled DIC to endmembers.